The Impact of Anthropogenic Activities on Global Terrestrial Carbon Fluxes

著者	Melnikova Irina
学位授与機関	Tohoku University
URL	http://hdl.handle.net/10097/00128457

Doctoral Thesis
博士論文

The Impact of Anthropogenic Activities on Global Terrestrial Carbon Fluxes

（人為的活動が全球の陸域炭素フラックスに与えるインパクト）

東北大学大学院理学研究科
地球物理学専攻

Irina Melnikova
メルニコワ・イリーナ

論文審査委員

山崎 剛 教授（指導教員・主査）
青木 周司 教授
森本 真司 教授
岩崎 俊樹 教授（特）
佐々井 崇博 助教

2019
令和元年

Doctoral Thesis

The Impact of Anthropogenic Activities on Global Terrestrial Carbon Fluxes

（人為的活動が全球の陸域炭素フラックスに与えるインパクト）

Irina Melnikova
(メルニコワ・イリーナ)

Department of Geophysics
Graduate School of Science
Tohoku University

Thesis Committee Members

Professor Takeshi Yamazaki (Chair, Supervisor)
Professor Shuji Aoki
Professor Shinji Morimoto
Professor Toshiki Iwasaki
Assistant Professor Takahiro Sasai

2019

Thesis Adviser | Author
Prof. Takeshi Yamazaki | **Irina Melnikova**

The Impact of Anthropogenic Activities on Global Terrestrial Carbon Fluxes

Abstract

The anthropogenic activity via land use change and fossil fuel and cement emissions substantially affect the Earth system, leading to the atmospheric CO_2 increase that is recognized to be the main cause of the increasing global surface temperatures and consequent climate change. The unprecedented human-induced alterations in the Earth system since the Industrial Revolution drove the carbon cycle out of equilibrium, so that currently, the global biosphere acts as an uptake of more than half of anthropogenic carbon emissions. The largest and the most uncertain contributor to the interannual carbon uptake is land. An accurate understanding of the impact of anthropogenic activity on the land carbon uptake is crucial for quantifying the future carbon-climate feedbacks.

The land uptake is the net balance of gross primary production (GPP) and terrestrial ecosystem respiration (TER). GPP and TER exhibit large magnitudes and interannual variabilities that makes it difficult to distinguish the impacts of anthropogenic activity on the fluxes, i.e., the GPP and TER *anthropogenic effects*, from the impacts of natural climate variability, i.e. GPP and TER *natural effects*. Factorial simulations using several biosphere models have been used to estimate the effects of long-term climate change on global GPP and TER. However, no study has integrated large-ensemble climate simulation data into a biosphere model to realistically estimate global terrestrial carbon fluxes with associated uncertainty and to project the future changes in the carbon fluxes by using statistical tools such as the probability density functions.

This thesis presents an approach to estimate the global GPP and TER with associated climate data-induced uncertainty that combines a diagnostic biosphere model with a large-ensemble climate simulation data set. I aim to distinguish the GPP and TER anthropogenic and natural effects in present 1952–2010 climate and future +2K and +4K warming climate simulations, identify the drivers and explore the probabilistic changes in GPP and TER with warming. In order to get realistic estimates of the global terrestrial GPP and TER with the associated input data-induced uncertainty, I force the biosphere model BEAMS with historical (HPB), “nonwarming” (HPB NAT), and future +2K and +4K (warmer than preindustrial) climate simulations of the Database for Policy Decision-Making for Future Climate Change

(d4PDF). In order to identify the drivers of GPP and TER anthropogenic effects, I carry out several sensitivity experiments.

First, I provide evidence for an increasing anthropogenic effect on global terrestrial GPP. The GPP anthropogenic effect is driven by CO_2 fertilization, which is projected to weaken or saturate by 2050–2150, depending on the representative concentration pathway scenario used. Model results suggest that shortwave radiation couples with ENSO conditions and volcanic eruptions to drive the natural GPP effect. While currently, the CO_2 fertilization effect primarily drives the tropical GPP increase that dominates the global GPP anthropogenic effect, in the future warmer world, the climate drivers are projected to constrain the tropical GPP increase, so that the climate-driven non-tropical GPP increase takes over the dominancy of the GPP anthropogenic effect.

Second, I show that despite the benefits of CO_2 fertilization effect on global GPP, the GPP anthropogenic effect cannot catch up with the increasing carbon emissions. Most likely, the major biosphere flux responsible for the increased atmospheric carbon growth is TER. The multi-ensemble model simulations show that both magnitude and interannual variability of TER increase in warmer climates with larger relative increase in high latitudes. The higher TER variability corresponds to higher TER in the tropics and mid-to-high northern latitudes. The main driver of future TER anthropogenic effect is temperature, while the effects of vapor pressure and precipitation are uncertain due to regional uncertainties in the climate projections. While in 1952–2010, temperature played only a minor role in the TER anthropogenic effect, its role is projected to increase in the future warmer climates because the contribution of temperature in driving TER increases with warming exponentially according to Q10 function.

Overall, the findings of the present study clarify the mechanism of the changes in land carbon fluxes due to the impacts of the anthropogenic activity on the Earth system. I show that both GPP and TER anthropogenic effects increased in the past, and are projected to increase in future warmer climates. While the GPP anthropogenic effect is the largest in the tropics, the TER anthropogenic effect exhibits bipolarity. While in the future climate simulations, the GPP anthropogenic effect is projected to weaken at higher CO_2 concentrations, no synchronic weakening is projected for the TER anthropogenic effect with higher temperatures. The disproportional increase in TER with warming towards high latitudes that are a massive reservoir of soil carbon highlight the need in the urgent action for stronger mitigation of anthropogenic emissions.

Contents

Chapter 1 Introduction 1

1.1 The impact of anthropogenic activities on the Earth system 1

1.2 Terrestrial carbon cycle 3

1.3 Estimation of global terrestrial gross primary production and ecosystem respiration 4

1.4 Purpose of this study 6

Chapter 2 Data and methods 7

2.1 The terrestrial biosphere model BEAMS 7

2.2 Database for Policy Decision-Making for Future Climate Change 10

2.3 Evaluation of input data 12

2.4 The default simulation and sensitivity experiment 16

2.5 Evaluation of the simulated carbon fluxes by BEAMS 19

2.6 Auxiliary data 22

Chapter 3 The impact of anthropogenic activities on gross primary production (Melnikova, I., & Sasai, T. (2020). Effects of anthropogenic activity on global terrestrial gross primary production. Journal of Geophysical Research: Biogeosciences, 125, e2019JG005403. https://doi.org/10.1029/2019JG005403) 23

3.1. Evaluation of input data 23

3.2. Validation and evaluation of the simulated gross primary production 26

3.3. The comparison between historical and preindustrial simulations 30

3.4. The future changes in gross primary production 37

Chapter 4 The changes in global terrestrial ecosystem respiration with climate warming 39

4.1. Evaluation of the simulated terrestrial ecosystem respiration 39

4.2. The comparison between preindustrial and future warming simulations 41

4.3. Sensitivity of terrestrial ecosystem respiration to future climate change by alternative approaches 49

Chapter 5 Discussion 51

5.1. The gross primary production anthropogenic effect 51

5.2. The contribution of gross primary production into terrestrial carbon cycle 58

5.3. The terrestrial ecosystem respiration anthropogenic effect 61

Chapter 6 Conclusion 64

List of Tables 66

List of Figures 67

List of Abbreviations 73

Acknowledgements 75

References 76

Chapter 1

Introduction

1.1 The impact of anthropogenic activities on the Earth system

The Earth system integrates four spheres, the geosphere, hydrosphere, atmosphere, and biosphere, via physical, chemical, and biological processes. The Earth's climate integrates these four spheres, and the energy, water and biogeochemical cycles (Bonan, 2015). The Earth's system was in a state of equilibrium for thousands of years before the anthropogenic activities became influential at an unprecedented scale, especially after the Industrial Revolution in 1850s. Now an additional sphere, anthroposphere, is defined to refer to a part of the Earth that is largely altered by people.

The major consequence of the anthropogenic activities is emission of greenhouse gases (GHGs) to the atmosphere. Because GHGs interact with radiative energy, e.g. solar radiation, they are a vital driver of climate via greenhouse effect (Bonan, 2015). The GHG that largely altered the Earth's climate since the Industrial Revolution is carbon.

The carbon cycle is the biogeochemical cycle by which carbon is exchanged among the spheres of the Earth. Both natural processes, e.g. volcano eruptions, photosynthesis, and anthropogenic processes, e.g. fossil fuel emissions, affect the concentration of CO_2 in the atmosphere. The anthropogenic carbon emissions, however, resulted in the unprecedently high concentrations in the atmosphere. Currently the atmospheric CO_2 concentration reached the maximum over 800 000 years (Figure 1.1). The atmosphere increase in greenhouse gases and, particularly CO_2, is the main reason of the historical global climate change (Canadell *et al.*, 2007a; IPCC, 2013b).

The anthropogenic carbon emissions include fossil fuel burning, cement production and land-use change (Baldocchi *et al.*, 2016; Le Quéré *et al.*, 2018). The atmospheric CO_2 increase above preindustrial levels was at first dominated by the deforestation and other land-use change activities, however, with the development of industry, the include fossil fuel burning, cement production emissions prevailed (Ciais *et al.*, 2013; Le Quéré *et al.*, 2018). The emissions largely affected the Earth system, and particularly atmosphere and biosphere via altered carbon cycle.

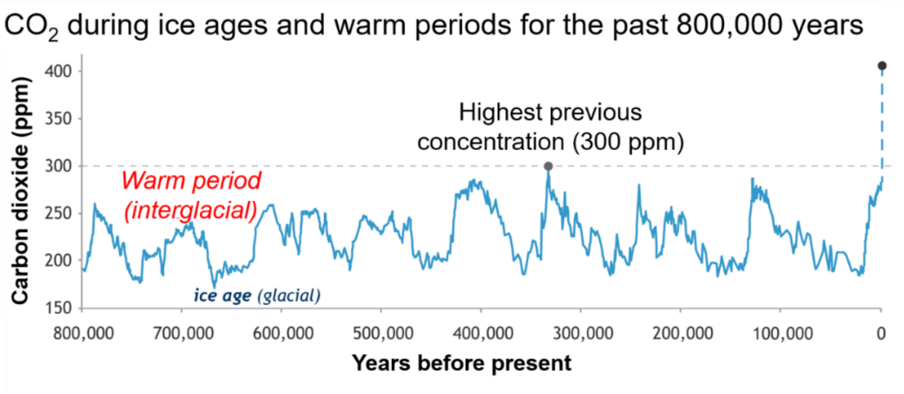

Figure 1.1. Atmospheric CO_2 concentrations in parts per million (ppm) for the past 800 000 years, based on EPICA (ice core) data. The peaks and valleys in CO_2 levels track the coming and going of ice ages (low CO_2) and warmer interglacials (higher levels). Throughout these cycles, atmospheric carbon dioxide was never higher than 300 ppm; in 2018, it reached 407.4 ppm (black dot). NOAA Climate.gov, based on EPICA Dome C data (Lüthi *et al.*, 2008) provided by NOAA NCEI Paleoclimatology Program. Modified reprints from Rebecca Lindsey, https://www.climate.gov/.

Carbon is the major chemical element constituent of most organic matter in the biosphere. It is constantly cycled through the Earth system mainly via carbon fluxes such as plant photosynthesis and respiration, litter fall and decomposition of soil organic matter by microbes and bacteria in land and via dissolution of atmospheric carbon dioxide into seawater, transportation of carbon into deep water, photosynthesis and respiration pf phytoplankton in ocean. Essentially all carbon pools exchange with the atmosphere on timescales from minutes to millions of years. In the preindustrial time when the anthropogenic activities were negligible, the atmospheric CO_2 concentration was nearly constant and equaled 277 parts per million (ppm) with variations in atmospheric CO_2 of <20 ppm, during at least the last 11,000 years prior to the Industrial Revolution. Likewise, the carbon uptakes by the biosphere, including land and ocean, were small with only insignificant interannual variation (Joos *et al.*, 2004). The anthropogenic carbon emissions resulted in the increased atmospheric carbon growth, as well as uptakes by land and ocean, i.e. land and ocean sinks. Ballantyne *et al.* (2012) reported that the global biosphere uptake doubled in 1961–2010 and absorbed more than half of the anthropogenic carbon emissions. In order to reduce the uncertainty of the future biosphere uptake, it is essential to have a robust understanding of the effect of the anthropogenic activities on the global carbon fluxes.

1.2 Terrestrial carbon cycle

The largest and the most uncertain contributor to the interannual global carbon uptake variability is land (Bousquet *et al.*, 2000; Friedlingstein *et al.*, 2014; IPCC, 2013a). The land carbon uptake is the net balance between the two large fluxes termed gross primary production (GPP) and ecosystem respiration (TER), i.e.

$$Land\ Uptake\ = GPP - TER - Residual, \tag{1}$$

where $Residual$ includes the carbon fluxes not accounted by GPP and TER, e.g. disturbances.

GPP is the rate of the total amount of carbon, i.e. carbon input into ecosystem, fixed by plants in the process of photosynthesis in a given length of time. TER is the rate of the total amount of carbon, total output of carbon, released from the ecosystem to the atmosphere. It integrates autotrophic respiration (R_A) and soil decomposition (SD). Part of carbon assimilated by the ecosystem via GPP is respired by the ecosystem for plant maintenance and growth via R_A. The remaining carbon is inputted into the soil via litter fall. The carbon stored in the soil is then exposed to decomposition by heterotrophic microorganisms via the process of SD. The GPP and TER have different sensitivities to the surrounding environmental and climate conditions. Because GPP integrates photosynthesis (equation 2) from the cell of a leaf to ecosystem level, it strongly depends on the CO_2 concentration, water availability and light.

$$nCO_2 + 2H_2O \xrightarrow{light} (CH_2O)_n + nO_2 + nH_2O \tag{2}$$

The R_A is shown to be dependent on GPP and temperature, and SD is dependent on the carbon storage in soil, soil temperature and moisture (Sasai *et al.*, 2005). The processes responsible for the enhancement of the land uptake remain uncertain. Particularly, it is well known that the increase in the CO_2 concentration causes a positive feedback on the GPP, and the increase in temperature causes a positive feedback on TER (Baldocchi *et al.*, 2016; Wang *et al.*, 2013). So far, multiple studies reported that the increase in GPP drove the increase in the land carbon uptake. But then, the land uptake as well increased during the warming hiatus in 1998–2012 when the atmospheric carbon growth stalled. Keenan *et al.* (2016) suggested that the reasons of the increased land uptake during hiatus involve both increased GPP driven by CO_2 fertilization and decreased TER driven by cooler temperatures. In support to this, Li *et al.* (2018) reported that TER growth stalled in the recent decades during cooler periods, e.g. after Pinatubo eruption and during the warming hiatus. These evidences of the increasing role of TER in the land carbon uptake raise the question whether the roles of GPP and TER are shifting.

1.3 Estimation of global terrestrial gross primary production and ecosystem respiration

The terrestrial gross primary production (GPP) and ecosystem respiration (TER) cannot be directly measured at large scales (Ma *et al.*, 2015; Welp *et al.*, 2011), thus, the estimations are typically based on upscaling *in situ* observations, satellite observations, and terrestrial biosphere models. Terrestrial biosphere models can be used to analyze the underlying processes driving GPP and TER changes because they incorporate a mechanistic understanding of biosphere carbon pools and fluxes. Two types of biosphere models exist: prognostic models that require only climate input data and diagnostic models that require climate and satellite-based vegetation input data (Sasai *et al.*, 2005). The prognostic approach benefits from the ability to forecast future carbon fluxes. The diagnostic approach gives more realistic estimates of carbon fluxes by incorporating satellite data.

Previous diagnostic studies have revealed the vegetation response to recent climatic change. Nemani *et al.* (2003) reported that climate change drove increases in global terrestrial vegetation activity during 1982–1999 primarily via decreased cloud cover and the resultant increase in shortwave radiation. Zhao and Running (2010) showed that regional droughts and a general drying trend over the Southern Hemisphere (SH) led to a decrease in vegetation activity during 2000–2009. These studies well represented interannual-to-decadal changes in carbon fluxes. However, they were limited to the satellite era and thus provide rather short term (10–30 years) analyses. Interannual climate variability strongly affects global GPP, and a few extreme events can explain most of the interannual variability (Doney *et al.*, 2006; Zscheischler *et al.*, 2014a). Consequently, current diagnostic approaches cannot distinguish the impact of anthropogenic emissions and consequent climate change on GPP (the anthropogenic GPP effect) from the impact of interannual natural climate variability on GPP (the natural GPP effect). Although a few studies have attributed natural and anthropogenic effects to changes in evaporation and leaf area index (LAI; (Mao *et al.*, 2015; Zhu *et al.*, 2016), to the best of my knowledge, this type of attribution study has not been performed for global GPP.

The study of GPP and TER anthropogenic effects involves estimating the long-term fluxes at greater than decadal timescales. The recently developed Database for Policy Decision Making for Future Climate Change (d4PDF) of Mizuta *et al.* (2017) includes 100-member ensemble outputs of an atmospheric general circulation model (AGCM) and provides the ability to compare the actual historical climate with the climate of a world where global industrial-era warming has not taken place. Integration of this newly developed long-term (1951–2010/2011) data set into a biosphere model provides the unique opportunity to attribute changes in global GPP explicitly to anthropogenic and natural effects, and permits a detailed analysis of the primary sources of these effects. Furthermore, by forcing a terrestrial biosphere model with large ensembles of climate simulations, one can account for climate data-induced uncertainty in GPP estimates that has often been overlooked. Although a few studies have estimated model structure-induced uncertainty in GPP and TER estimates (Huntzinger *et al.*, 2017; Huntzinger *et al.*, 2013; Sitch *et al.*, 2015; Sitch *et al.*, 2008), to the best of my knowledge, no study has used large-ensemble climate data to determine input data-induced uncertainty. Finally, the multi-ensemble carbon fluxes simulation of future climate projections allow analyzing the global terrestrial GPP and TER anthropogenic effects in the future warmer climates by using statistical tools such as probability density functions.

1.4 Purpose of this study

The purpose of this study is to estimate the anthropogenic effect on land carbon fluxes and their probabilistic change in future climate projections. To this end, I combine the benefits of diagnostic carbon fluxes estimations with large-ensemble climate simulations. I estimate the global GPP and TER during 1952–2010 by applying 100-member ensembles of high-resolution historical, “non-warming”, future +2K and +4K warming climate simulations from the d4PDF (Mizuta *et al.*, 2017) to the diagnostic-type biosphere model BEAMS of Sasai *et al.* (2016). For vegetation input data, I integrate satellite observations into a prognostic air temperature-based estimation, assuming an extension of the growing season and an increase in plant growth with temperature rise (Knyazikhin *et al.*, 1999; Myneni *et al.*, 1997). There are two sub-purposes in this study. First is to estimate the current (1952□2010) anthropogenic effect on global GPP with input-data uncertainty and identify drivers of GPP change. Second is to explore the changes in TER with future warming and identify the drivers of TER change.

The outline of the paper is as follows. Chapter 2 describes the methods and data, including the outline of the biosphere model BEAMS used in to estimate carbon fluxes and The Database for Policy Decision making for Future climate change (d4PDF) used to force BEAMS. In Chapter 3, I investigate the GPP anthropogenic and natural effects in 1952–2010 and their drivers. In Chapter 4, I investigate the TER anthropogenic effect in terms of magnitude and interannual variability in future +2K and +4K climates in comparison to preindustrial. In Chapter 5, I discuss the GPP and TER anthropogenic effects based on the Chapters 3 and 4, and the shifting roles of GPP and TER in the land carbon uptake with climate warming. Conclusions of this study are summarized in Chapter 6.

Chapter 2

Data and methods

2.1 The terrestrial biosphere model BEAMS

The diagnostic-type Biosphere model integrating Eco-physiological And Mechanistic approaches using Satellite data (BEAMS ver.1.3) by Sasai *et al.* (2016) has been previously validated globally and used in numerous studies (Sasai *et al.*, 2005; Setoyama & Sasai, 2013). BEAMS consists of four carbon fluxes of GPP, autotrophic respiration (R_A), litter fall, and soil decomposition (SD). It estimates GPP via the light use efficiency (LUE) concept and accounts for the environmental effects of air temperature, relative humidity, soil moisture, and atmospheric CO_2 concentrations on vegetation growth by including “stress” biophysical responses of photosynthesis to environmental factors using a photosynthesis model coupled with a stomatal conductance algorithm. TER consists of two fluxes, autotrophic respiration, R_A, and soil decomposition, SD. R_A is modeled in proportion to the potential net primary production (NPP) with temperature dependency. The SD modeling is based on the carbon cycle component of the Century model (Parton *et al.*, 1993) with water and temperature dependences. Figure 2.1 describes the BEAMS carbon processes and dependencies. The detailed explanation is given by Sasai *et al.* (2005) and Sasai *et al.* (2007).

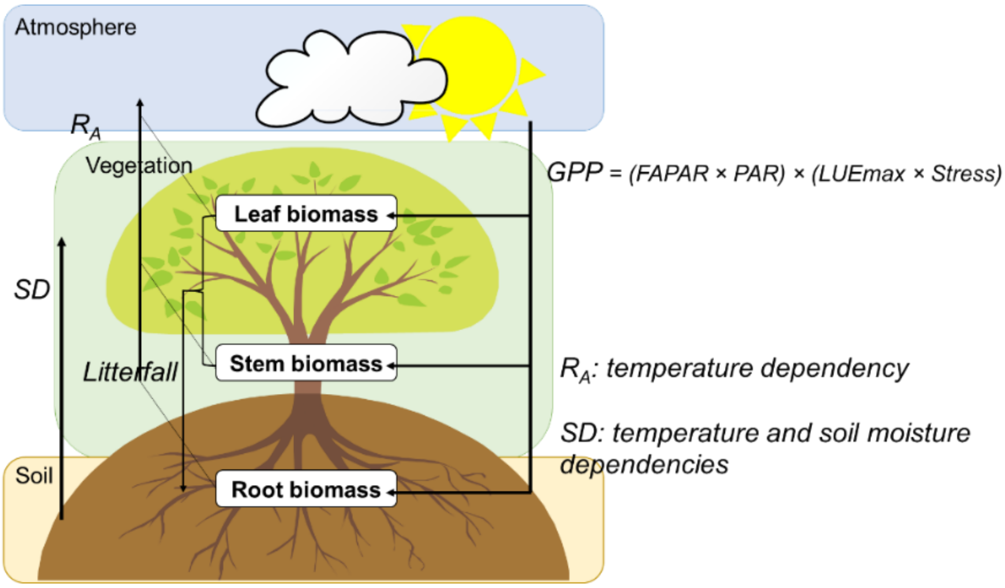

Figure 2.1. Outline of the BEAMS model structure.

BEAMS incorporates carbon, energy, and water processes in the terrestrial ecosystem and requires monthly surface climate inputs for air temperature, land surface temperature (LST), precipitation, shortwave radiation at the surface, vapor pressure, wind speed, monthly satellite observations of vegetation (fraction of absorbed photosynthetically active radiation, FAPAR and LAI), and monthly global mean atmospheric CO_2 concentrations, and temporally invariant inputs, namely land cover type, elevation, soil texture, and soil depth. The time-invariant and space-invariant (CO_2 concentration) data for BEAMS is explained in Table 2.1. The land cover change was not accounted for in the present study and the time-invariant MOD12C1 land cover of year 2004 was utilized.

Table 2.1. BEAMS input data.

Parameter	Data set	Reference
Land cover	MODIS Land Cover Type (MCD12Q1)	Friedl *et al.* (2010)
Ground elevation	Shuttle Radar Topography Mission (SRTM-30)	Farr *et al.* (2007)
Soil depth & texture	Soil Map of the World produced by the Food and Agriculture Organization of the United Nations/United Nations Educational, Scientific, and Cultural Organization (FAO/UNESCO)	Webb *et al.* (1993)
CO_2 concentration	Global historical CO_2 concentration	The Institute for Atmospheric and Climate Science, Zürich, Switzerland

BEAMS requires monthly inputs of satellite-based LAI and FAPAR. However, long-term satellite data sets began during the 1980s and, therefore, do not cover the required 60-year period. Several prognostic models can simulate LAI and FAPAR and provide long-term monthly data (Huntzinger *et al.*, 2018; Sitch *et al.*, 2015; Zhu *et al.*, 2016). They estimate vegetation variables from climate inputs, such as temperature, soil water, or photosynthetic carbon allocations. Prognostic models have been shown to overestimate mean LAI, the length of the growing season, interannual variability over the high-latitude Northern Hemisphere (NH; (Murray-Tortarolo *et al.*, 2013), and the CO_2 fertilization effect (Smith *et al.*, 2015). In fact, models often simulate a temporal mismatch in spring green-up on the order of 1–2 months and estimate a much larger positive temporal trend in global mean (Stöckli *et al.*, 2011). Smith *et al.* (2015) showed that prognostic models may be oversensitive to CO_2 fertilization.

The vegetation variables LAI and FAPAR were derived by integrating satellite observations into prognostic air temperature-based estimations. Previous studies revealed the dependence of LAI on temperature (Kunkel *et al.*, 2004; Melnikova *et al.*, 2018). In this study, I derived LAI and FAPAR using the 30-year satellite LAI and FAPAR data set GIMMS3g from Boston University and the d4PDF air temperature. I chose the GIMMS3g data set over newer but shorter-term LAI products with higher resolution (i.e. MODIS, SPOT, etc.) because the 30-year period provides the response of the LAI and FAPAR to long-term warming. I used the method proposed by Sasai *et al.* (2016) that assumes an extension of the growing season and an increase in plant growth with increasing temperature (Knyazikhin *et al.*, 1999; Myneni *et al.*, 1997). First, I calculated the relationship between satellite-based vegetation and historical air temperature data. Then, I estimated LAI and FAPAR for each member of the d4PDF HPB, HPB NAT, +2K and +4K climate simulations based on this empirical relationship and the air temperature. A detailed description of this process is provided by Sasai *et al.* (2016) and the method used is as follows.

1) Calculate the monthly GIMMS3g average LAI and FAPAR, and the 100-member ensemble mean d4PDF 2-m air temperature of the HPB climate simulation for the period 1982–2011.
2) For leaf-dropping vegetation: calculate the average leafing and leaf dropping months based on the cumulative air temperatures above 0°C before leafing and during leaf dropping for the study period. The 12 months of the year are divided into leafing, leaf dropping, growing, and dormant months.
3) For leaf-dropping vegetation: calculate the acceleration/deceleration of leafing and leaf dropping assuming that the growing season lengthens with warming for each member of the 100-member ensemble HPB and HPB NAT climate simulations of the d4PDF for the period 1951–2010.
4) For months other than leafing and leaf dropping for leaf-dropping vegetation, and for all months for evergreen vegetation, calculate the increase/decrease of LAI and FAPAR assuming increasing plant growth with rising temperature. The maximum increment is constrained for each plant functional type. Here, I use the difference in air temperature between the simulation month for each ensemble member and the average derived in (1).

2.2 Database for Policy Decision-Making for Future Climate Change

The d4PDF is a large ensemble of high-resolution (0.5625° grid) climate simulations that covers the period 1951–2010/2011 and provides the projected climates 2K and 4K warmer than preindustrial (+2K and +4K). The d4PDF was developed for use in estimations of the effects of anthropogenic climate change on extreme local weather and climate events and planning for adaptation to global warming (Mizuta *et al.*, 2017). The database uses the Meteorological Research Institute Atmospheric General Circulation Model (MRI-AGCM) version 3.2, which is a Coupled Model Intercomparison Project Phase 5 (CMIP5) member. It is coupled with an aerosol model to represent the direct and indirect effects of aerosols on radiation (Mizuta *et al.*, 2012). The cloud fraction and water content are provided from the cloud scheme. The calculation of downward surface shortwave radiation considers both the effects of aerosols and the optical properties of clouds based on the cloud water content (Mizuta *et al.*, 2012; Slingo, 1989). The d4PDF provides simulations of the historical climate (HPB), the climate of a world where global warming has not taken place in the industrial era (HPB NAT) and future +2K and +4K climates. Table 2.2 describes duration, ensemble size, and prescribed boundary conditions of the four simulations of d4PDF. The HPB simulation uses the observed sea surface temperature (SST) and sea ice from the Centennial Observation-Based Estimates of SST version 2 (COBE-SST2) data set (Hirahara *et al.*, 2014) as the lower boundary conditions, and global-mean concentrations of greenhouse gases (GHGs) and three-dimensional distributions of ozone and aerosols as external forcings. The HPB NAT simulation is of a non-warming climate and uses the same SST except that the long-term trend is removed using the average values during 1900–1919 as the baseline of the detrended SST, it uses preindustrial GHGs and aerosols (fixed at 1850 values), and ozone is fixed at 1960 values. Small perturbations were added to the SST to generate different initial conditions for the ensemble members. On a global scale, the SST pattern drives interannual climate variability and can be described in terms of El Niño Southern Oscillation (ENSO), the dominant feature of cyclic climate variability on subdecadal timescales (Yeh *et al.*, 2009). Both the HPB and HPB NAT simulations include the natural climate variability of ENSO. However, only HPB includes the anthropogenic climate effect related to the long-term SST trend and historical changes to GHG concentrations. Thus, the difference between HPB (including the anthropogenic effect and climate variability) and HPB NAT (including only climate variability) gives an explicit measure of the anthropogenic effect. Mizuta *et al.* (2017) describes the d4PDF in detail.

Table 2.2. Duration, ensemble size, and prescribed boundary conditions of the four simulations of d4PDF. Modified from Mizuta *et al.* (2017).

Parameter	**HPB**	**HPB NAT**	**+2K**	**+4K**
	Historical simulation	Non-warming simulation	Future simulation	Future simulation
Duration	60 (1951–2010)	60 (1951–2010)	60	60
Members	100	100	6 × 9	6 × 15
GHGs	Observed	Values at 1850	Values at 2040 of RCP8.5	Values at 2090 of RCP8.5
Aerosols	Monthly output from MRI-CGCM	Sulfate, black carbon, organic carbon at 1850; mineral dust, sea salt same as HPB	2040 output from MRI-CGCM	2090 output from MRI-CGCM
SST	Observed (COBE-SST2)	Detrended (COBE-SST2)	Added ΔSST 2031–2050	Added ΔSST 2080–2099

The +2K and +4K scenarios provide future climate projections in which the global-mean surface air temperature becomes 2K and 4K warmer than the preindustrial climate. The +2K simulation uses GHGs values of year 2040, and +4K simulation—of 2090 under the representative concentration pathway 8.5 (RCP8.5) of CMIP5. Mizuta *et al.* (2017) gave the detailed explanation of d4PDF. These two sets of climate simulation in addition to the internal climate variability, account for the uncertainty in future climate projections from differences in CMIP climate models. Six models that cover the most part of the uncertainty of the patterns in all the CMIP5 models are used by the data set. Specifically, the d4PDF utilizes SST changes of by CCSM4 of National Center for Atmospheric Research (United States), GFDL CM3 of National Oceanic and Atmospheric Administration GFDL (United States), HadGEM2-AO of Met Office Hadley Centre (United Kingdom), MIROC5 of AORI, NIES, JAMSTEC (Japan), MPI-ESM-MR of Max Planck Institute for Meteorology (Germany) and MRI-CGCM3 of Meteorological Research Institute (Japan).

2.3 Evaluation of input data

The d4PDF climate data were evaluated with six reanalyses (20CR V2c, ERA-Interim, JRA-55, MERRA-2, NCEP NCAR, and NCEP CFSR), four observation-based data sets (CRU TS 4.00, GPCC, GPCP, University of Delaware 4.01) and two reanalyses-observation hybrids (CRU-NCEP, Princeton University), as listed in Table 2.3.

Table 2.3. Climate and leaf area index (LAI) data sets.

Data set	**Resolution**	**Period**	**Reference**
Reanalyses			
NCEP NCAR	2.5°	1948–2016	Kalnay *et al.* (1996)
NCEP CFSR	0.5°	1979–2010	Saha *et al.* (2010)
ERA-Interim	0.75°	1979–2016	Dee *et al.* (2011)
JRA-55	1.25°	1958–2013	Kobayashi *et al.* (2015)
MERRA-2	0.675 × 0.5°	1980–2016	Bloom *et al.* (2016)
20CRV2c	2.5°	1851–2014	Compo *et al.* (2011)
Observation-based			
CRU TS 4.00	0.5°	1901–2015	Harris *et al.* (2014)
GPCC	1°	1901–2013	Schneider *et al.* (2011)
GPCP	2.5°	1979–2016	Adler *et al.* (2003)
University of Delaware 4.01	0.5°	1900–2014	Lawrimore *et al.* (2011)
Reanalyses-observation hybrids			
CRU-NCEP	0.5°	1901–2010	N. Viovy and P. Ciais, unpublished, 2010
Princeton University	1°	1948–2010	Sheffield *et al.* (2006)
Satellite-based LAI			
GIMMS3g	1/12 degree	1982–2011	Zhu *et al.* (2013)
GLASS ver.4	1-km	1982–2014	Xiao *et al.* (2014)
GLOBMAP	8-km	1982–2016	Liu *et al.* (2012)
MODIS	1-km	2000–2016	Yuan *et al.* (2011)
SPOT	1-km	2000–2016	Verger *et al.* (2016)

Table 2.4. Global 1982–2009 mean and interannual variation (by standard deviation) of climate variables from different data sets (sea surface, desert and ice areas are excluded).

Data set	**Shortwave radiation ($W\ m^{-2}$)**	**Air temperature (degC)**	**Land surface temperature (degC)**
HPB	197.42 ± 0.64	12.61 ± 0.29	12.85 ± 0.30
20CR V2c	199.40 ± 0.77	13.21 ± 0.31	
CRU TS 4.00		12.90 ± 0.31	
CRU-NCEP	191.18 ± 0.53	12.74 ± 0.31	
ERA-Interim	184.47 ± 0.69	13.01 ± 0.32	13.05 ± 0.31
GPCC			
GPCP			
JRA-55	198.72 ± 0.99	12.99 ± 0.31	13.10 ± 0.30
MERRA-2	196.50 ± 1.14	12.89 ± 0.33	13.19 ± 0.34
NCEP CFSR	189.15 ± 1.47	12.63 ± 0.37	12.80 ± 0.37
NCEP NCAR	219.53 ± 0.87	11.92 ± 0.25	12.03 ± 0.25
Princeton	181.21 ± 0.73	12.88 ± 0.30	14.19 ± 0.34
Delaware		12.71 ± 0.30	
Data set	**Precipitation (mm)**	**Vapor pressure (hPa)**	**Wind speed ($m\ sec^{-1}$)**
HPB	1051.73 ± 12.82	13.07 ± 0.18	3.42 ± 0.01
20CR V2c	1074.65 ± 28.83	12.59 ± 0.23	3.23 ± 0.03
CRU TS 4.00	898.12 ± 22.94	13.26 ± 0.21	
CRU-NCEP	859.02 ± 22.91	12.49 ± 0.19	2.48 ± 0.02
ERA-Interim	1025.27 ± 15.97	13.14 ± 0.17	3.22 ± 0.02
GPCC	901.90 ± 18.74		
GPCP	975.64 ± 19.33		
JRA-55	1047.23 ± 28.7	13.38 ± 0.16	2.53 ± 0.1
MERRA-2	900.14 ± 27.53	12.82 ± 0.16	3.32 ± 0.03
NCEP CFSR	1088.61 ± 59.46	12.05 ± 0.24	3.01 ± 0.03
NCEP NCAR	1021.96 ± 28.63	13.75 ± 0.18	2.94 ± 0.02
Princeton	873.66 ± 22.43	14.52 ± 0.17	2.84 ± 0.03
Delaware	872.61 ± 17.35		

The global long-term climate data sets that maximally cover the temporal range of the study period were selected. Decker *et al.* (2012) evaluated several climate variables, including air temperature, wind speed, precipitation, and shortwave radiation, from four reanalysis data sets using eddy-covariance site observations, and showed that all the reanalysis data sets include biases. The NCEP NCAR reanalyses overestimate shortwave radiation by >25 W m^{-2} (Decker *et al.*, 2012) and also overestimate surface temperature (Wang & Zeng, 2013). The NCEP CFSR data set has a large precipitation bias (Decker *et al.*, 2012), JRA-55 has an erroneous trend in 10-m wind speed (personal communication), and 20CR has inaccuracies in the long-term trends of wind speed according to observations (Krueger *et al.*, 2013). I excluded data with large confirmed biases from the analysis (i.e. shortwave radiation and air temperature from NCEP NCAR, LST from NCEP NCAR and Princeton University, precipitation from NCEP CFSR, and wind speed from 20CRV2c and JRA-55; Table 2.4). Table 2.5 provides a summary of terrestrial means and interannual variations (IAVs) of both included and excluded from the analysis climate data.

Table 2.5. Global 2001–2010 mean and interannual variation (by standard deviation) of leaf area index (LAI) from different data sets.

	HPB	**GIMMS3g**	**GLOBMAP**	**GLASS ver.4**
LAI	1.50 ± 0.01	1.5 ± 0.04	1.59 ± 0.02	1.72 ± 0.02
	MODIS	**SPOT**	**PhenoAnalysis**	
LAI	1.35 ± 0.02	0.77 ± 0.04	1.62 ± 0.01	
	BIOME-BGC	**CLM4**	**CLM4-VIC**	**GTEC**
LAI	4.22 ± 0.05	2.67 ± 0.04	2.09 ± 0.03	2.46 ± 0.01
	LPJ-wsl	**SiB-CASA**	**VEGAS 2.1**	
LAI	3.25 ± 0.07	3.89 ± 0.02	3.52 ± 0.02	

Because LAI and FAPAR are related by the Beer–Lambert law according to the Monsi–Saeki theory (Melnikova *et al.*, 2018), and because not all of the satellite data sets provide FAPAR, I evaluated only the derived LAI by comparing it with several satellite data sets, as described in Table 2.3. In addition, I compared the estimated LAI with the LAI of prognostic models of the global 0.5° Model outputs of Multi-scale Synthesis and Terrestrial Model Intercomparison Project, MsTMIP (Huntzinger *et al.*, 2018) downloaded from https://daac.ornl.gov/NACP/guides/NACP_MsTMIP_TBMO.html and the LAI of the Global Phenology Reanalysis (PhenoAnalysis) of Stöckli *et al.* (2011). To check whether the substitution of satellite data with the derived LAI and FAPAR distorts the GPP estimates, I performed an additional model run. The BEAMS setup was identical to that of the HPB run, (using the HPB ensemble-mean climate data), except for the use of a shorter simulation period (1982–2011) and the use of GIMMS3g LAI and FAPAR input data.

2.4 The default simulation and sensitivity experiment

I estimate the impact of anthropogenic activities on the global GPP and TER, i.e. the GPP and TER anthropogenic effects, by combining the diagnostic-type biosphere model BEAMS (Sasai *et al.*, 2016) with large ensemble climate simulations of d4PDF (Mizuta *et al.*, 2017). Here I distinguish the GPP and TER anthropogenic and natural effects by forcing BEAMS with the data of historical (HPB), 2K and 4K warmer than preindustrial climates (+2K and +4K) and nonwarming or preindustrial (HPB NAT) climate simulations. I define the GPP (TER) anthropogenic effect as the difference between GPP (TER) of HPB/+2K/+4K and GPP (TER) of HPB NAT climate simulations. Figure 2.2 illustrates the study design. First, I prepare and evaluate the surface d4PDF climatology by comparing it with existing modern climate data sets, including reanalyses, observation-based data sets and reanalyses-observation hybrids. Next, I derive BEAMS input vegetation data, i.e. leaf area index (LAI) and fraction of absorbed photosynthetically active radiation (FAPAR), using satellite (GIMMS3g) LAI and FAPAR and d4PDF air temperature, and evaluate the derived vegetation data by comparing it with existing satellite data sets.

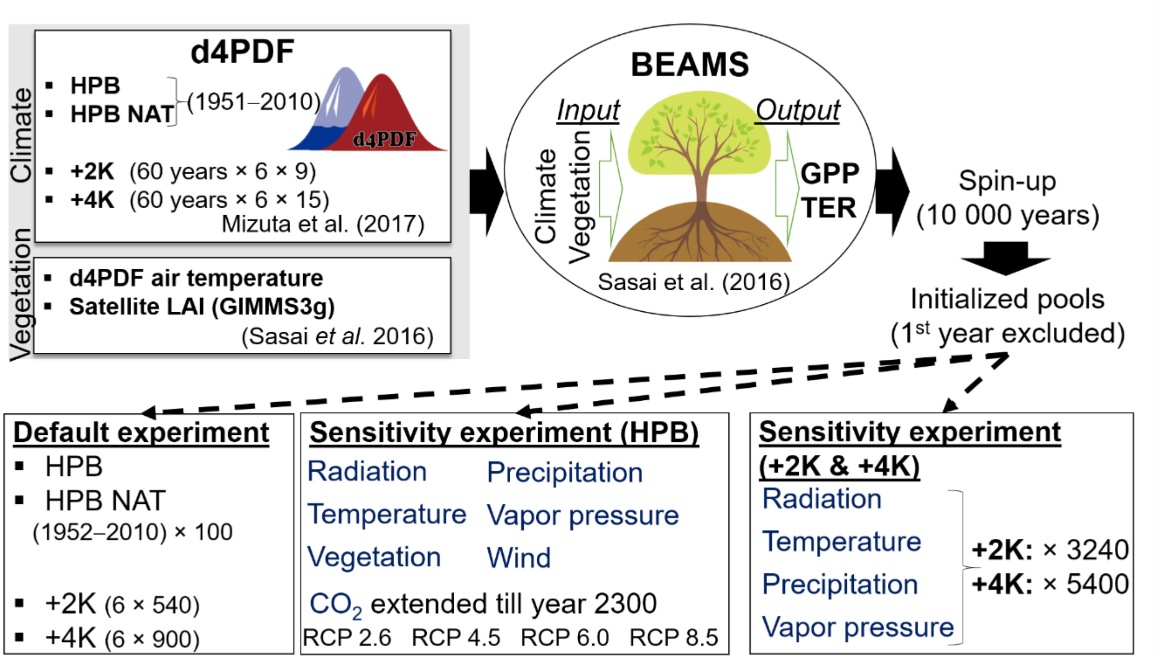

Figure 2.2. The study design used to estimate terrestrial gross primary production (GPP) and ecosystem respiration (TER) anthropogenic effect with the input data-induced uncertainty.

The BEAMS was run 2 ×100 times using the climate and vegetation inputs based HPB and HPB NAT climate simulations, 6 × 9 based on +2K and 6 × 15 based on +4K climate simulations. During the spin-up, I ran BEAMS iteratively with the first year's monthly inputs for each ensemble member for 10,000 years until the model reached equilibrium state, including that of soil carbon pool. The equilibrium criterion for the spin-up is the zero difference between GPP and TER, i.e. Net Ecosystem Production (NEP). The trajectory of both GPP and NEP of the first two decades was checked in order to confirm the fulfilment of the equilibrium criterion together with absence of large drifts of GPP in the subsequent years following spin-up for HPB (Figure 2.3). Although some transient spin-up artifact may remain in the GPP estimates, it does not largely affect the results. However, the GPP and TER estimates of the first year were excluded from the analysis because they were largely affected by spin-up.

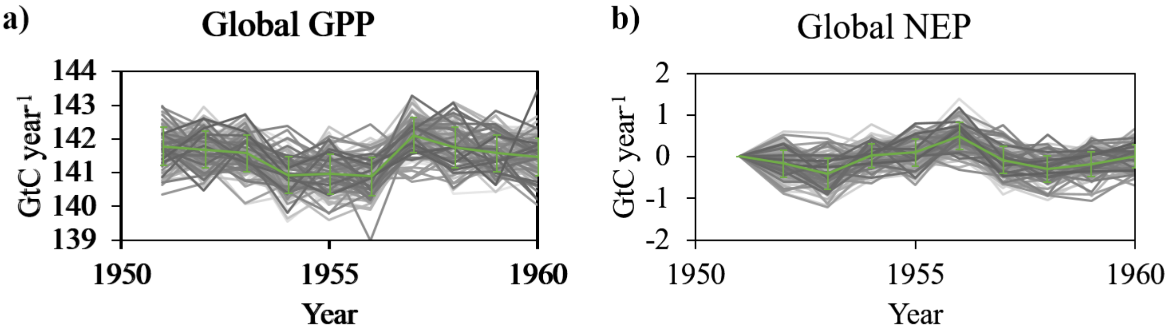

Figure 2.3. The trajectory of annual BEAMS estimates following spin-up of multi-ensemble (a) gross primary production (GPP) and (b) net ecosystem production (NEP). Gray lines indicate 100 ensemble members and green lines indicate the ensemble-mean with error bars showing standard deviation of 100 ensemble members. Year 1951 is the initial year of spin-up.

In total, 5900 years of carbon fluxes estimates in HPB and HPB NAT (100 members × 59 years of 1952–2010), 3240 years in +2K (9 × 6 members × 60 years of 2032–2091) and 5400 years of +4K (15 × 6 members × 60 years of 2052–2111) were obtained. The 0.5625-degree grid monthly d4PDF climate outputs of the six climate variables were used, including surface air temperature at 2 m (K), effective ground temperature (degC), surface air wind speed at 10 m (m sec^{-1}), surface air relative humidity at 2 m (%), total precipitation (mm), and downward shortwave radiation at the bottom (W m^{-2}). The relative humidity was converted to vapor pressure using air temperature. I used monthly global mean CO_2 concentration for HPB runs, 1850 monthly values for HPB NAT runs, 2040 and 2090 monthly values under the RCP8.5 of CMIP5 for +2K and +4K runs, respectively.

The seven ensemble HPB sensitivity runs were performed for time variable inputs in order to identify the drivers of the GPP anthropogenic effect. The following drivers were selected: CO_2 (atmospheric CO_2 concentration), radiation (shortwave radiation), temperature (air temperature and LST), precipitation, vapor pressure, vegetation (LAI and FAPAR) and wind (wind speed). In the sensitivity runs, only target variables were allowed to vary, while climate data and CO_2 inputs were kept constant at their 1951 monthly values. The same initial conditions as in the default runs were used for the sensitivity experiment. In addition, in order to examine the future evolution of the CO_2 fertilization effect, the CO_2 sensitivity experiment was extended till year 2300 using the CO_2 concentration data of four CMIP5 Representative Concentration Pathway (RCP) scenarios, namely RCP2.6, RCP4.5, RCP6.0 and RCP8.5 (Meinshausen *et al.*, 2011). The sensitivity experiment provided the ground for the discussion of the drivers of GPP anthropogenic and natural effects.

Additional four ensemble sensitivity runs were performed for time variable inputs in order to examine the impact of climate variables on TER interannual variability in future +2K and +4K climates: radiation run (shortwave radiation), temperature run (air temperature and land surface temperature), precipitation run, and vapor pressure run. Similar to HPB experiment, in the future sensitivity runs, only target variables were allowed to vary, while other inputs kept constant at the monthly values of initial year.

2.5 Evaluation of the simulated carbon fluxes by BEAMS

The GPP estimates by BEAMS was compared against GPP observations at 19 eddy-covariance sites of FLUXNET2015 database (http://daac.ornl.gov/FLUXNET/) in order to confirm the performance of BEAMS forced by d4PDF inputs. The sites that cover the major plant functional types globally were chosen. The observations covered the period of 1991–2010 depending on the site (Table 2.6).

The global mean, IAV and linear trend of GPP by BEAMS were evaluated by comparing the estimates with the existing GPP grid-data sets of two approaches: data-driven data sets and process-driven models. For the comparison with data-driven approach, I used two data sets. First data set is FLUXNET Multi-Tree-Ensemble (MTE GPP) (Jung *et al.*, 2011) that provides GPP upscaled from observations of the global network of eddy-covariance sites using the machine learning technique model tree ensembles. The data set involves two flux partitioning methods. Eddy-covariance technique uses continuous net ecosystem exchange (NEE) measurements, where NEE is the net balance between GPP and TER. The technique partitions NEE into the fluxes, GPP and TER, assuming that at night GPP is zero and TER > 0 and during daytime GPP > TER. The utilized in the present study data sets involve two flux partitioning methods according to methods by Lasslop *et al.* (2010) and Reichstein *et al.* (2005), where daytime and nighttime NEE data, respectively, are used to constrain estimation of GPP. The second data set is FLUXCOM (RS+METEO) Global Land Carbon Fluxes using CRUNCEP climate data (Jung *et al.*, 2017; Tramontana *et al.*, 2016). This data set provides estimates of GPP by three machine-learning techniques and two flux-partitioning methods. I used the means of two estimates for MTE GPP and six estimates for FLUXCOM. For the comparison with process-driven approach, I used global 0.5-degree Model outputs of MsTMIP (Huntzinger *et al.*, 2018). MsTMIP provides global estimates of GPP simulated by a standard protocol to account for the uncertainty from model structure with reference input data (Wei *et al.*, 2014). It is a factorial set of fifteen models simulations that aims to attribute the historical changes in the global terrestrial carbon fluxes to the biophysical and biogeochemical drivers (Huntzinger *et al.*, 2017; Huntzinger *et al.*, 2013). 10 out of 15 MsTMIP models that did not have any reported issues and that were used in other studies were used (Table 2.7) (Fang *et al.*, 2017; Schwalm *et al.*, 2015). For GPP evaluation, the 100-member ensemble means with distribution expressed through standard deviation of the ensemble members were used. In order to evaluate the climate, vegetation and carbon flux data, I converted them to 1-degree monthly by either averaging (higher spatial resolution to lower) or linear interpolation lower spatial resolution to higher) depending on the data set's original resolution. The data of lesser than monthly temporal resolution (LAI, U and V wind components) were converted to monthly. Only land values excluding sea surface, desert and ice areas were utilized.

Table 2.6. FLUXNET2015 sites utilized for validation of gross primary production by BEAMS.

	ID	PFT	Latitude	Longitude	Period
1	IT-BCi	Crops	40.5238	14.9574	2004–2010
2	FR-Gri	Crops	48.8442	1.9519	2004–2010
3	DE-Geb	Crops	51.1001	10.9143	2001–2010
4	US-ARM	Crops	36.6058	-97.4888	2003–2010
5	US-Ne1	Crops	41.1651	-96.4766	2001–2010
6	US-Ne2	Crops	41.1649	-96.4701	2001–2010
7	US-Ne3	Crops	41.1797	-96.4397	2001–2010
8	CH-Oe2	Crops	47.2863	7.7343	2004–2010
9	DE-Kli	Crops	50.8931	13.5224	2004–2010
10	BR-Sa3	Tropical ENF	-3.018	-54.9714	2000–2004
11	MY-PSO	Tropical ENF	2.973	102.3062	2003–2009
12	US-Ha1	DBF	42.5378	-72.1715	1991–2010
13	DE-Hai	DBF	51.0792	10.453	2000–2010
14	US-WCr	DBF	45.8059	-90.0799	1996–2006
15	AU-DaS	Savannas	-14.1593	131.3881	2008–2010
16	RU-Che	Wetland	68.613	161.3414	2002–2005
17	RU-Cok	Shrubland	70.8291	147.4943	2003–2010
18	RU-Fyo	ENF	56.4615	32.9221	1998–2010
19	RU-Ha1	Grassland	54.7252	90.0022	2002–2010

Note: PFT is plant functional type, ENF is evergreen needle forest, and DBF is deciduous broadleaf forest

The TER anthropogenic effect was evaluated in comparison to the existing TER grid-data sets of two approaches: data-driven data sets and process-driven models. The first data set, the inter-model comparison "Trends in net land-atmosphere carbon exchange over the period 1980–2010" (TRENDY) for the Regional Carbon Cycle Assessment and Processes (RECCAP) by Sitch *et al.* (2008) consists of a number of biosphere models forced with the same input data. I use ensemble mean of the five models—NCAR-CLM-4C and NCAR-CLM4-CN (Oleson *et al.*, 2010), LPJ (Sitch *et al.*, 2003), LPJ GUESS (Smith *et al.*, 2001), and VEGAS (Zeng *et al.*, 2005). The second and third data sets are data-driven, however, the utilized observational data are different. I use the global annual soil respiration (R_S) estimates over the period of 1901–2012 by Hashimoto *et al.* (2015) who developed a climate-driven model of soil respiration based on a global database of soil respiration data (SRDB) by Bond-Lamberty and Thomson (2018). Finally, TER of FLUXCOM (RS+METEO) Global Land Carbon Fluxes using CRUNCEP climate data (Jung *et al.*, 2017; Tramontana *et al.*, 2016) were utilized. This data set provides estimates of TER by three machine-learning techniques and two flux-partitioning methods (I used the ensemble-mean of six estimates). Note that R_S differs from TER by the exclusion of aboveground R_A. Usually R_S comprises between 50 and 80% of TER. Therefore, its absolute value is expected to be lower than TER.

Table 2.7. Model outputs of Multi-scale Synthesis and Terrestrial Model Intercomparison Project (MsTMIP) models utilized for evaluation of BEAMS performance.

Model	**Affiliation**
Biome-BGC	NASA Ames (Weile Wang)
ISAM	University of Illinois Urbana Champaign (Atul Jain)
CLM4	Oak Ridge National Lab (Dan Hayes)
CLM4-VIC	Pacific Northwest National Lab (Maoyi Huang)
DLEM	Auburn University (Hanqin Tian)
GTEC	Oak Ridge National Lab (Dan Riccuito)
LPJ-wsl	Laboratoire des Sciences du Climat et l'Environnement (LSCE), France (Ben Poulter)
ORCHIDEE-LSCE	Laboratoire des Sciences du Climat et de l'Environnement (LSCE), France (Gwenaëlle Berthier)
VEGAS	University of Maryland (Ning Zeng)
VISIT	National Institute for Environ. Studies, Japan (Akihiko Ito)

2.6 Auxiliary data

The data other than terrestrial biosphere fluxes were used from the Global Carbon Project (GCB) by Le Quéré *et al.* (2018). The fossil fuel and cement emissions are from Boden *et al.* (2017), land-use change emissions are from Houghton *et al.* (2012), atmospheric carbon growth rate is from Edward Dlugokencky and Pieter Tans, NOAA/ESRL and ocean sink is from Le Quéré *et al.* (2016). The residual biosphere source is defined as the difference between anthropogenic carbon emissions, atmospheric carbon growth and the biosphere uptake based on the mass balance. It involves all unaccounted fluxes.

In order to derive R_S by statistical methods, I used the soil moisture and soil temperature for level 1 (surface, <20 cm) depths, precipitation and surface air temperature of d4PDF and applied the statistical relationships derived by Hursh *et al.* (2017) decribed in Table 2.8.

Table 2.8. The statistical relationships between soil respiration and climate variables derived by Hursh *et al.* (2017).

Climate driver	Relationship	R^2
Air temperature (degC)	$y = 34.99x + 439.1$	0.89
Precipitation (mm)	$y = 270.33 + 0.43x$	0.88
Soil temperature (degC)	$y = 39.5x + 327.2$	0.91
Soil moisture ($m^3\ m^{-3}$)	$y = 150803.45x - 277187.14x^2 - 19562.43$	0.45

The temperature sensitivity of R_S is often estimated via a simple exponential temperature function based on Q10 function that refers to the increase in the respiration rate for a temperature interval of 10 degrees (Hashimoto *et al.*, 2015). Here I derived the Q10 effect on TER of HPB, +2K and +4K multi-ensemble climate simulations of d4PDF by using the equation 3:

$$TER_{new} = TER_{HPB\,NAT} \times Q10^{T_{soil\,new} - T_{soil\,HPB\,NAT}/10}, \tag{3}$$

where TER_{new} and $T_{soil\,new}$ are TER and soil temperature, respectevely, of intended multi-member ensemble climate simulation (HPB, +2K or +4K), $TER_{HPB\,NAT}$ and $T_{soil\,HPB\,NAT}$ are long-term ensemble mean of monthly TER and soil temperature, respectively, of HPB NAT simulation, i.e. mean monthly TER and soil temperature of pre-industrial climate. Q10 is values estimated using the temperature function from Hashimoto et al. (2015).

Chapter 3

The impact of anthropogenic activities on gross primary production

(Melnikova, I., & Sasai, T. (2020). Effects of anthropogenic activity on global terrestrial gross primary production. Journal of Geophysical Research: Biogeosciences, 125, e2019JG005403. https://doi.org/10.1029/2019JG005403)

3.1. Evaluation of input data

The accuracy of surface climatology of the Database for Policy Decision-Making for Future Climate Change (d4PDF) was confirmed in comparison to the d4PDF interannual and latitudinal variations with the existing climate data sets, frequently used in the studies of carbon fluxes (Figure 3.1). Previously, Yukimoto *et al.* (2012) evaluated the performance of the MRI-AGCM ver.3 and concluded that the model reproduces the overall mean climate, seasonal variation, and IAV, including El Niño Southern Oscillation (ENSO). The authors acknowledged the existing cold bias in the Northern Hemisphere (NH) and warm bias in the Southern Hemisphere (SH). Here, the d4PDF suitability for uses in the studies of the carbon-climate feedbacks is addressed. The surface climatology of d4PDF is within the range of other data sets, except for wind speed that is higher in HPB, especially in the NH (Table 2.3). The difference in wind speed between the satellite observations based high-resolution MERRA-2 reanalyses and d4PDF is only about 0.1 m sec^{-1}. Besides, wind speed is only a minor input variable in BEAMS. The range of climate data set estimates is as follows: 18.2 W m^{-2} for shortwave radiation, 0.4 degC for LST, 0.6 for air temperature, 215.6 mm year^{-1} for precipitation, 2.5 hPa for vapor pressure, and 0.83 m sec^{-1} for wind speed (1982–2009 mean).

The latitudinal similarity with existing data sets is overall high (Figure 3.1b). The d4PDF agrees well with other data sets in terms of positive temporal trends in air temperature, LST and vapor pressure. The anomalies of d4PDF data are consistent with the modern data sets (Figure 3.1a). Overall, d4PDF reproduces the interannual variability of surface climate variables in consistency with existing climate data sets.

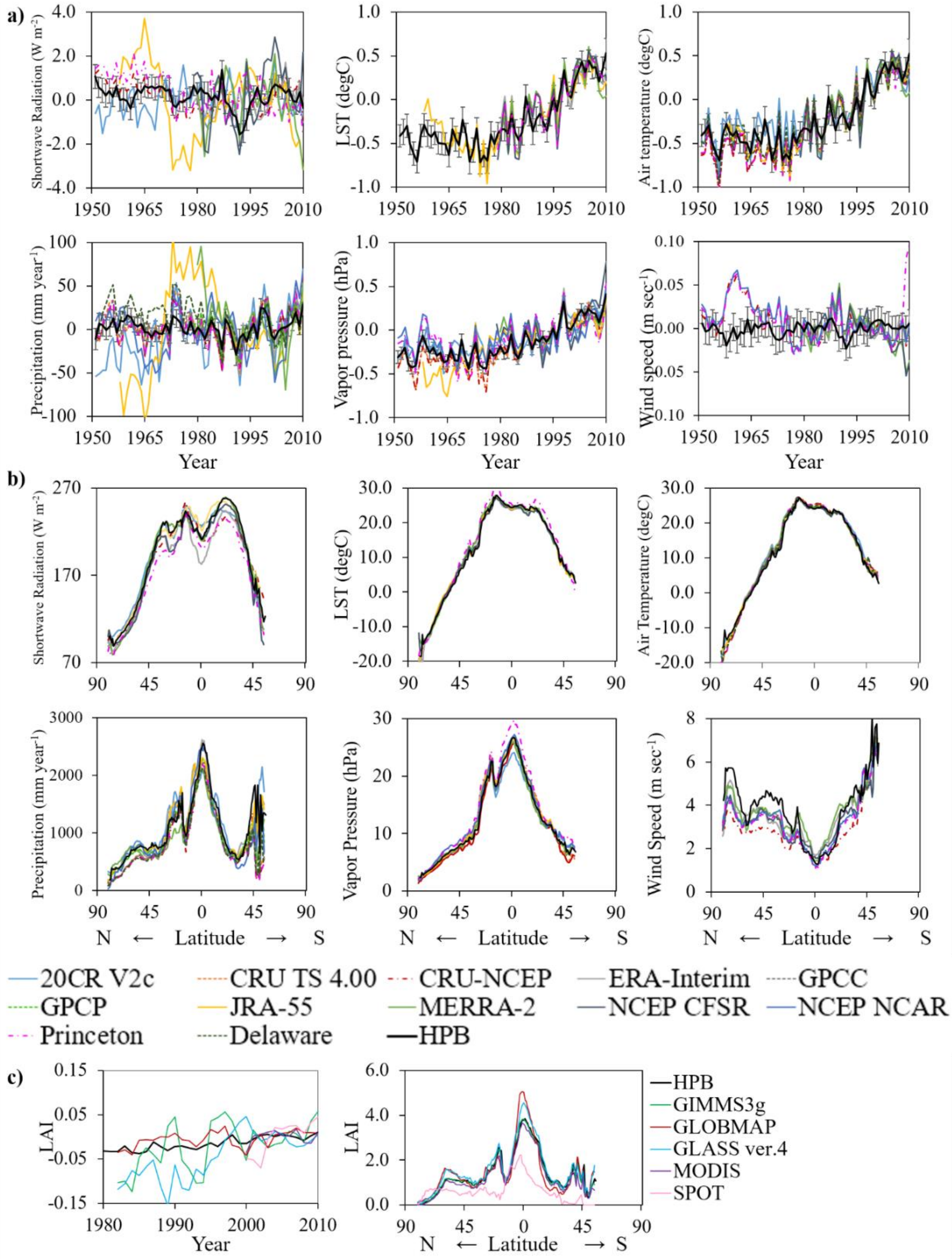

Figure 3.1. (a) Interannual anomalies and (b) latitudinal variations in climate variables from different data sets (sea surfaces, deserts, and ice areas are excluded) for the 1982–2009 mean. HPB indicates the ensemble mean of the historical d4PDF simulation. Error bars indicate one standard deviation of the 100 ensemble members. Solid lines indicate reanalyses, square dotted lines indicate observational data sets, and dash-dot lines correspond to reanalysis–observation hybrids. (c) Global leaf area index (LAI) interannual variations (left) and latitudinal variations (right) based on the 2000–2010 average LAI from several satellite data sets. HPB indicates the ensemble-mean LAI derived from the GIMMS3g LAI and the d4PDF (HPB) air temperature.

The climatology of derived LAI has overall reasonable temporal and latitudinal agreement with the satellite data sets (Figure 3.1c). The absolute values and temporal trends of d4PDF are within the range of existing data sets, but the derived LAI (HPB) has smaller IAV compared to that of the satellite data sets, especially the long-term (i.e., GIMMS3g and GLASS). The long-term change in the derived LAI is somewhat over-smoothed. For example, the LAI decrease after a large volcano eruption in 1991 (Pinatubo) is absent. In the previous study, Jiang *et al.* (2017) compared the modern long-term satellite data sets and reported that the available long-term LAI satellite products are neither intraconsistent over time nor latitude. The major reasons for the LAI discrepancy in the products are the differences in input surface reflectance and reflectance preprocessing algorithms, the retrieval algorithm, and the treatment of vegetation types (Jiang *et al.*, 2017; Liu *et al.*, 2018a). The comparison of interannual LAI variation with the prognostic LAI estimates (Table 2.4) showed larger linear LAI trends that were reported before (Smith *et al.*, 2015). The effect of Pinatubo eruption on the global vegetation is not completely understood yet. Some studies reported a decrease in vegetation growth in 1992–1993 due to temporary cooling caused by the eruption (Lucht *et al.*, 2002), especially in the high latitudes of the NH (Nemani *et al.*, 2003). Other studies reported the GPP increase in northern deciduous forest due to the aerosol-induced increase in diffuse radiation (Gu *et al.*, 2003). In fact, the presence of clouds and aerosols reduces the quality of satellite observations dramatically.

Overall, due to large divergence in LAI products, the estimated by empirical method LAI cannot be either confirmed or discredited. The data set is appropriate for the use in GPP simulations. However, the related level of uncertainty in the results of this study due to uncertainties in LAI estimates exists.

3.2. Validation and evaluation of the simulated gross primary production

The BEAMS estimates of GPP forced with d4PDF data against observations at 19 eddy-covariance sites with a Pearson correlation coefficient $R = 0.923$ (Figure 3.2). BEAMS underestimated the interannual GPP variation compared to the in situ observations. There are several possible reasons for this underestimation. One is that the underestimation of LAI IAV (described in Section 3.1) may have translated to the underestimation of GPP IAV. However, the underestimation of GPP IAV, although to a lower degree, remains even when BEAMS is forced with satellite-based vegetation data (Figure 3.3). Therefore, underestimation of IAV of input climate variables in d4PDF should have contributed to the underestimation of GPP IAV by BEAMS. Indeed, the IAVs of d4PDF climate variables are lower than the average of existing grid climate data sets (Table 2.4), although they are usually not the lowest ones among the existing data sets. Finally, the larger pixel size of the BEAMS estimates compared to the size of in situ site should have contributed to the smaller GPP IAV because it flattens over large area (Melnikova *et al.*, 2018). All three factors are considered to contribute to the underestimation of GPP IAV by BEAMS compared to the in situ observations.

Because BEAMS estimated higher very high GPPs compared to observations, I tested whether the substitution of satellite data with the derived LAI and FAPAR distorted the GPP estimates. The comparison of BEAMS GPP forced by both derived in this study and satellite LAI and FAPAR data (Figure 3.3) showed analogous performance with the correlation coefficient $R = 0.995$ between BEAMS GPP estimates at 19 sites. Therefore, the use of derived vegetation data could not be the reason of higher very high BEAMS GPPs compared to observations. A thorough study on the matter is required because the earlier study of BEAMS validation by Sasai *et al.* (2005) did not involve GPPs higher than 2000 gC m^{-2} $year^{-1}$. Because the correlation coefficient is overall high, the reasonable performance of BEAMS forced by d4PDF climate and vegetation data is confirmed.

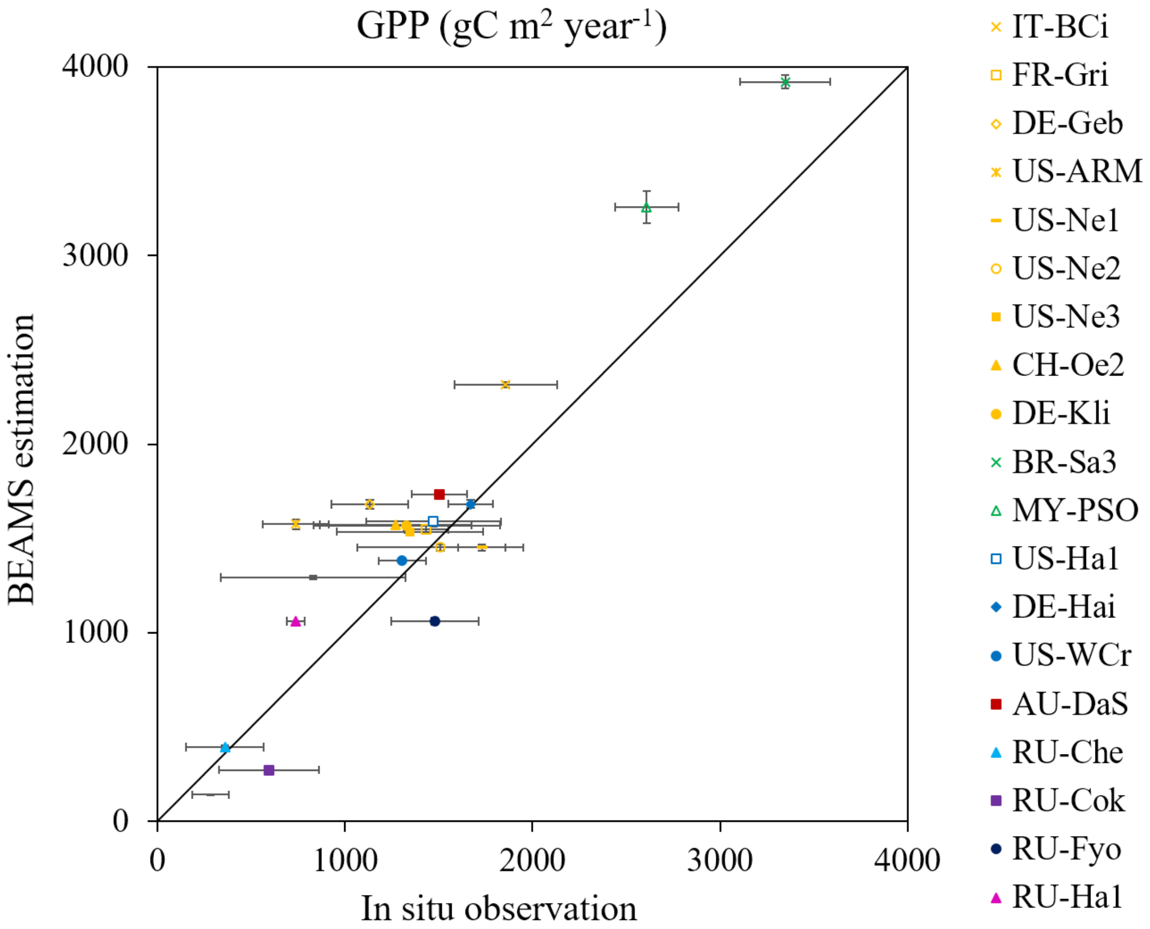

Figure 3.2. Comparison between interannual mean gross primary productions (GPP) by BEAMS forced with d4PDF data and in situ GPP observations at 19 eddy-covariance sites globally. The sites are divided into plant functional types by colors: tropical evergreen broadleaf forest (green), crops (orange), deciduous broadleaf forest (blue) and evergreen needle forest (dark blue), wetlands (light blue), grasslands (magenta), savannas (dark red) and shrub-lands (purple). The error bars indicate interannual variation.

The estimated global GPP equaled 145.7 ± 1.6 GtC year^{-1} (the spread indicates IAV by SD) in 1982–2010 and fell within the range of existing global terrestrial GPP estimates of 112.0–169.0 GtC year^{-1} reviewed by Anav *et al.* (2015) and 133.0 ± 15.0 GtC year^{-1} by Piao *et al.* (2013). However, the estimate is higher than the global GPP mean of 123.0 ± 8.0 GtC year^{-1} by Beer *et al.* (2010). Note, that SD of the estimates by Anav *et al.* (2015), by Piao *et al.* (2013) and Beer *et al.* (2010) indicate the spread of estimates by different models and approaches. One possible reason of high global GPP by BEAMS is the high input shortwave radiation of d4PDF compared to existing climate data sets (Figure 3.1). The second possible reason is that BEAMS estimated higher high GPPs (>2000 gC m^{-2} year^{-1}) compared to observations (Figure 3.3). The moderate spatial resolution of simulated GPP, 0.5625 degree-grid, aggregates area of about 60 km. Sasai *et al.* (2016) compared BEAMS simulation of net ecosystem production (NEP) with 1-degree and 10-km grid-scale resolutions and suggested a tendency of coarser resolution to have lower low and higher high NEP values. Similarly, Joiner *et al.* (2018) pointed out that better statistical comparisons with the eddy-covariance data are achieved when satellite data are used at high spatial resolution similar to the typical footprint of eddy-covariance site of one km^2. Meanwhile, the annual GPP by BEAMS agreed well with the study that used chlorophyll fluorescence and estimated GPP of 137 ± 6 GtC year^{-1} in 2015 (Norton *et al.*, 2018).

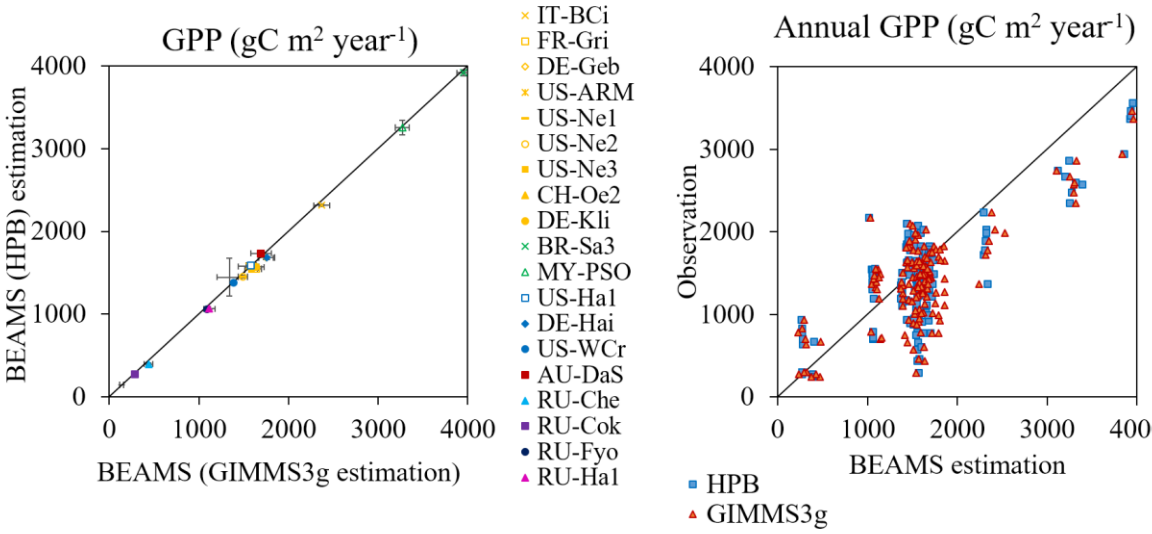

Figure 3.3. (a) Comparison between interannual mean gross primary production (GPP) by BEAMS forced with GIMMS3g- and d4PDF-based leaf area index (LAI) and fraction of absorbed photosynthetically active radiation (FAPAR) data. The sites are divided into plant functional types by colors: tropical evergreen broadleaf forest (green), crops (orange), deciduous broadleaf forest (blue) and evergreen needle forest (dark blue), wetlands (light blue), grasslands (magenta), savannas (dark red) and shrub-lands (purple). The error bars indicate interannual variation by standard deviation. (b) Comparison of GPP by BEAMS forced with GIMMS3g and d4PDF against GPP flux tower observations at 21 sites globally.

The global mean, IAV and linear trend of GPP by BEAMS were compared with the grid-data sets of two types, data-driven (MTE GPP and FLUXCOM) and process-driven (MsTMIP) approaches for the shared period for all data sets of 1982–2010. The three statistical parameters—the mean, IAV and linear trend—of the ensemble-mean GPP by BEAMS (HPB) were within the range of existing data sets by data- and process-driven approaches (Table 3.1). In comparison with the existing GPP grid-data sets, BEAMS estimated higher IAV and linear trend of GPP than the data-driven approach, and lower IAV and linear trend of GPP than the process-driven approach. The data-driven approach estimates GPP by upscaling the eddy-covariance observations. The eddy-covariance sites are usually located in the areas of little anthropogenic disturbance, and therefore, the resulting data sets do not explicitly account for the anthropogenic disturbance, i.e. land-use change. In addition, the observations are affected by the specific conditions of the given ecosystem (age, successional stage etc.) and are frequently limited to the short periods. The process-driven approach, on the other hand, overestimated GPP trend due to overestimation of CO_2 fertilization effect. Only BEAMS simulated the large GPP increase during intensive warming in 1980–2000 and zero trend during warming hiatus in 2000–2010. This finding agrees with the satellite-based studies of NPP (Zhao & Running, 2010), LAI (Alton, 2018) and GPP (Ballantyne *et al.*, 2017).

Table 3.1. Global mean, interannual variation (IAV) and 1982–2010 linear trend of terrestrial gross primary production (GPP).

	BEAMS (HPB)	**MTE GPP**	**FLUXCOM**
Mean GPP	145.7 ± 0.1	116.0	114.1
IAV	1.6 ± 0.1	1.4	0.4
Linear trend	0.16^{***}	0.08^{**}	0.01^{ns}

	BIOME-BGC	**ISAM**	**CLM4**	**CLM4-VIC**	**DLEM**
Mean GPP	128.0	94.1	133.2	105.5	101.9
IAV	3.0	1.9	4.3	3.8	3.4
Linear trend	0.25^{***}	0.21^{***}	0.48^{***}	0.42^{***}	0.37^{***}

	GTEC	**LPJ-wsl**	**VEGAS 2.1**	**VISIT**	**TRIPLEX-GHG**
Mean GPP	175.6	129.2	107.0	111.6	118.9
IAV	4.3	4.1	2.4	4.1	3.9
Linear trend	0.49^{***}	0.45^{***}	0.24^{***}	0.44^{***}	0.42^{***}

Note: The unit of mean and interannual variation, IAV (through standard deviation) of GPP is GtC year^{-1}, the unit of GPP linear trend is GtC year^{-2}; ns corresponds to non-significant trends, * corresponds to p-value < 0.05, ** corresponds to p-value < 0.01, *** corresponds to p-value < 0.001.

3.3. The comparison between historical and preindustrial simulations

To determine the GPP anthropogenic effect, first, the effect of anthropogenic activities on global climate was investigated. Figure 3.4a shows the IAV of global land climate variables for six decades. Air temperature, LST, precipitation and vapor pressure displayed a clear positive trend. The difference in the shortwave radiation of the HPB and HPB NAT climate simulations was 3.17 ± 0.65 W m^{-2} in the beginning of the study period, and increased over time due to the negative trend in HPB; the difference in 10-m wind speed of two simulations was nearly constant over time. The differences in climate variables, emerging with warming, were consistent with existing studies that reported increased surface temperatures, intensified water cycle with warming (Boucher *et al.*, 2013; Richardson *et al.*, 2018). The anthropogenic effect on the surface radiation is less certain, although model-based studies report decrease in shortwave radiation at surface with warming (Richardson *et al.*, 2018). To the best of my knowledge, there is no observational evidence of the long-term decrease in surface shortwave radiation with instead the large decadal variability (Wild, 2016). The existing observation-based studies report that the surface shortwave radiation decreased until 1980s and increased in many regions since then (Hayasaka, 2016). The MRI-AGCM simulated a 3.3 W m^{-2} difference in shortwave radiation between HPB and HPB NAT climates already in the beginning of the study period (Figure 4a). The difference in shortwave radiation between HPB and HPB NAT simulations by the AGCM most probably occurred due to the differences in the input anthropogenic aerosols and water vapor that is in line with conclusions of Hayasaka (2016).

Overall, the global anthropogenic effect on climate based on the difference between 2001–2010 and 1951–1960 means was as follows: 4.07 ± 0.66 W m^{-2} decrease in mean shortwave radiation, 1.20 ± 0.18 degC increase in temperature, 28.66 ± 13.52 mm $year^{-1}$ increase in precipitation, 0.89 ± 0.09 hPa increase in vapor pressure, and 0.01 ± 0.02 m sec^{-1} decrease in wind speed. The global terrestrial shortwave radiation, air temperature, LST, and vapor pressure of HPB and HPB NAT share neither ensemble means nor spread of global annual values. Figure 3.4b provides an outlook on the spatial patterns of the HPB and HPB NAT climate simulations. The largest decrease in shortwave radiation takes place in Africa and Southeast Asia, the largest increase in temperature takes place in the northern high latitudes. Precipitation increases in the high-precipitation and decreases in the low-precipitation regions.

Vapor pressure increases globally with the largest increase in SH, especially tropics. The changes in wind speed are globally small and regionally heterogeneous: there are slight increases over North America, central Australia and northern Eurasia, and decreases elsewhere.

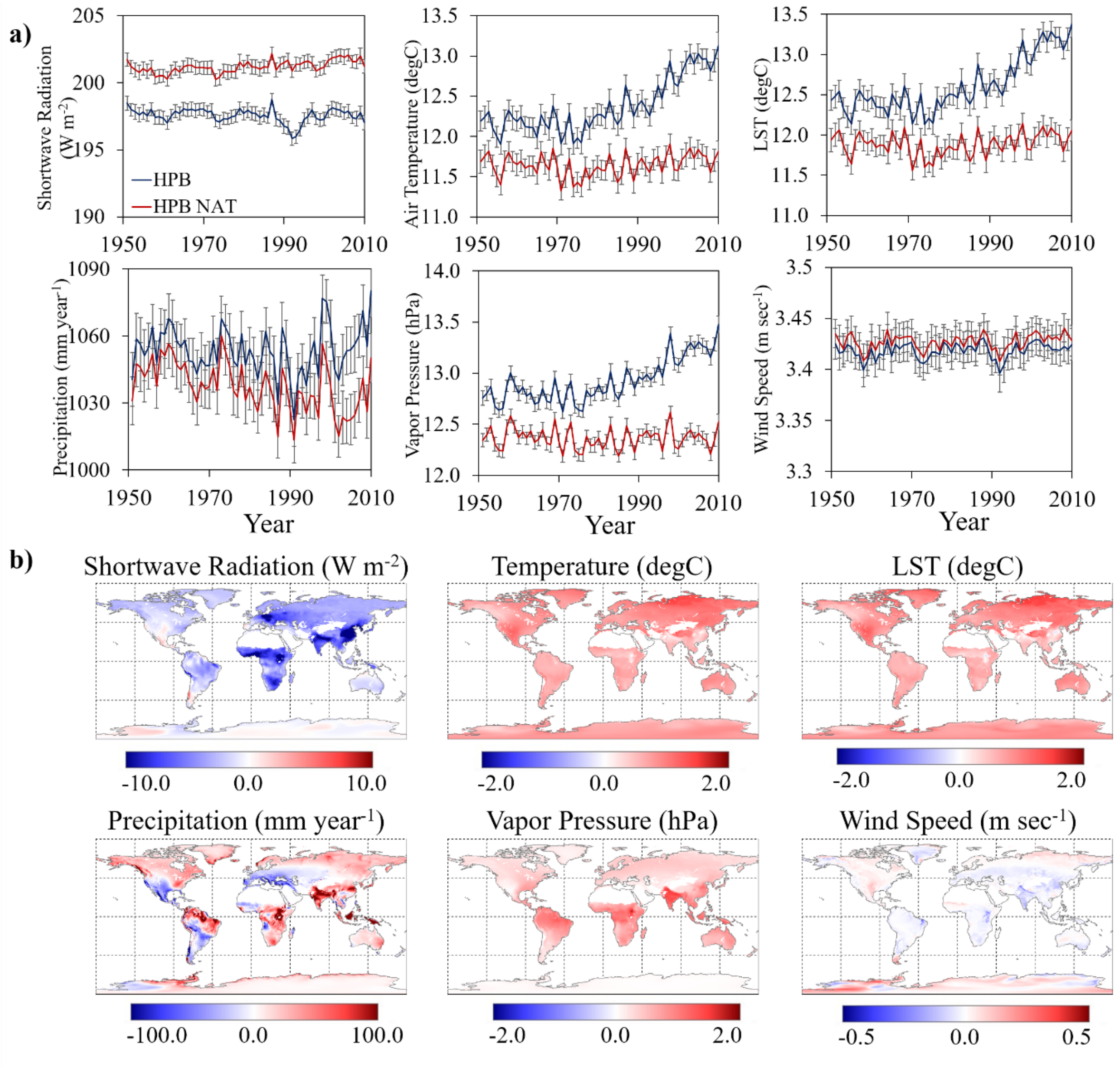

Figure 3.4. (a) Interannual variation of 100-member ensemble means of climate variables from historical (HPB) and nonwarming (HPB NAT) climate simulations. The error bars indicate standard deviation between ensemble members. (b) Spatial distribution of the ensemble means of the anthropogenic effect (HPB – HPB NAT) on the climate variables (excluding sea surface, desert and ice areas).

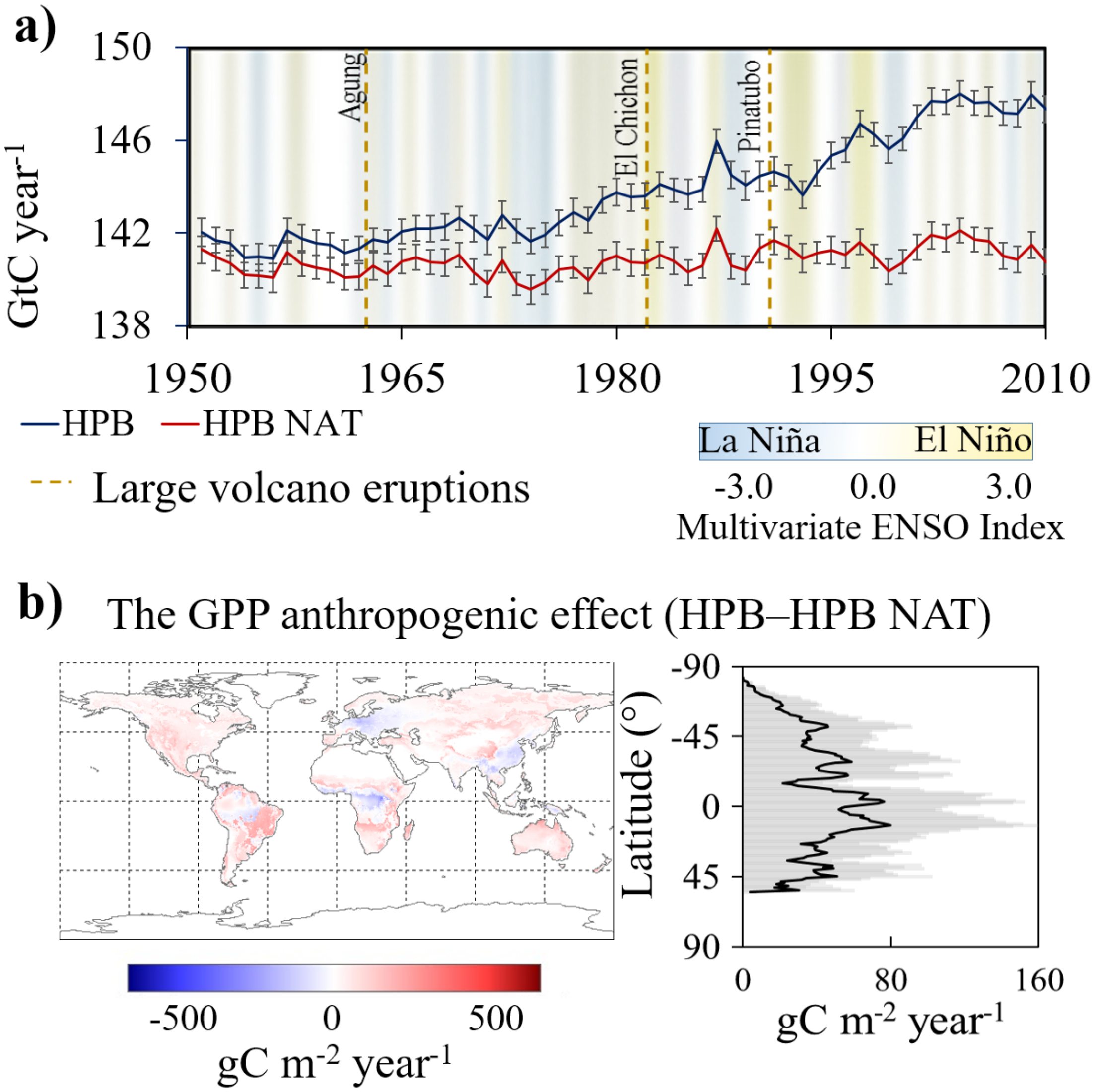

Figure 3.5. The gross primary production (GPP) anthropogenic effect. (a) Long-term interannual variation of 100-member ensemble means of the historical and nonwarming climates. The error bars indicate standard deviation between ensemble members. The names of the erupted volcanoes with climatologically corrected Volcanic Explosivity Index (VEI) > 5 are provided. The Multivariate ENSO Index (MEI) data were downloaded from https://www.esrl.noaa.gov/psd/enso/mei.ext/table.ext.html and volcano aerosols data were from http://www.juergen-grieser.de/downloads/VolcanicAerosolForcing/vaod.dat. (b) The difference between 1952–2010 GPP of the historical (HPB) and nonwarming (HPB NAT) climate simulations. Latitudinal pattern (1° bands) of mean GPP anthropogenic effect. The shading indicates the longitudinal variation by standard deviation. The sea surface, desert and ice areas are excluded.

The long-term (1952–2010) global mean GPP equaled 143.8 ± 0.1 GtC year^{-1} in HPB and 140.8 ± 0.1 GtC year^{-1} in HPB NAT climate simulations. The mean GPP anthropogenic effect equaled 2.2% of GPP in HPB NAT. It increased over time from the mean 0.9 ± 0.1 Gt year^{-1} in the first decade to 6.1 ± 0.3 Gt year^{-1} in the last decade of the study period, while the spread (by standard deviation) of the ensemble runs constantly remained 0.6 Gt year^{-1}. The 1952–2010 linear GPP trend in HPB was 0.12 GtC year^{-2} ($p < 0.001$), and the trend also increased over time. The interannual GPP variation appeared rather similar in HPB and HPB NAT with only some minor differences (Figure 3.5). The GPP peaks coincide with ENSO events: positive peaks covariate with El Niño and negative peaks–with La Niña. The typical increase during El Niño did not occur after Pinatubo eruption that resulted in cooler temperatures and decreased length of growing-season in NH (Nemani *et al.*, 2003). The input-data induced uncertainty in GPP estimated by multi-member ensemble BEAMS runs indicates that GPP of the HPB was significantly different from the GPP of HPB NAT climate simulation, the difference increased over time. Neither the GPP natural effect, nor the climate input-data induced uncertainty can explain the global GPP change in 1952–2010. The GPP anthropogenic effect was accountable for the large changes in the global GPP over the six decades.

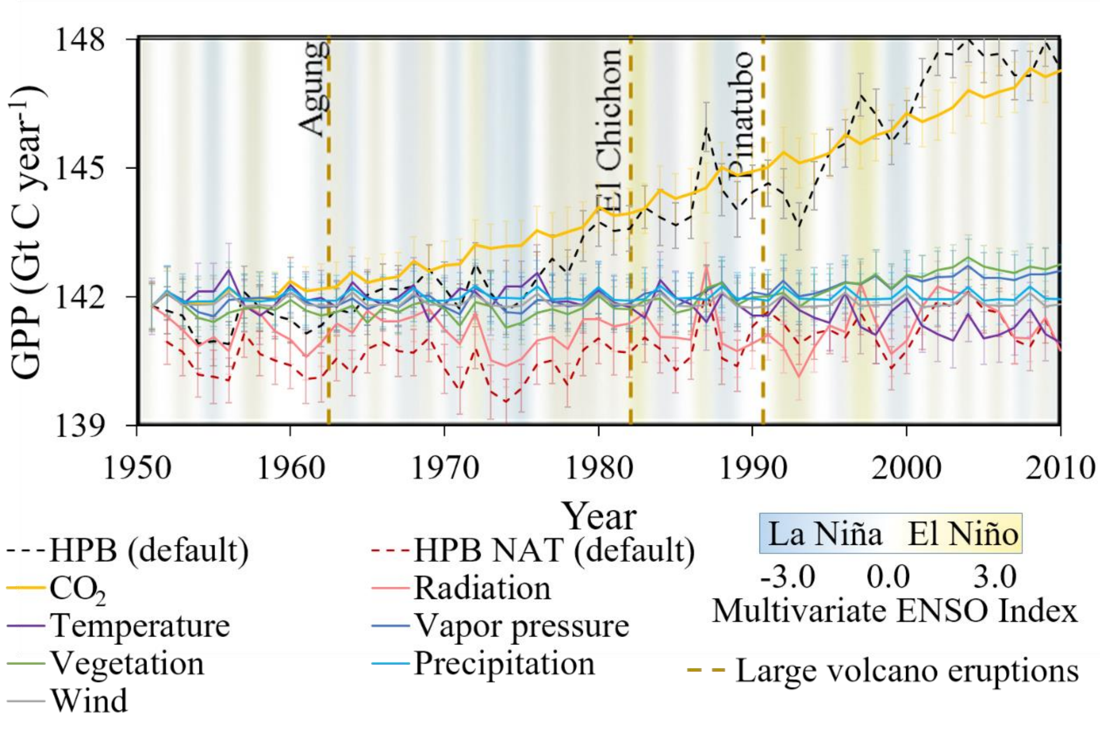

Figure 3.6. Interannual variation of gross primary production (GPP) absolute values for seven driving factors of the sensitivity experiment. The default runs of historical (HPB) and nonwarming (HPB NAT) GPP are plotted for comparison. The error bars indicate the spread of 100 ensemble members by standard deviation.

The global GPP anthropogenic effect is overall positive but varies regionally. The largest positive GPP anthropogenic effect is observed in the semi-arid regions of SH. This finding is in line with the study by Ahlström *et al.* (2015) who highlighted that the semi-arid regions dominate the positive trend of the global land uptake. The GPP anthropogenic effect may have initiated the positive trend in the semi-arid regions due to relaxed water stress and increased water use efficiency through CO_2 fertilization (Sato *et al.*, 2015). The anthropogenic effect resulted in the GPP decreases in the equatorial tropics, Southeast Asia and Europe.

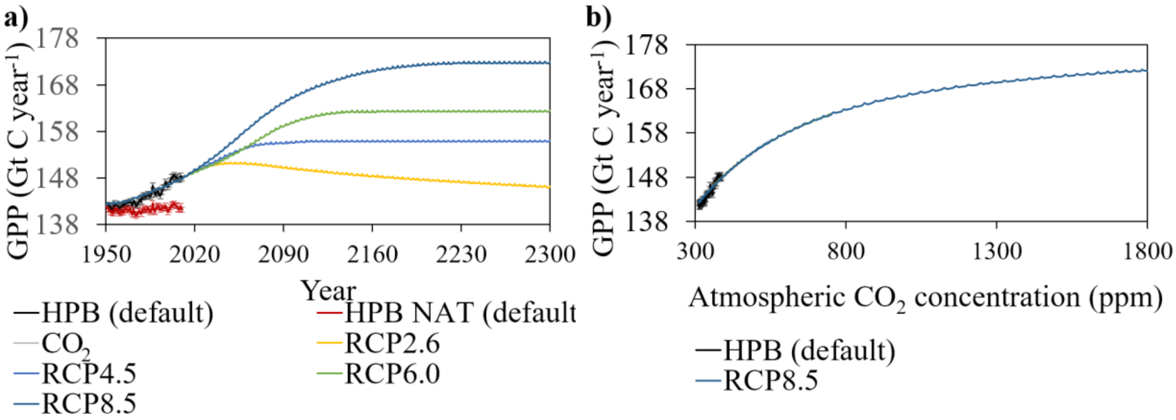

Figure 3.7. The interannual gross primary production (GPP) from the CO_2 sensitivity experiment using HPB climate simulation data and CO_2 concentration data of four Representative Concentration Pathway (RCP) scenarios as a function of (a) year and (b) atmospheric CO_2 concentration.

The sensitivity experiment of HPB climate simulation allowed identifying the drivers of GPP anthropogenic and natural effects (Figure 3.6). The main driving factors of the GPP anthropogenic and natural effects in 1952–2010 were CO_2 fertilization and shortwave radiation, respectively. Besides, the IAV of the radiation sensitivity run coupled with the ENSO events and large volcanic eruptions. E.g., the decrease in shortwave radiation contributed to the decrease in GPP after Pinatubo eruption. The global decrease in shortwave radiation had also the largest negative effect on the global GPP. Temperature contributed to the GPP positively in 1950–1960s, and negatively in the later period, the negative effect of temperature on the GPP intensified over time. Vapor pressure contributed to the GPP positively in a similar way to vegetation, and intensified over time. The precipitation had only minor and highly uncertain contribution to the GPP change. The main driving factor of the GPP anthropogenic effect, CO_2 fertilization, is expected to saturate in future at the CO_2 concentration levels over 700 ppm (Canadell *et al.*, 2007b; De Kauwe *et al.*, 2016). The extended CO_2 sensitivity run (Figure 3.7) shows that the CO_2 fertilization may saturate by year 2050–2150 depending on the RCP scenario. The maximum annual GPP in the case of RCP8.5 scenario is nearly 173 GtC year^{-1}. In comparison, the annual GPP by BEAMS in in 1982–2010 equals 145.7 ± 0.1 GtC year^{-1}.

Thus, the capability of the CO_2 fertilization effect to increase the global GPP is limited to 27.3 GtC year^{-1} from the current level of GPP.

The spatial distribution of the GPP linear trends from the sensitivity experiment (Figures 3.8 and 3.9) clarifies the mechanism of the GPP changes. CO_2 fertilization dominated the global GPP increase globally, followed by the positive effect of temperature in the northern high latitudes, shortwave radiation in Europe and negative effect of shortwave radiation in the part of South-East Asia (Figure 3.8). The CO_2 fertilization had the largest effect in the tropics. The increases in temperature and vapor pressure, and vegetation greening led to the positive GPP changes in the northern high latitudes. The increase in temperature and decrease in shortwave radiation drove the negative GPP anthropogenic effect in the tropics and Southeast Asia.

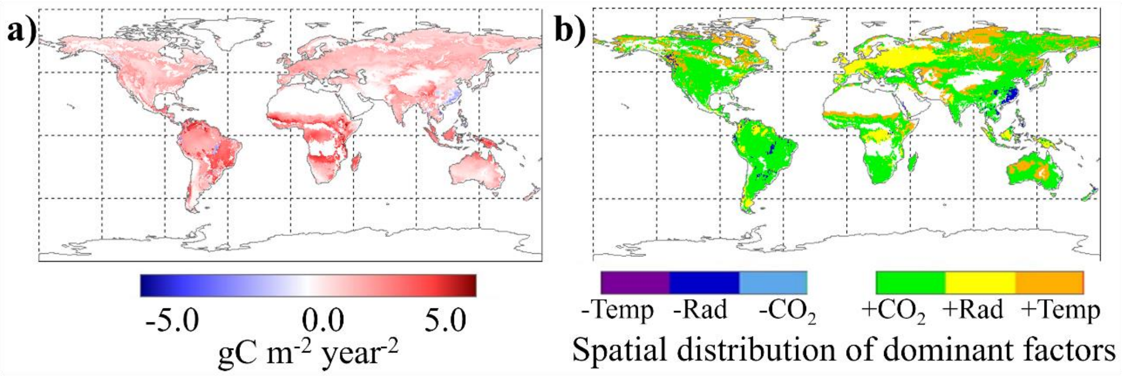

Figure 3.8. (a) The 1952–2010 linear trend (95% significance) of gross primary production (GPP) of default HPB run. (b) Spatial distribution of dominant driving factors of GPP trend defined as the driving factor from the sensitivity experiment that contributes the most to the increase (or decrease) in GPP in each vegetated grid cell. The driving factors include CO_2, temperature (Temp) and shortwave radiation (Rad). A prefix "+" of the driving factors indicates a positive effect on GPP trends, whereas "-" indicates a negative effect.

The spatial distribution of the negative GPP anthropogenic effect overlaps with the negative anthropogenic effect on the shortwave radiation (figure 3.4b). Previously, Nemani *et al.* (2003) suggested that the shortwave radiation is the main climatic constraint over the radiation-limited regions in Western Europe and the equatorial tropics. The results of the sensitivity experiment suggest that the increase in temperature had a negative GPP anthropogenic effect in Europe, while changes in precipitation and wind speed had only minor effect globally. The largest spread in the ensemble GPP estimates is in the northern high latitudes and tropics for radiation, and in the central Eurasia for temperature sensitivity runs. I provide only simple investigation of the 60-year changes, and thus, the future studies should focus on the regional distribution of the GPP anthropogenic effect and analyze the inter-decadal GPP change. In addition, more attention should be paid to the regional uncertainty.

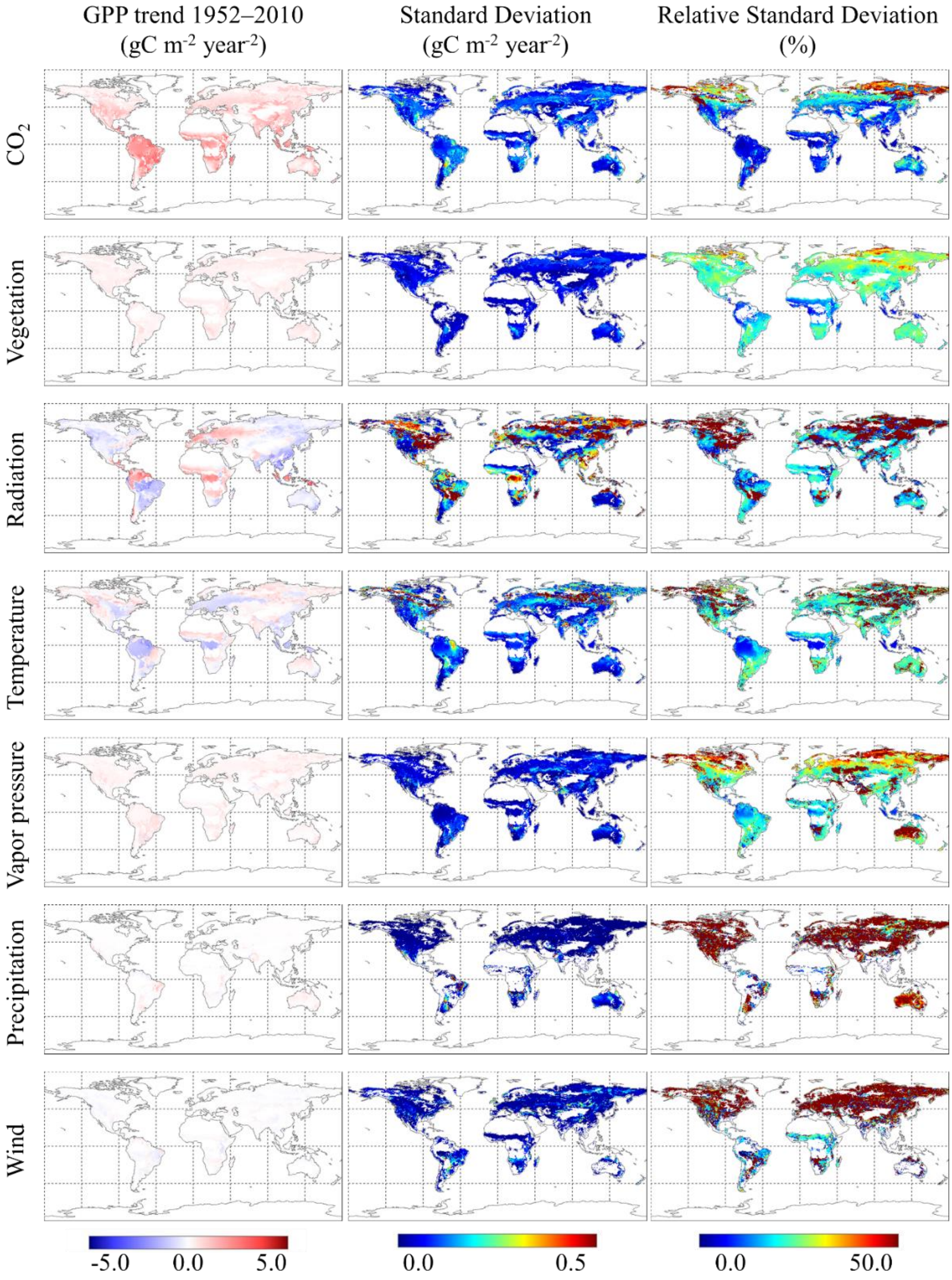

Figure 3.9. The 1952–2010 linear trends (95% significance) of gross primary production (GPP) for seven driving factors of the sensitivity experiment. The ensemble spreads are defined through standard deviation and relative standard deviation, i.e. standard deviation divided by the ensemble mean.

3.4. The future changes in gross primary production

I compared the GPP estimates of RCP8.5 CO_2 sensitivity run with that of the default future warming experiments (Figure 3.10). The +2K and +4K multi-ensemble future warming climate simulations of d4PDF correspond to the RCP8.5 scenario. Specifically, +2K set of simulations uses ΔSSTs between 1991–2010 and 2031–2050 and +4K set of simulations uses ΔSSTs between 1991–2010 and 2080–2099 in the historical and RCP8.5 experiments by the six CMIP5 models. In addition, the GHGs and aerosols values at 2040 and 2090 of RCP8.5 are utilized for +2K and +4K, respectively. Therefore, the comparison of the year 2040 and 2090 of RCP8.5 CO_2 sensitivity run with +2K and +4K default runs allows analyzing the relative contribution of CO2 fertilization effect and climate drivers to the global GPP increase.

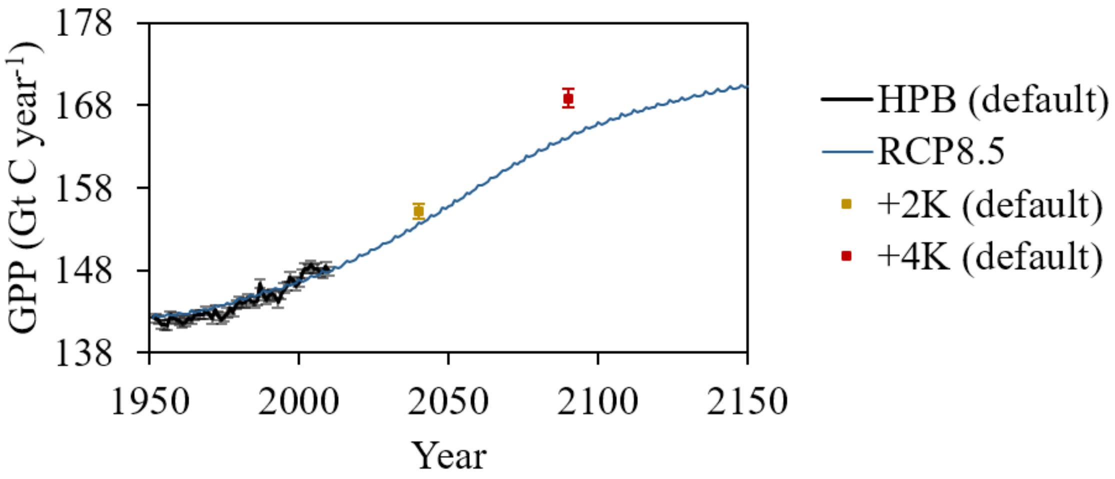

Figure 3.10. The interannual variation of gross primary production (GPP) from the CO_2 sensitivity experiment using HPB, 2K, +4K climate simulation data and CO2 concentration data of four Representative Concentration Pathway (RCP) 8.5. The error bars indicate ensemble-spread by standard deviation.

Figure 3.10 suggests that while CO_2 fertilization effect plays the major role in the current increase in global GPP (1951–2010), the role of CO_2 decreases in the future with warming of the climate, especially in +4K climate, when CO_2 fertilization effect approaches saturation. Figure 3.11 provides a spatial variation of these changes. In both future warming cases, the tropical and subtropical areas are characterized stronger positive CO_2 fertilization effect compared to the effect of climate, while the opposite is true for everywhere else. Taking into account that the GPP of default simulation is higher than that of CO_2 sensitivity experiment, it is safe to conclude that climate-driven non-tropical GPP increase is projected to take over the dominant role of global GPP increase in the future. While CO_2 fertilization chiefly drives

GPP increase in the tropics, in the future warmer climates, climate variables are projected to constrain the tropical GPP increase.

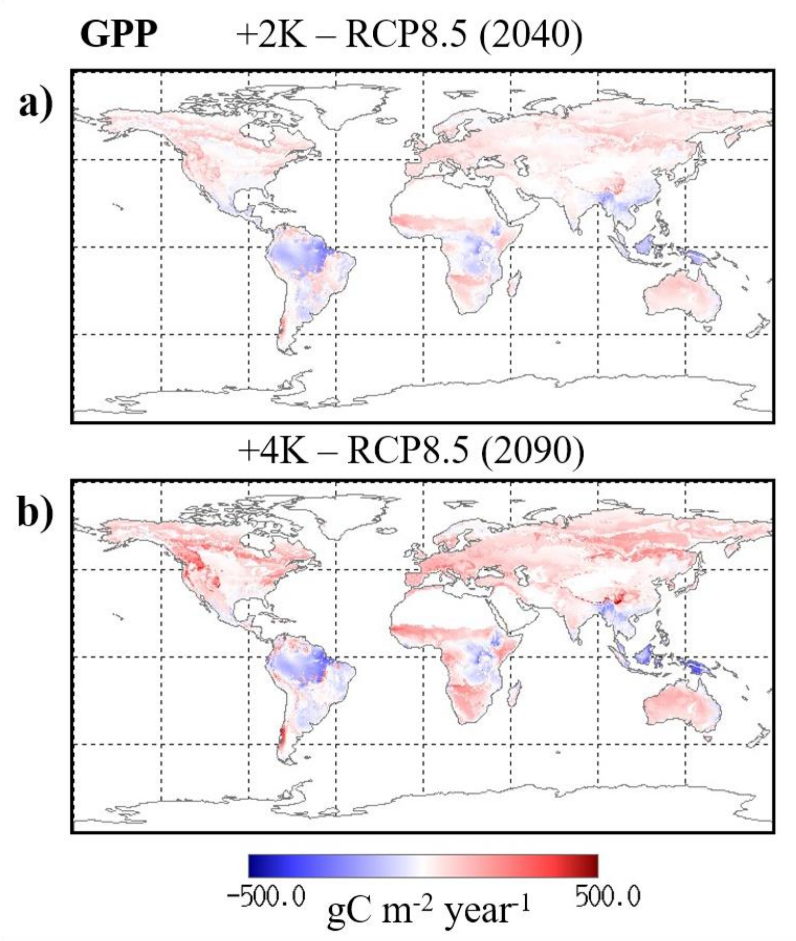

Figure 3.11. The difference between (a) +2K default GPP simulation and CO2 sensitivity experiment based on CO2 concentration data of Representative Concentration Pathway (RCP) 8.5 of year 2040 and (b) +4K default GPP simulation and CO2 sensitivity experiment based on RCP8.5 of year 2090. The sea surface, desert and ice areas are excluded. The negative values suggest stronger positive effect of CO2 concentration increase on GPP, and negative values suggest stronger positive effect of climate.

In conclusion, although currently the CO_2 fertilization drives the global anthropogenic GPP effect, its relative contribution decreases with warming in future climates. Future studies should investigate the relative contributions of other climate drivers on GPP in +2K and +4K climates.

Chapter 4

The changes in global terrestrial ecosystem respiration with climate warming

4.1. Evaluation of the simulated terrestrial ecosystem respiration

The global terrestrial ecosystem respiration (TER) remains the least well-constrained terrestrial flux in the biosphere models and observations are sparse (Bond-Lamberty & Thomson, 2010; Tramontana *et al.*, 2016). As a result, the global TER estimates by the models and observations are inconsistent (Carvalhais *et al.*, 2014). I compared the TER anomaly and TER anthropogenic effect estimated by BEAMS with atmospheric carbon growth and alternative global TER estimates currently available (Figure 4.1). The 1960–2010 linear trends for TER products are highly divergent, starting from a slope of 0.08 GtC year^{-2} in observation-based respiration by Hashimoto *et al.* (2015) to 0.26 GtC year^{-2} in TRENDY model-ensemble ($p<0.001$). The anomaly of TER anthropogenic effect by BEAMS is amongst the TER anomalies by observation- and model-based estimation approaches. It is essential to note that the anomaly in TER anthropogenic effect cannot be directly compared to the anomalies in TER, because it does not include the interannual TER variability. In addition, the fact that Hashimoto *et al.* (2015) estimates include R_S, not TER should be kept in mind.

The comparison provides verification of reasonable TER estimate by BEAMS compared to other data sets, and the evidence of the increasing trend of the TER anthropogenic effect in the recent decades. The largest increase in the TER anomaly is the TRENDY suit of the prognostic models. Because the R_A largely depends on the GPP, the overestimation of the GPP due to ovestimation of CO_2 ferilization effect (Smith *et al.*, 2015) leads to overestimation of R_A and thus, TER. In addition, the little constraint by the input data causes the large spread in global TER estimates due to differences in model structure. The TER estimate by FLUXCOM shows the lowest slope of linear trend and smallest interannual variation among data set similar to that of GPP (Table 3.1).

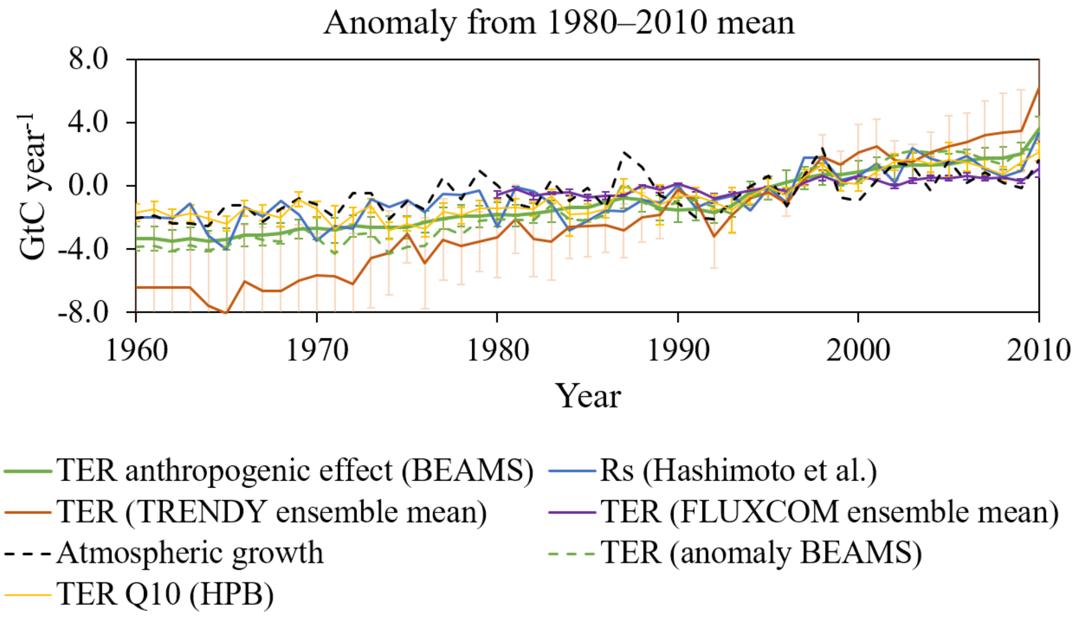

Figure 4.1. The interannual variation of the terrestrial ecosystem respiration (TER) anthropogenic effect estimated by BEAMS and TER, TER Q10 effect estimated using d4PDF soil moisture, soil respiration (R_S) anomalies by various approaches from the 1980–2010 mean. The anomaly of atmospheric carbon growth is plotted for comparison.

4.2. The comparison between preindustrial and future warming simulations

In order to determine the terrestrial ecosystem respiration (TER) anthropogenic effect, it is first necessary to investigate the effect of anthropogenic activities on global climate (Figure 4.2). In the future warmer climate the shortwave radiation at surface decreases with larger decrease in +4K compared to +2K climate simulation. The dimming is spatially heterogeneous—larger decrease of shortwave radiation in the northern high latitudes, continental Southeast Asia and central Africa. The shortwave radiation decrease is consistent with increase in precipitation, especially in the northern high latitudes and eastern Eurasia. The precipitation and shortwave radiation anthropogenic effect differs between +2K and +4K climates in Australia. This suggests strong cloud-radiative feedbacks in the future warmer climates and a possibility of large regional changes in future precipitation. The changes in air temperature and vapor pressure are consistent with those of the historical climate of 1951–2010 (Figure 3.4b). Air temperature increases globally with the larger increase in the north, and vapor pressure increases globally with the largest increase in the tropical and subtropical areas of the Southern Hemisphere. These fluctuations again indicate large future changes in the global water cycle via spatial change of relative humidity.

Bond-Lamberty *et al.* (2018) provided multiple lines of evidence of rising heterotrophic respiration on a global scale. Authors suggested that the increases are climate-driven. I analyzed the probability density functions (PDFs) of the multi-ensemble TER estimates by BEAMS in +2K and +4K climates in comparison to HPB NAT (Figure 4.3). The PDFs confirmed an increase of TER magnitude up to 8 and 18% in +2K and +4K climates, respectively (Figure 4.3a). The interannual TER variability and occurrence of years with extremely high global TER also increases in warmer climates (Figure 4.3b).

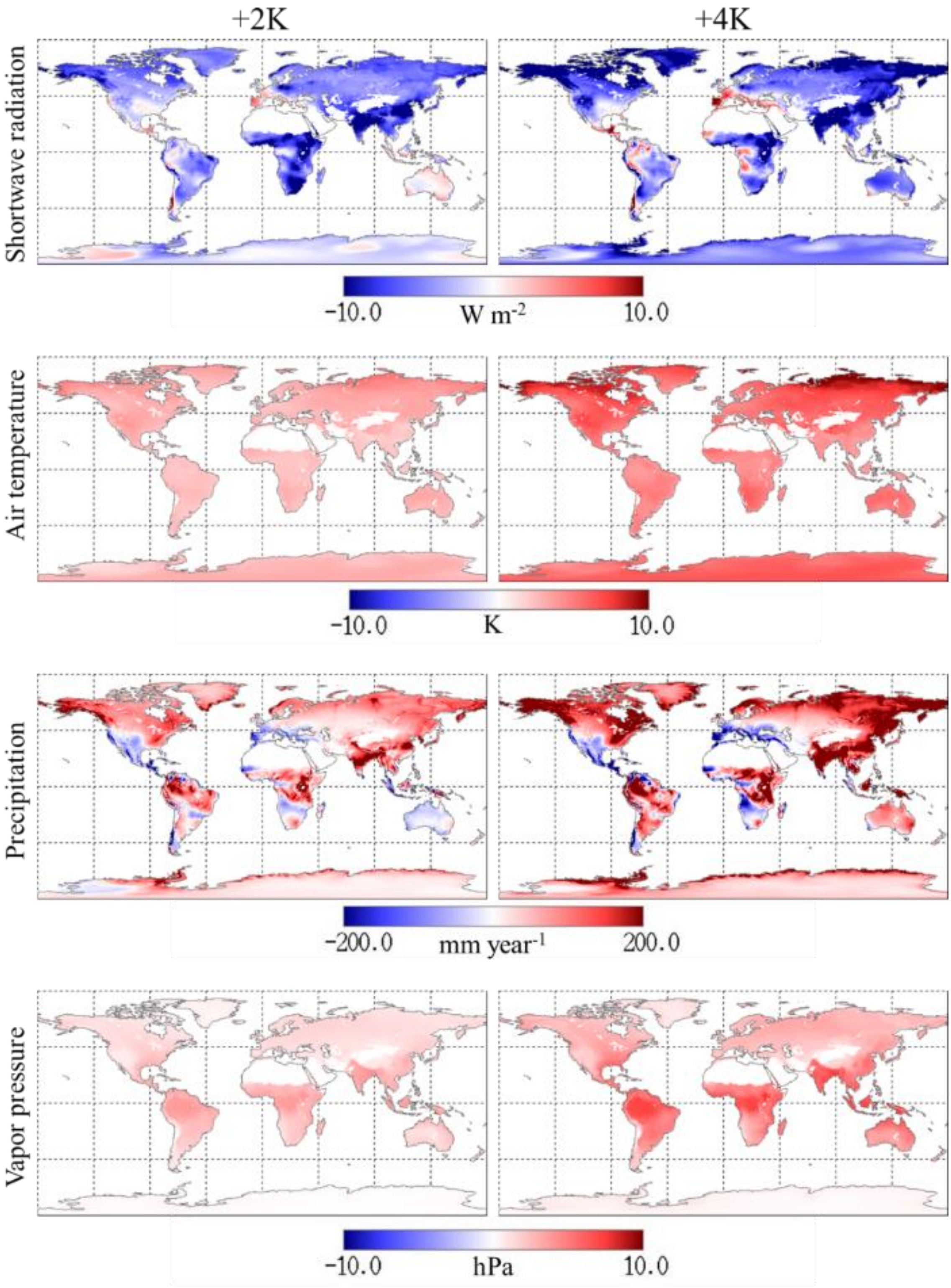

Figure 4.2. Spatial distribution of the ensemble means of the anthropogenic effect (difference between +2K or+4K and HPB NAT) on the climate variables (sea surface and desert areas are excluded).

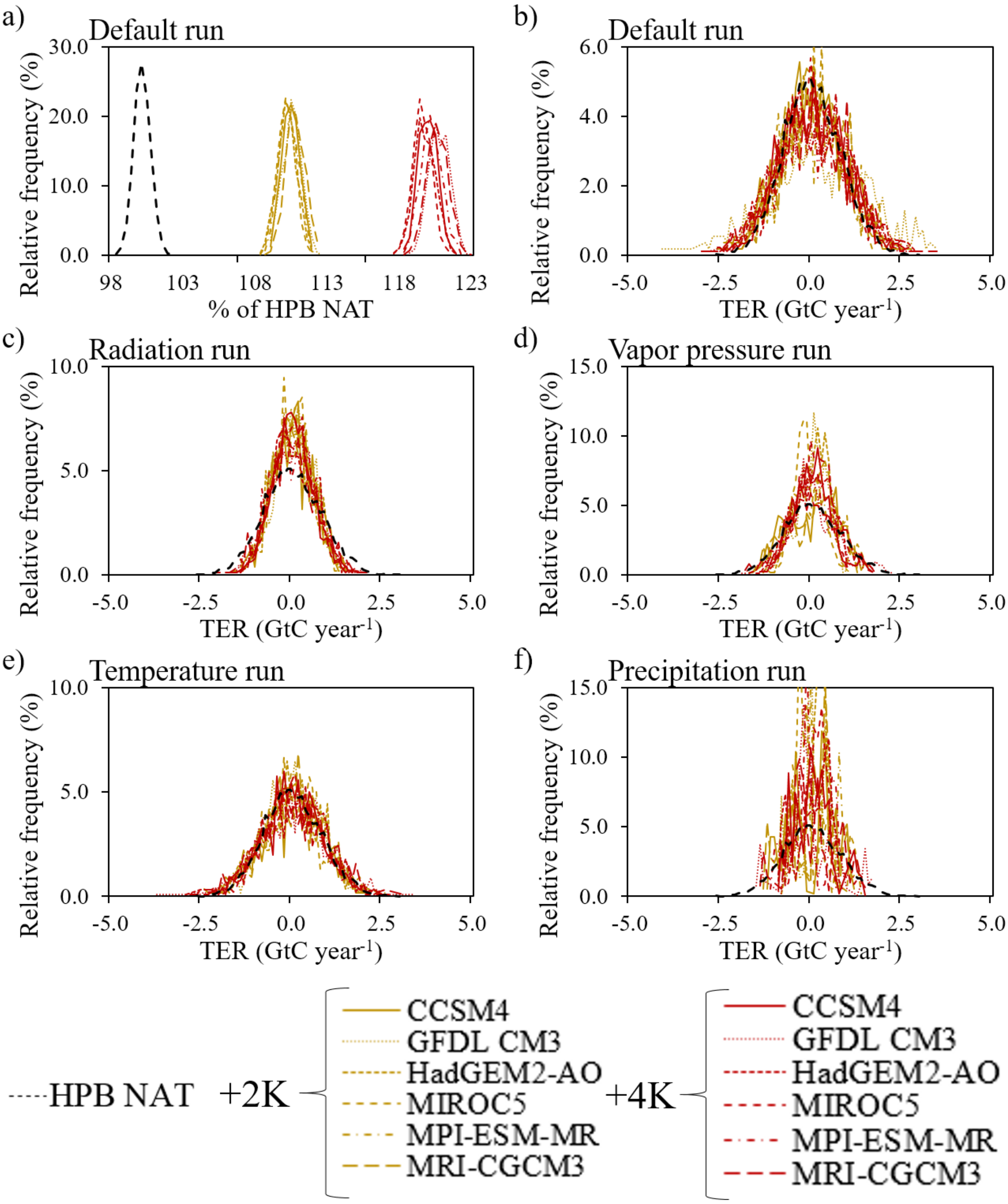

Figure 4.3. Probability density functions of global terrestrial ecosystem respiration (TER) in HPB NAT, +2K and +4K climates based on (a) absolute TER values, (b) TER anomalies of the default experiment and (c–f) TER anomalies of future sensitivity experiments for shortwave radiation, vapor pressure, temperature and precipitation (5900 years of HPB NAT, 6 ×540 years of +2K and 6 × 900 years of +4K simulations).

The future climate simulations of d4PDF in addition to perturbations include the uncertainty of CMIP5 models. Thus, the increase in interannual TER variation shown in Figure 4.3b includes the uncertainty in future TER. In order to distinguish the probabilistic increase in interannual TER variation from the increase in uncertainty, it is necessary to treat the relative frequencies of sic CMIP5 models used in d4PDF separately (Figure 4.3b and c). The GDFL CM3 model grounds the largest spread of global TER estimates in +2K that transfers into a larger spread of global TER estimates in +2K than in +4K simulation. On the other hand, when the GDFL CM3 based TER estimates are excluded, the interannual variation of global TER appears larger in +4K compared to cooler climates. Overall, the interannual TER variation and occurrence of years with extremely high global TER increases in warmer climates.

The TER sensitivity experiment (Figure 4c–f) provides the reasoning of these changes. The radiation run does not display any large impact of the changes in shortwave radiation on the global TER in the future. To the best of my knowledge, there is no evidence of the direct control of shortwave radiation over TER. Its control is indirect via increase in GPP according to the LUE concept. Because only one R_A largely depends on GPP, the sensitivity of TER to radiation is insignificant. The anthropogenic effect on the shortwave radiation remains poorly understood, although several studies report recent trend of global dimming due to the intensifying water cycle and anthropogenic aerosol emissions (Wang *et al.*, 2017; Wild, 2012; Zou *et al.*, 2016). Shortwave radiation is not anticipated to cause extreme low or high values of global GPP unless the volcano eruption occurs. Because the d4PDF data does not involve any probabilistic occurrence of volcano eruption, there is no increase in global TER interannual variation compared to HPB NAT. Finally, the anthropogenic effect on shortwave radiation at surface is secondary, compared to other climate variables, such as temperature and precipitation. The vapor pressure and precipitation runs display an elongation towards high global TER and appears multimodal in +2K and +4K simulations. The multimodality might be related to the large model spread of the regional changes in vapor pressure and precipitation and, thus, uncertainty in the anthropogenic effect in future climates (Gettelman & Sherwood, 2016). Temperature run displays the largest increase in the interannual variability of global TER and, specifically, an occurrence of years with extremely high and low global TER.

Figure 4.4 illustrates the latitudinal variation of the TER, TER anthropogenic effect and relative TER anthropogenic effect. Despite the peak of the global aboveground biomass, and thus GPP in the tropics, the tropical peak in TER anthropogenic effect does not appear apparent (Figure 4.4b). Moreover, the relative TER anthropogenic effect is the highest in the high latitudes (Figure 4.4c).

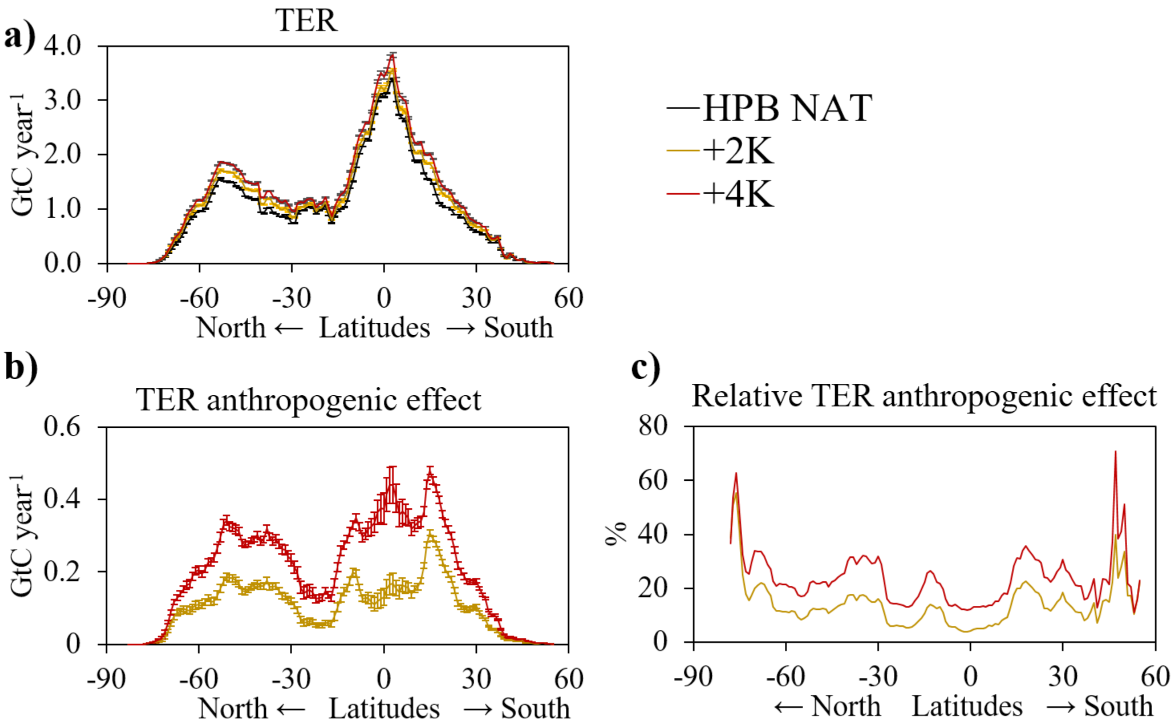

Figure 4.4. Latitudinal variation of the average global terrestrial ecosystem respiration (TER) in three climate simulations (a), the +2K and +4K TER anthropogenic effect (b) and relative TER anthropogenic effect relative to the ensemble-mean TER estimated by BEAMS (c). Calculations are based on 5900 years of HPB NAT, 3240 years of +2K and 5400 years of +4K simulations. The shading indicates the longitudinal variation by standard deviation.

Figure 4.5 illustrates the spatial distribution of TER in the regions that are accountable for the extreme increase in the global TER interannual variation. The extreme increase occurs in the tropical and sub-tropical areas of the Southern Hemisphere and mid- to high latitudes over 45 degrees north. Contrariwise, the semi-arid regions of southern North and South America seem to have negligible effect on the increase in global TER variation. The sensitivity experiment indicates that all analyzed climate drivers contribute to the increase in amplitude of the global TER variation in the tropics. The increase in the amplitude of the global TER in the mid- to high latitudes differs amongst +2K and +4K climate simulations. In the +2K, all climate drivers play role in the increase of the global TER interannual variation, and in +4K, only temperature plays a significant role. Other regions that are shown not to contribute to the extreme increase in the global TER variability, perhaps contribute to the global TER and TER anthropogenic effect only insignificantly.

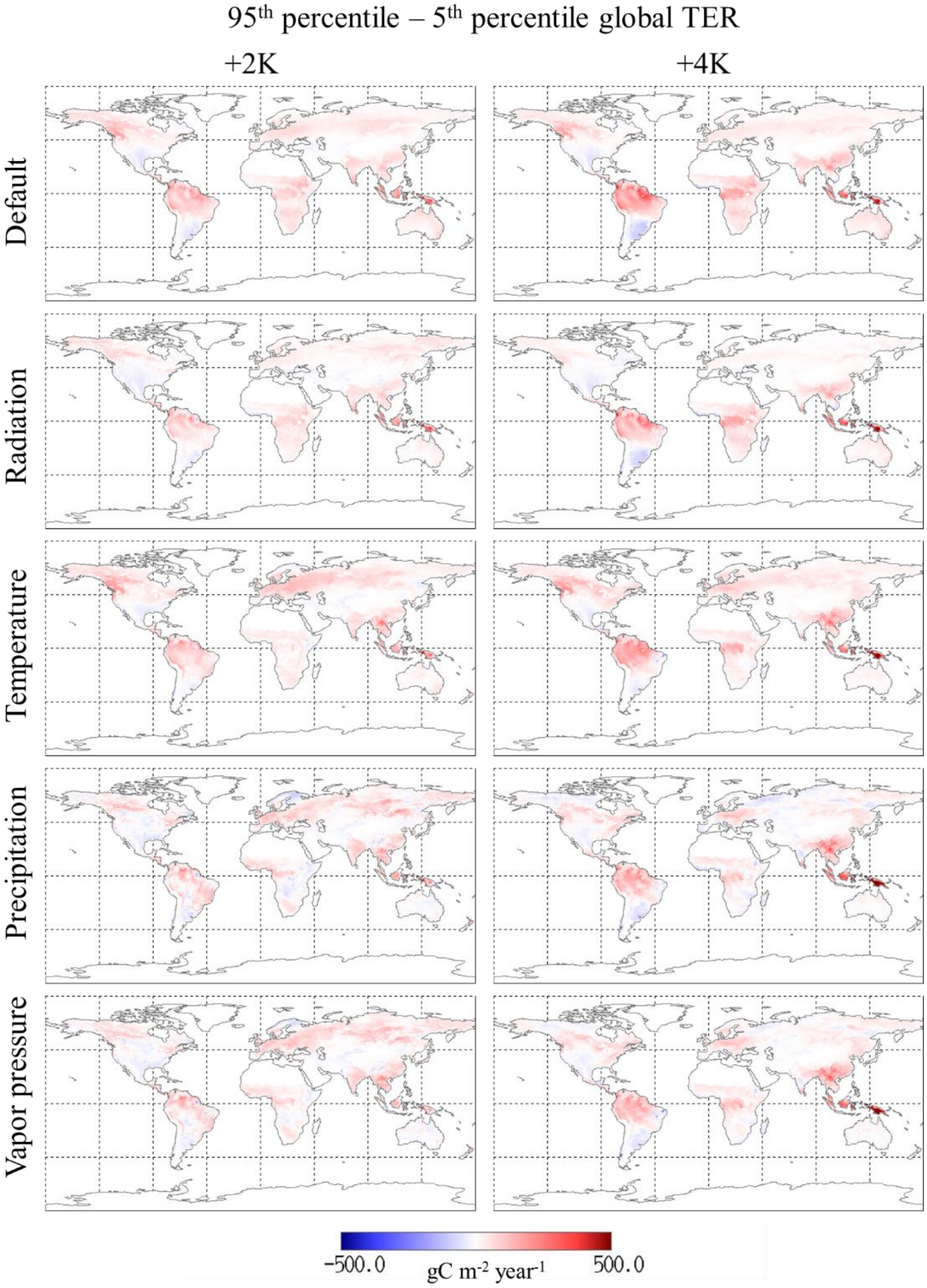

Figure 4.5. Spatial distribution of the terrestrial ecosystem respiration (TER) corresponding to the difference between the 95th and 5th percentiles of global TER in +2K and +4K in default and sensitivity experiments based on 3240 years of +2K and 5400 years of 4K simulations.

The two parts of TER—R_A and SD—have uneven responce to the climate changes. While Ra relates to the increases in GPP, SD relates to the available litter fall mass and microbial activity. In order to clarify the mechanism of the increasing TER, to ensure that the results are not sensitive to averaging over the ecosystems, and to distinguish the climate drivers of extremely high global TER, the extremely high global TER in the default and sensitivity experiments and spatial distributions of the corresponding climate drivers were analyzed (Figure 4.6). The regional responses of the extreme global TER in cases of in +2K and +4K climates are inconsistent. The extremely high global TER is dominated by northern mid-latitudes in +2K, and tropics in +4K climate.

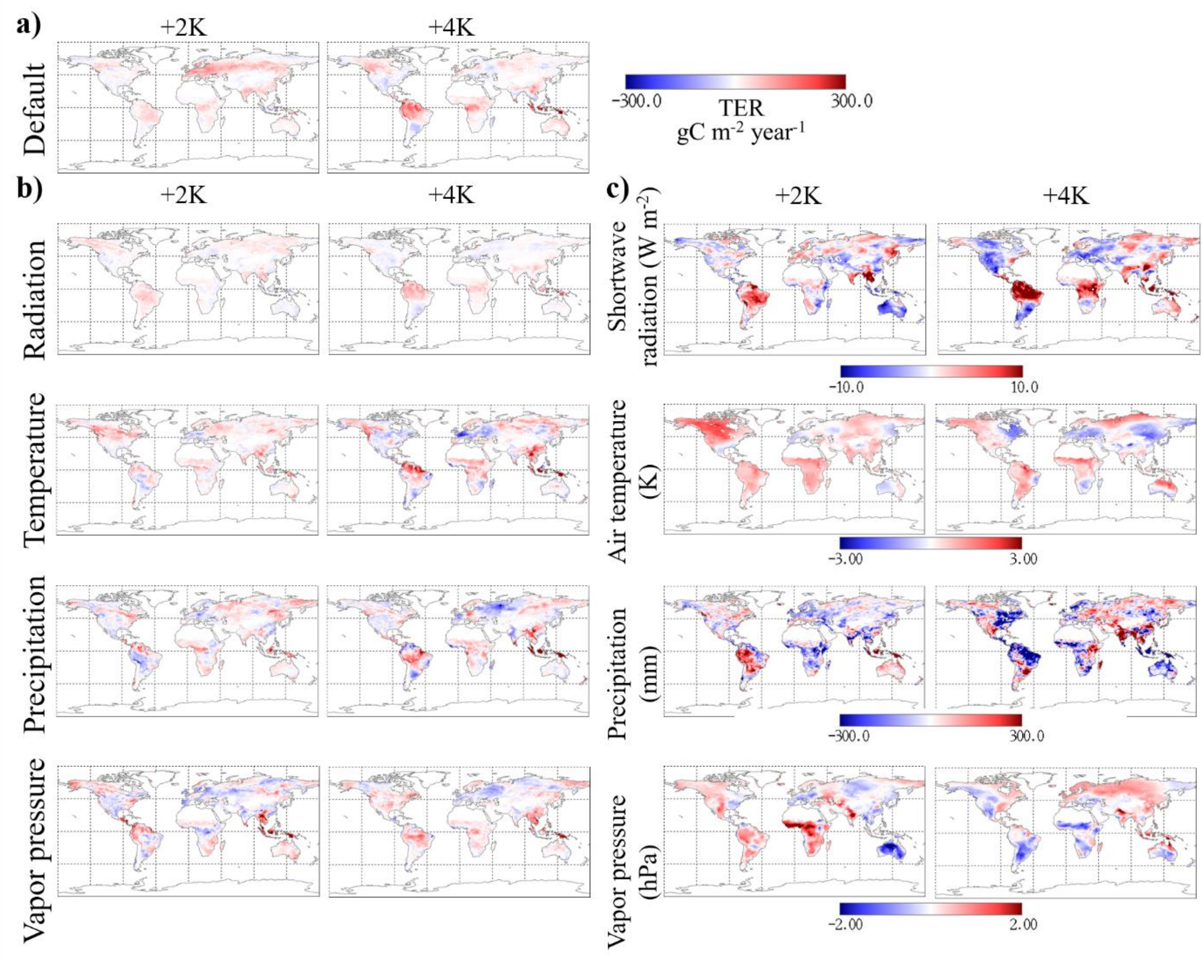

Figure 4.6. Spatial distribution of the differences between 95th percentiles and medians of global TER averaged over all years of +2K and +4K climates in (a) default and (b) four sensitivity runs. (c) The spatial distribution of the climate variables that correspond to the differences between 95th percentiles and medians of global TER in four multi-ensemble sensitivity runs. Figures are based on 3240 years for +2K and 5400 years for +4K.

The spatial distribution of the vast shortwave radiation increases corresponds to that of extremely high TER. This suggests, as expected, that the overall increase in the GPP, and thus, litter mass results in higher Ra, and thus TER. The increase in air temperature in the +2K climate suggests the increase in both GPP-driven increase in both Ra and SD due to longer season and SD via Q10 dependency in the mid-latitudes and only SD via Q10 dependency in the tropics. In even warmer +4K climate the mechanism of the mid-latitudinal TER increase of +2K spreads further to the northern high-latitudes and simultaneously weakens in the mid-latitudes. Vapor pressure sensitivity run shows that increased VPD in the grasslands and agricultural lands of India and central Africa, as well as Europe may dominate extremely high global in +2K, and increased VPD in the southern Hemisphere, including both tropics and semi-arid and arid areas, may dominate high global TER in +4K climate. Finally, increased precipitation in tropics of Africa and Southeast Asia and decreased precipitation in the northern high latitudes causes extremely high global TER in +2K, while very low precipitation in the tropics causes extremely high global TER in +4K climate. The TER response to the changes in water availability is rather complex and poorly understood. Both Ra and SD depend on water availability—decreased precipitation and increased droughts, lead to stomatal closure, decreased GPP, and, thus, decreased Ra and TER (van der Molen *et al.*, 2011) on the one hand, and increased tree mortality, consequently, increase litter fall, and, thus, increased SD and TER on the other hand. In addition, SD is on the chemical composition, microbial community composition and acclimation. (van der Molen *et al.*, 2011). Overall, the major driver of high global TER is temperature, followed by water-related climate variables.

4.3. Sensitivity of terrestrial ecosystem respiration to future climate change by alternative approaches

In order to confirm the TER estimates in the future warming climate simulations, I used the empirically derived statistical relationships of R_S with four climate drivers, air temperature, precipitation, soil temperature and moisture, derived by Hursh *et al.* (2017). Figure 4.7 illustrates the PDFs of global soil respiration (RS) in HPB NAT, +2K and +4K climates. Based on the availability of spatial coverage of data, in total I analyzed R_S estimates based on 39049 pixels of air temperature, 39086 pixels of precipitation, 38429 pixels of soil temperature and 30473 pixels of soil moisture. Because of large difference in the number of available pixels between climate drivers, the results of TER estimates may be only used for evaluation of the BEAMS-based TER estimates, not for the analysis.

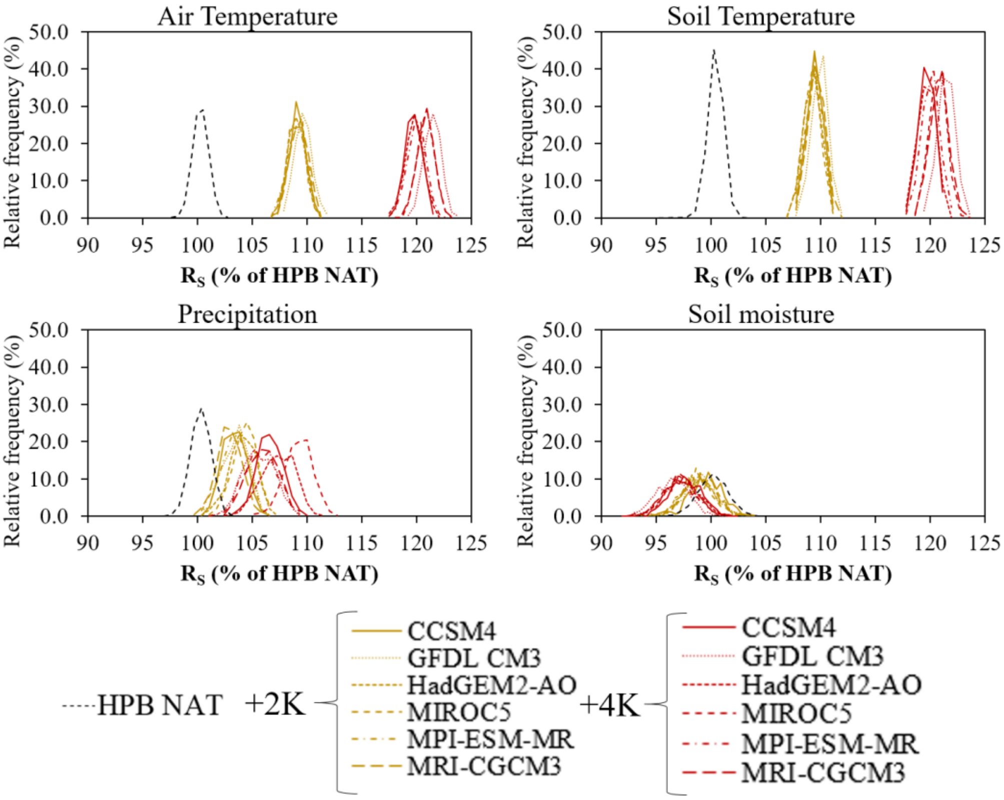

Figure 4.7. Probability density functions of global soil respiration (R_S) in HPB NAT, +2K and +4K climates based on R_S estimated using the statistical relationships with four climate drivers determined by Hursh *et al.* (2017). 5900 years of HPB NAT, 6 × 540 years of +2K and 6 × 900 years of +4K simulations are used.

Consistent with the findings described in the Section 4.2, air and soil temperatures explain the R_S increase in the future warmer world. Together with the increase in magnitude, IAV of R_S increases. Precipitation drives a small increase in global R_S, while soil moisture changes suggest a decrease in mean R_S with warming. Hursh *et al.* (2017) suggested a quadratic soil moisture function to estimate R_S as opposed to the linear functions based on the other three climate drivers, warning on the consequent increase in root mean square error. In addition, there were the least number of soil moisture pixels available for the analysis. Overall, the figure shows a large uncertainty in climate driven statistically estimated global RS in future climate simulations. The largest uncertainty exists for soil moisture- and precipitation-based estimates and +4K air and soil temperatures. In Section 4.2, I came to the analogous conclusion in regards of precipitation and vapor pressure sensitivity experiments (Figure 4.3c–f).

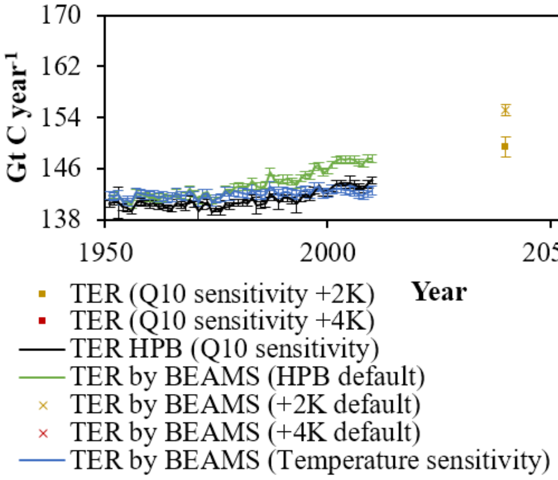

Figure 4.8. The interannual variation of terrestrial ecosystem respiration (TER) from the BEAMS and Q10 effect on TER based on d4PDF soil temperature data simulated for Representative Concentration Pathway (RCP) 8.5 scenario. The error bars indicate ensemble-spread by standard deviation.

Finally, because temperature was shown to be the major driver of the TER anthropogenic effect, I compared the BEAMS-based TER estimates with the d4PDF-based empirically estimated Q10 effect on TER using equation 3. Figure 4.8 confirms the increasing role of temperature via Q10 in the future warming climates. Both the BEAMS temperature sensitivity experiment and Q10 effect on TER suggest that in 1951–2010, only minor part of TER increase was affected by temperature. However, the contribution of temperature in driving TER increases with warming exponentially. This means that the temperature will play larger role in TER and, thus land carbon uptake in the future warmer climates.

Chapter 5

Discussion

5.1. The gross primary production anthropogenic effect

I provide the evidence of the anthropogenic effect on the global terrestrial gross primary production (GPP) by combining the advantages of the diagnostic approach and the large-size ensemble climate data. The GPP of the HPB with the associated climate input-data uncertainty is significantly different from the GPP of the HPB NAT. While the multi-member ensemble spread constantly remained 0.6 GtC year^{-1} throughout the study period, the GPP anthropogenic effect, increased from 0.9 ± 0.1 GtC year^{-1} in 1952–1961 to 6.1 ± 0.3 Gt year^{-1} in 2001–2010. I decomposed the temporal change in the global terrestrial GPP into two parts—the long-term trend and the interannual GPP variability, i.e. GPP anthropogenic and natural effects. The long-term GPP trend corresponded to the change in CO_2 concentration, suggesting that CO_2 fertilization was the main driver of the GPP anthropogenic effect during the study period. Likewise, Sitch *et al.* (2015) reported that increasing CO_2 concentration drives the increasing terrestrial carbon uptake. The extended sensitivity experiment (Figure 3.6c) shows that CO_2 fertilization is going to saturate by 2050–2150 depending on Representative Concentration Pathway (RCP) scenario. The interannual GPP variability corresponded to the changes in shortwave radiation (Figure 3.6a). The model results suggest that shortwave radiation is the main driver of the GPP natural effect. The GPP peaks of both default HPB and radiation sensitivity runs coincide with El Niño Southern Oscillation (ENSO) events: positive peaks covariate with El Niño and negative peaks–with La Niña. Especially large increases in GPP occur during 1987–1988 and 1997–1998 El Niño events. This increase can be explained by radiation anomalies alone (Figure 3.5) and is in line with existing model-based studies (Ichii *et al.*, 2005). The large volcano eruptions contribute to the changes in global terrestrial GPP by altering the response of GPP to ENSO. E.g., the eruption of El Chichon in 1982 and Pinatubo in 1991 suppressed the effects of 1982–1983 and 1991–1992 El Niño on GPP, respectively. The volcano eruptions influence the incoming shortwave radiation by releasing the aerosols into the atmosphere. The ENSO events are related to the total cloudiness fraction of the sky, and thus, shortwave radiation at surface in the tropics. The strong radiation control over vegetation growth in the tropics has been previously acknowledged by Nemani *et al.* (2003) and Ichii *et al.* (2005). Because of the large tropical biomass and production, the radiation control over GPP in the tropics translates to the control over global GPP. The variation in shortwave radiation together with the volcano activity are the “natural” forcing that controls ENSO via variability of the SST anomaly (Liu *et al.*, 2015). Although the coupling of shortwave radiation with ENSO in determining the GPP is currently a topic of the active research (Zhang *et al.*, 2019a), and the mechanism is yet to be clarified, the model results suggest that two factors, CO_2 fertilization and shortwave radiation, explain nearly entire GPP change in 1952–2010.

The d4PDF data set based on the multi-member ensemble climate simulations indicates a decrease in surface shortwave radiation with warming. Despite that, the biosphere model based on the LUE approach and forced with d4PDF data suggest the increase in GPP with warming (Figure 3.5), thus, implying that the negative radiation effect on GPP is being canceled by the positive effect of CO_2 fertilization (Figure 3.6). The GPP anthropogenic effect appeared spatially heterogeneous. The CO_2 fertilization dominates the GPP increase globally, the decrease in shortwave radiation drives the negative GPP anthropogenic effect in Southeast Asia and positive effect in Europe, and temperature increase drives the positive effect in high latitudes (Figures 3.8 and 3.9). The relaxed water stress via increased water vapor and precipitation, and increased water-use efficiency via CO_2 fertilization effect are likely to drive the positive GPP effect in the semi-arid regions.

The results of BEAMS simulations suggest that the decrease in shortwave radiation had a strong negative feedback on global GPP (Figure 3.6). The shortwave radiation at surface depends on the atmospheric aerosols, water vapor and cloud cover. The positive anthropogenic effect on shortwave radiation due to increased anthropogenic aerosols and water vapor in the atmosphere has been reported elsewhere (Boucher *et al.*, 2013; Richardson *et al.*, 2018). The current understanding of the cloud-radiative feedbacks to climate change remains insufficient. The cloud formation scheme is the largest source of disagreement in the GCMs: the CMIP5 models agree that the cloud feedback is positive, but disagree on its magnitude (Ceppi *et al.*, 2017; Dessler, 2010; Gettelman & Sherwood, 2016). The satellite observations do not provide sufficient evidence on the temporal surface shortwave radiation trends (dimming or brightening), although in the majority, they are consistent with the model simulations (Norris *et al.*, 2016; Trenberth & Fasullo, 2009). The linear trends of shortwave radiation by global reanalyses (1951–2010 and 1982–2010) do not agree on the sign of the trends (Figure 3.1a). The decrease in shortwave radiation with warming simulated by the MRI-AGCM in d4PDF is consistent with the simulations by most GCMs, although, Li *et al.* (2013) highlighted the existence of large regional biases of the annual means of shortwave radiation in the modern GCMs.

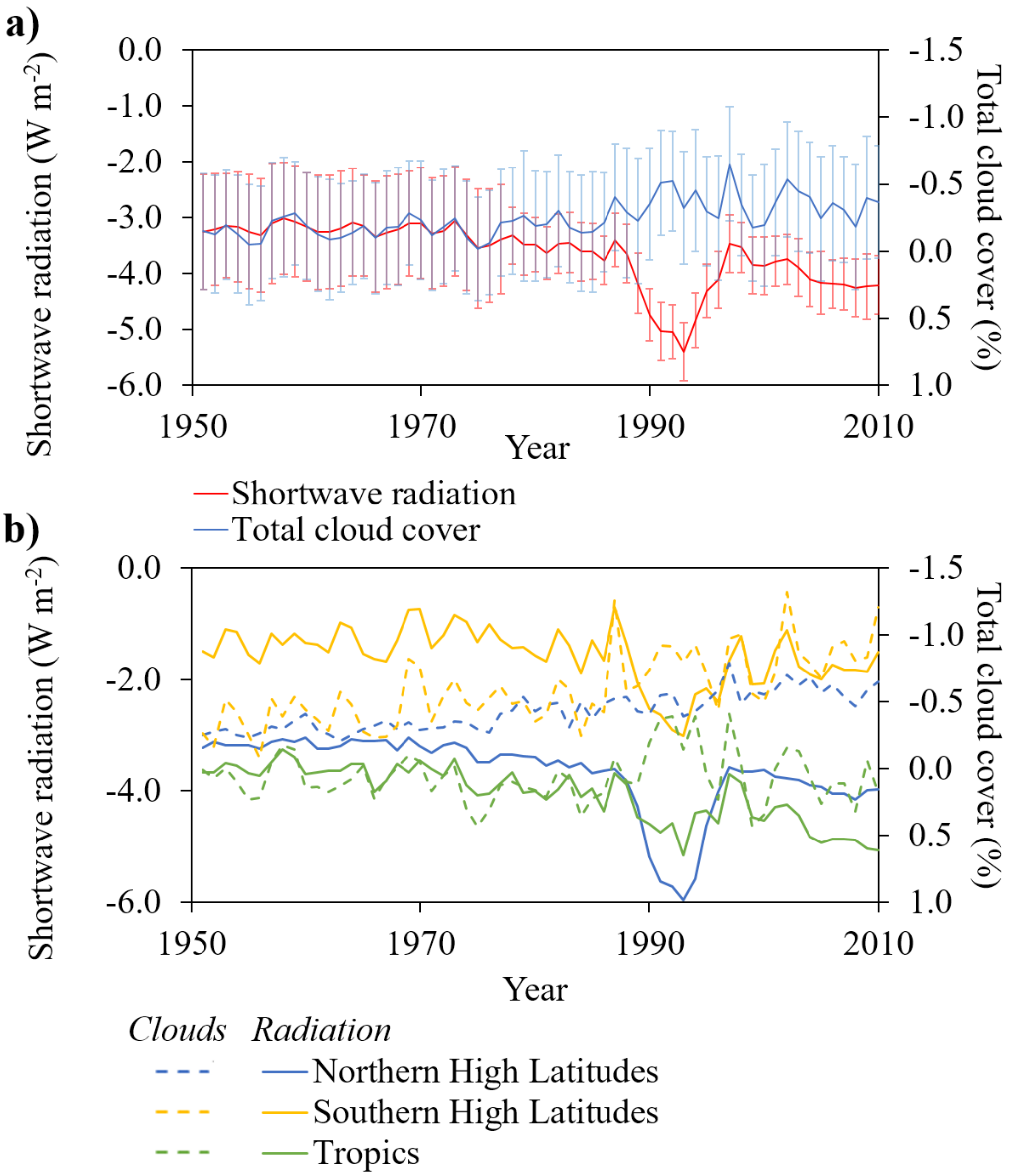

Figure 5.1. (a) Interannual variation of 100-member ensemble means of the anthropogenic effect (difference between HPB and HPB NAT simulations) on global surface shortwave radiation and total cloud cover from d4PDF data set. Error bars indicate standard deviation of 100 ensemble members. Sea surface, desert and ice areas are excluded.(b) same for the Northern High Latitudes that correspond to region over 25N, tropics—to region 25S–25N and Southern High Latitudes—to the region over 25S. Sea surface, desert and ice areas are excluded.

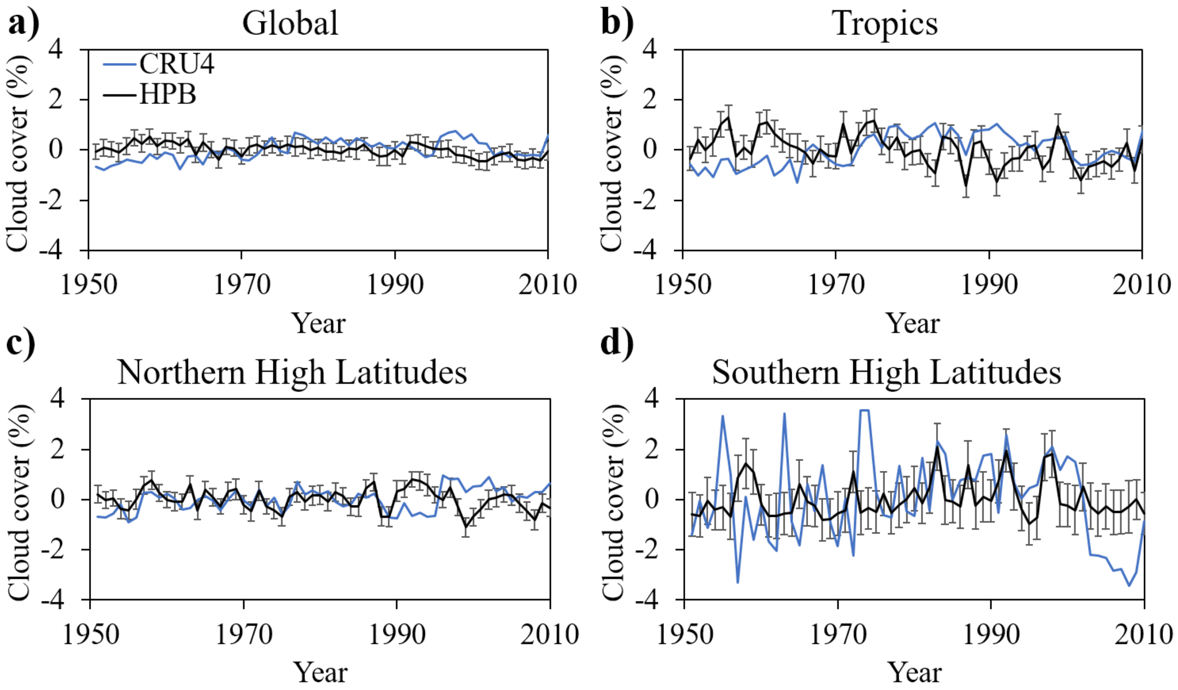

Figure 5.2. Interannual anomalies of total cloud cover from CRU TS 4.03 and d4PDF (sea surface, desert and ice areas are excluded) based on 1951–2010 mean. HPB indicates ensemble-mean of the historical simulation d4PDF data with error bars indicating standard deviation of 100 ensemble members. (a) Global mean, (b) mean of the tropics corresponding to region 25S–25N, (c) Northern High Latitudes—region over 25N, and (d) Southern High Latitudes—region over 25S.

The d4PDF trends in shortwave radiation are not universally consistent with trends in the total cloud cover and are spatially divergent (Figure 5.1). The comparison of cloud cover of d4PDF and an observation-based data set CRU TS 4.03 suggests reasonable reproducing of overall interannual variation of cloud cover although with discrepancy in the SH, especially in 1991–2010 (Figure 5.2). The future study would benefit from including a GCM that has an alternative cloud formation scheme from that of the MRI-AGCM, in order to account for the model uncertainty. Besides, although the warming increases cloud cover and, thus, decreases surface shortwave radiation, it also increases the diffuse component of radiation (Kanniah *et al.*, 2012; Mercado *et al.*, 2009). Diffuse radiation enhances GPP because diffuse light can more effectively penetrate the canopy. It is yet uncertain to what degree the two feedbacks, decreasing total shortwave radiation and increasing diffuse component compensate each other. In this study, I did not focus on the cloud-surface radiation, as well as aerosol-surface radiation feedbacks. However, the finding of the major role of interannual variation in surface shortwave radiation on GPP highlights the necessity of such studies in the future. Boucher *et al.* (2013) reported that clouds and aerosols are the largest source of uncertainty in the estimates of Earth's changing energy budget. I encourage future studies to make use of currently available stationary and satellite data in order to understand the mechanism of GPP feedback on the anthropogenic changes in clouds and aerosols both temporally and regionally.

This study is pioneer to apply the large-size ensemble climate simulations to estimate the long-term GPP. Previously, the d4PDF was used only to study the effect of climate change on the crop economic production (Iizumi *et al.*, 2018). Consequently, there is a need to summarize the limitations of the d4PDF surface data use in the studies of carbon-climate feedbacks. First, the HPB NAT climate simulation of d4PDF represents the climate without historical warming, and thus it uses detrended SSTs and constant preindustrial concentrations of GHGs, aerosols and ozone. However, HPB NAT simulation does not account for the effect of anthropogenic climate change on the interannual climate variability. In this study, I found that the climate variables of both HPB and HPB NAT simulations peak at ENSO events. The question of how climate change affects the climate variability in terms of ENSO is yet unanswered because the ENSO signal remains both in HPB and HPB NAT simulations via IAV of the SST. Thus, the d4PDF is beneficial for the studies of the effect of the long-term climate change on the global carbon fluxes rather than their interannual-to-decadal change. Second, shortwave radiation of d4PDF is close to that of 20CRv2, MERRA-2 and JRA-55 reanalyses that all have high biases (Zhang *et al.*, 2016). Shortwave radiation is the major input in the diagnostic-type terrestrial biosphere models based on LUE approach, like BEAMS, and therefore, the overestimation of the shortwave radiation may lead to overestimation of GPP. Third, the d4PDF user should be aware that HPB NAT climate simulation excludes interannual atmospheric aerosol variability from both anthropogenic and natural sources, e.g., volcano eruptions, by using constant 1850 values (except for mineral dust and sea salt). Thus, in this study, the difference between the long-term GPP estimates of HPB and HPB NAT represents the difference between long-term GPP that involves only natural climate variability (HPB NAT) and GPP affected by natural climate variability, natural and anthropogenic aerosols and the anthropogenic effect. The d4PDF focuses on the intrinsic natural climate variability, thus, no d4PDF simulations except for HPB, account for the natural external climate forcing (volcano eruptions). For this reason, the drop in the shortwave radiation induced by 1991 volcano eruption that was present in HPB disappears in HPB NAT. The user of d4PDF should be aware of these data peculiarities initiated from the primary aim of d4PDF to study the probability of extreme events.

The present study estimated the climate data-induced uncertainty of the single MRI-AGCM with prescribed observed SST as the lower boundary conditions. In addition, small SST perturbations based on SST analysis error are added to the observed SST (Mizuta *et al.*, 2017). Because the uncertainty in climate variables from AGCM depends on the lateral boundary conditions, the use of the large-size ensembles of climate simulations enables realistic representation of climate with associated internal variability. Evaluation of the surface climate variables of d4PDF by comparison with grid-observations and reanalyses confirmed the model's reasonable performance. While there are numerous studies that attempted to compare variations in climate and carbon fluxes between CMIP5 models (Friedlingstein *et al.*, 2014; Li *et al.*, 2013), the present study attempts to look at the internal variability. This allows statistical estimation of the changes in climate and GPP by comparing different climate scenarios, e.g. HPB and HPB NAT simulations. Here I succeeded to distinguish the anthropogenic and natural effects on the climate and GPP. The benchmarking of the results of this large-ensemble data based study with the study that uses different climate model to generate large-ensemble data when such data set becomes available will provide further insights on the findings.

The empirical method of LAI estimation used in the present study involves only dependency on the surface air temperature. Recent studies report the increasing constraint of moisture on global vegetation (Garonna *et al.*, 2018; Pan *et al.*, 2018). Thus, the water stress on global GPP and the impact of El Niño–related droughts on the tropical GPP might have been underestimated. The results should be interpreted with this caveat in mind.

Here I aimed to estimate the drivers of the GPP anthropogenic effect, specifically CO_2 increase and changes in climate due to anthropogenic emissions from both fossil fuels and land use and land cover changes (LULCC). The LULCC influence global ecosystem directly, i.e. via changes in the land cover, and indirectly via increases in the atmospheric GHGs and aerosols. The indirect influences are accounted for in the d4PDF data set where HPB climate simulation uses the factual concentrations of GHGs and aerosols as opposed to HPB NAT. This enables estimating the impacts of anthropogenic emissions on both climate and carbon fluxes, e.g. GPP. However, the direct influences of LULCC were not accounted for in the biosphere model because the dynamic change in land cover could interfere the results in a way that the climate driving factors were suppressed. In addition, the large uncertainty present in the existing land use data sets would add to the uncertainty in GPP estimates (Meiyappan & Jain, 2012; Sitch *et al.*, 2015; Zhu *et al.*, 2016). By exploiting these findings, the future study would benefit from the attribution of GPP drivers separately to the LULCC and fossil fuel emissions.

On the other hand, exclusion of land use change processes led to the uncertainty in the estimates of the GPP anthropogenic effect. The possible underestimation of the negative GPP anthropogenic effect includes urbanization, deforestation and human-induced fires, especially in the tropics. The possible underestimation of the positive GPP anthropogenic effect include afforestation and agricultural intensification, especially in Europe, former Soviet Union and China (Wang *et al.*, 2017; Zou *et al.*, 2016).

In conclusion, this study is pioneer to provide the estimates of the GPP anthropogenic effect. Such approach allows deeper understanding of how and what part of carbon fluxes was altered by anthropogenic activities with the estimated uncertainty. It contributes to the efforts of both scientific and policy communities to stabilize the climate.

5.2. The contribution of gross primary production into terrestrial carbon cycle

Both terrestrial GPP and TER globally increase with positive temperature and humidity anomalies (Doney *et al.*, 2006). The question to what degree the two processes can compensate each other remains unanswered. Because the d4PDF provides not only historical but future climate data for +2K and +4K, in future studies, I have an opportunity to investigate the future anthropogenic effects on GPP and TER using statistical methods.

Figure 5.3 illustrates the interannual variation of the land carbon uptake, GPP anthropogenic effect and anthropogenic carbon emissions in 1960–2010 (note, that the anthropogenic effect does not include GPP interannual variability). During the study period, the land uptake increased with large interannual variability. The GPP anthropogenic effect coupled with the biosphere sinks until mid-1970s. However, the coupling weakened with time in a way that although the GPP anthropogenic effect increased, the land uptake did not catch up with it. These long-term changes in the land carbon uptake suggest that the role of the global terrestrial GPP decreases. Despite the benefits of the anthropogenic activities on GPP via CO_2 fertilization and climate change, the GPP anthropogenic effect cannot catch up with the increasing anthropogenic and biosphere carbon emissions.

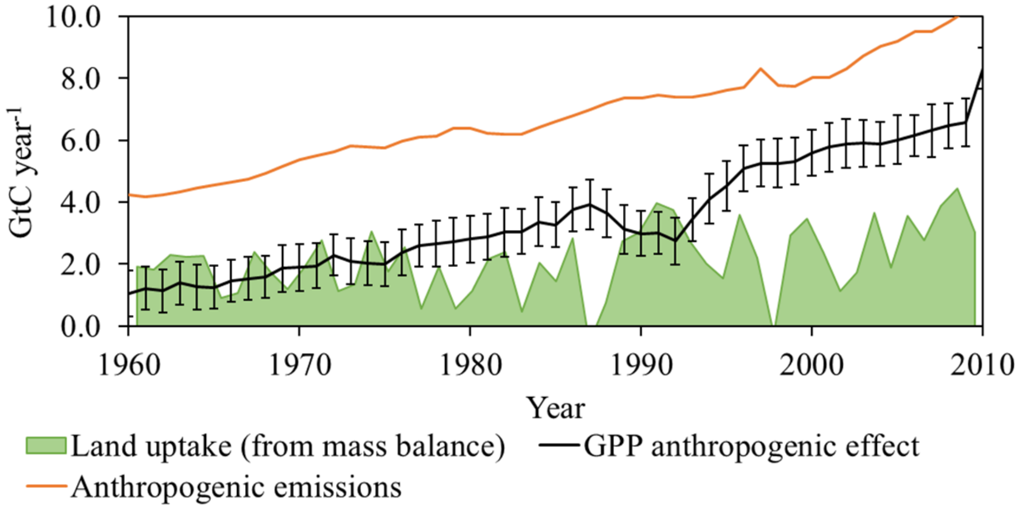

Figure 5.3. Interannual variation of the land carbon uptake, gross primary production (GPP) anthropogenic effect and anthropogenic carbon emissions. Interannual variation is not included into the GPP anthropogenic effect. Error bars indicate the standard deviation of 100-member ensemble runs of BEAMS to estimate GPP.

The findings of this study suggest the major but decreasing role of GPP in the land carbon sink. A number of studies have previously attributed the increase in the land sink to the CO_2 fertilization-driven increase in the GPP in the recent decades (Ballantyne *et al.*, 2017; Friedlingstein *et al.*, 1995; Schimel *et al.*, 2015b). The multi-ensemble biosphere model simulation shows that the increase in the GPP anthropogenic affect in terms of both magnitude and trend exceeds the increase in land sink, suggesting the increase in the biosphere carbon emissions to the atmosphere. Although I accept uncertainty related to the magnitude of estimated GPP due to input data uncertainty and model parametrization, I show that besides the magnitude of GPP anthropogenic effect, its linear trend is also large. Zhang *et al.* (2019b) reported weaker increase rate of GPP compared to greening rate. I caution, however, that the study was short-term (2000–2015) and included warming hiatus period (1998–2012), when GPP anthropogenic effect slowed down (Figure 5.1). The findings are in line with overall conclusions by Zhang *et al.* (2019b) that the capacity of terrestrial GPP may be weakened due to anthropogenic activities.

The absolute magnitude of the GPP anthropogenic effect largely depends on the magnitude of GPP estimate by BEAMS. Thus, the larger absolute magnitude of model GPP estimates will certainly lead to the larger GPP anthropogenic effect. In the case of BEAMS, the absolute value of GPP estimate is largely dependent on the input shortwave radiation. Note, that I do not claim that the estimated magnitude of the GPP anthropogenic effect is certainly exact. However, regardless the magnitude of the GPP anthropogenic effect, its trend does not catch up with the carbon emissions. To support this idea, in addition to the magnitudes, I show the linear trends of the major contributors to the biosphere carbon uptake (Table 5.1). The GPP anthropogenic effect and ocean sink together increased faster than the anthropogenic carbon emissions. Despite that, the rate of the anthropogenic carbon growth continued to increase, suggesting that the anthropogenic effect on the biosphere fluxes, other than terrestrial GPP, play an increasing role in the land sink. The anthropogenic activities resulted in the 347.5 GtC of carbon emissions in five decades. The emissions doubled from 1960s to 2000s. Consistent with Ballantyne *et al.* (2012), I show that the biosphere uptook 55% of anthropogenic carbon emissions. The ocean was steadily uptaking nearly 24% of the anthropogenic carbon emissions. On the contrary, the carbon uptake via the GPP anthropogenic effect largely increased in both magnitude and fraction. While the amount of the carbon uptake from 1960s to 2000s almost doubled, larger part of the emissions remained in the atmosphere. This finding offers evidence of the progressive increase of the biosphere carbon emissions in the recent decades.

Table 5.1. Interannual means and linear trends of the global carbon fluxes in 1960–2010.

	Mean ± IAV (GtC year^{-1})	**Linear trend (GtC year^{-2})**
Emissions from fossil fuel consumption and cement production	5.52 ± 1.70	0.11^{***}
Land-use change emissions	1.30 ± 0.16	0.00^{**}
Total anthropogenic carbon emissions	6.81 ± 1.67	0.11^{***}
Atmospheric carbon growth	3.04 ± 1.27	0.05^{***}
Biosphere uptake (from mass balance)	3.77 ± 1.29	0.06^{***}
Ocean sink	1.64 ± 0.44	0.03^{**}
GPP anthropogenic effect	4.58 ± 2.13	0.14^{**}
Residual atmospheric accumulation	2.45 ± 2.04	0.11^{***}
GPP anthropogenic effect & ocean sink	6.22 ± 2.53	0.17^{***}

Note: *IAV stands for interannual variation via standard deviation. ** corresponds to p- value < 0.01, *** corresponds to p-value < 0.001.*

5.3. The terrestrial ecosystem respiration anthropogenic effect

Most likely, the major biosphere flux responsible for the increased atmospheric carbon growth is TER. The global TER remains the least well-constrained terrestrial flux in the biosphere models and observations are sparse (Bond-Lamberty & Thomson, 2010; Tramontana *et al.*, 2016). As a result, the global TER estimates by the models and observations are inconsistent (Carvalhais *et al.*, 2014). Liu *et al.* (2018b) reported that the short-term carbon uptake variability might be more sensitive to TER losses than previously thought. Here I further develop this idea and suggest that currently the role of TER in the land carbon sink is on the rise.

The studies of the effects of climate change to the global TER remain scarce (Bond-Lamberty *et al.*, 2018; Hashimoto *et al.*, 2015; Hursh *et al.*, 2017; Li *et al.*, 2018; van der Molen *et al.*, 2011). This flux, containing autotrophic and heterotrophic, aboveground and soil parts is yet poorly understood and constrained, especially on a global scale. The current ability of Earth satellites does not allow estimating TER from space, the in situ observations are lacking, especially, in the areas of high soil carbon content, i.e. high latitudes, and, the areas of high litter production, i.e. tropics (Bond-Lamberty & Thomson, 2010; Hursh *et al.*, 2017; Tramontana *et al.*, 2016). The bipolarity of land carbon storage accompanied with disproportionate climate feedback (Schimel *et al.*, 2015a) only add up to the uncertainty. Schimel *et al.* (2015b) highlighted that the TER or combustion may increasingly dominate over GPP in the northern high latitudes, resulting in the release of the massive amount of belowground carbon to the atmosphere in response to climate change. The findings also suggest the bipolarity of the future increase in global TER dominated by mid-latitudes in +2K and tropics in +4K climates. Note, however, that the utilized version of BEAMS did not account for permafrost melting effects. The permafrost melting has the capacity to surpass the amount of carbon released via TER in both mid-latitudes and tropics. Schuur *et al.* (2015) provided evidence of projected gradual and prolonged release of greenhouse gas emissions in the permafrost lands.

TER is likely the major contributor to the increasing land carbon source TER stalled during cooler periods after Pinatubo eruption and 1998–2012 warming hiatus and contributing to the increased land sink (Li *et al.*, 2018). Both magnitude and interannual variability of TER are projected to increase in the future warmer climates. The changes dramatically increase from +2K to +4K climate. Global TER and its interannual variability increase in future with larger relative increase in high latitudes. Currently, anthropogenic TER effect is driven by plant biomass. In future +2K and +4K climates, temperature contribution to the anthropogenic TER effect is projected to increase.

The land carbon sink is a relatively small flux arising from the difference between two fluxes of much larger magnitudes—GPP and TER. I warn that the positive effects of the anthropogenic activities on the land sink, including CO_2 fertilization, greening and increase in the growing season (Forkel *et al.*, 2016; Graven *et al.*, 2013; Zhu *et al.*, 2016) may soon be surpassed by the by the positive effects on the land source.

Previously, Hursh *et al.* (2017) analyzed the relationships between soil respiration (that involves both R_A and SD) with the climate variables and reported the increasing soil respiration with temperature and precipitation, and parabolic relationships with the soil moisture. Authors indicated that soil moisture is the driver of soil respiration in temperate and boreal forests. Carvalhais *et al.* (2014) suggested that the role of water in the terrestrial carbon cycle might increase with time. Contrariwise, the anthropogenic activities-induced CO_2 fertilization lead to increased water use efficiency that can partly compensate for the decreased water availability (Drake *et al.*, 2017). This possibly large effect was neglected in the analysis. The TER response to the changes in water availability is rather complex and poorly understood. Both Ra and SD depend on water availability—decreased precipitation and relative moisture, e.g. droughts, lead to stomatal closure, decreased GPP, and, thus, decreased Ra and TER (van der Molen *et al.*, 2011) on the one hand, and increased tree mortality, consequently, increase litter fall, and, thus, increased SD and TER on the other hand. In addition, SD is on the chemical composition, microbial community composition and acclimation. (van der Molen *et al.*, 2011).

In addition to the direct effect of water availability on TER, Frank *et al.* (2015) and Zscheischler *et al.* (2014a) reported that water scarcity is likely the main driver for negative extreme events. The anthropogenic effect on vapor pressure and precipitation combined with temperature may lead to more frequent and severe weather extremes and disturbances, e.g. droughts, fires and pest outbreaks, that in their turn largely affect GPP. Extreme events contribute to the increase in the land carbon source via not only alterations of TER processes, but also the decrease in photosynthetic capacity. E.g., the increased frequency of the extreme events corresponds to the increase in the GPP extreme events (Frank *et al.*, 2015; Zscheischler *et al.*, 2014b). Modern biosphere models are not skillful enough to correctly estimate the effects of extreme events and disturbances on the terrestrial carbon fluxes, e.g., increased tree mortality (Xiao *et al.*, 2016). The models are shown to underestimate the effects of extreme events. E.g., the MsTMIP models estimate NPP decrease as a response to drought approximately four times shorter and weaker than observations suggest (Ito *et al.*, 2017; Kolus *et al.*, 2019; von Buttlar *et al.*, 2018). The best way to account for the effects of extreme events on the carbon fluxes is to use satellite data that provide reference of the state of terrestrial vegetation (Reichstein *et al.*, 2013). BEAMS is a diagnostic model, however there is no satellite data available as input data for five decades. Therefore, the long-tern estimation likely does not capture total effect of extreme events on GPP. This means that the increase in frequency of the extreme GPP events is larger than estimated, and the GPP anthropogenic effect is lower than shown in Figure 5.1.

Overall, these findings add up to the existing evidences of the shifting roles of global GPP and TER in the land carbon sink. Specifically, I show that currently both magnitude and interannual variation of TER are on the rise and dominated by temperature, followed by highly unceratin effect of water availability, e.g. vapor pressure and precipitation. The autotrophic and heterotrophic fluxes of TER correspond to the changes in climate in different ways. R_A is tight to GPP and limited by it, meaning that the increase in Ra is driven by CO_2 fertilization in proportion to GPP. Meanwhile, SD is tight to temperature and water availability and is not limited by GPP but rather soil carbon content. The weakening role of the GPP and strengthening role of TER and other biosphere carbon sources, e.g. permafrost melting and increased probability of extreme weather events affecting both GPP and TER, highlight the need in the urgent action for stronger mitigation of anthropogenic emissions.

Chapter 6

Conclusion

This thesis aimed to clarify the mechanism of the recent and future changes in the global terrestrial gross primary production (GPP) and ecosystem respiration (TER) by combining the advantages of the diagnostic-type biosphere model and the large-size ensemble climate data. I estimated the anthropogenic effect on the global surface climate and land carbon fluxes, identified their drivers and explored the shifts in the roles of GPP and TER in the land carbon uptake with warming.

First, I decomposed the temporal change in the global GPP into the long-term trend and interannual variability. I associated the long-term GPP with the effect of the anthropogenic emissions and resulting climate change on GPP, i.e. GPP anthropogenic effect, and the interannual GPP variability with the effect of natural climate variability on GPP, i.e. GPP natural effect. Such approach allowed explicit estimating the long-term GPP, and to distinguish the GPP anthropogenic and natural effects with the associated large-size ensemble climate input-data uncertainty. The sensitivity experiment allowed identifying the drivers of the GPP change. The anthropogenic activity altered global climate via increased surface temperatures, intensified water cycle, and reduced shortwave radiation. These changes together with increased atmospheric CO_2 concentration led to the positive GPP anthropogenic effect. It increased from 0.9 ± 0.1 GtC year^{-1} in 1952–1961 to 6.1 ± 0.3 GtC year^{-1} in 2001–2010, and significantly exceeded the climate input-data induced uncertainty. The CO_2 fertilization was the main factor that controlled the GPP anthropogenic effect, and the shortwave radiation that coupled with El Niño Southern Oscillation (ENSO) events and large volcano eruptions was the main factor that controlled the GPP natural effect. Overall, CO_2 fertilization and shortwave radiation explained almost all of GPP change in 1952–2010. The largest positive GPP anthropogenic effect associated with the relaxed water stress and CO_2 fertilization occurred in the semi-arid regions of Southern Hemisphere. The largest negative effect associated with the increased temperature and decreased shortwave radiation occurred in Europe and equatorial tropics. The CO_2 fertilization effect that currently drives the global GPP anthropogenic effect is expected to saturate at >700 ppm CO_2 concentration levels. I project that saturation will happen by year 2050–2150 depending on the Representative Concentration Pathway (RCP) scenario. Meanwhile, in 1952–2010, the CO_2 fertilization effect canceled the negative effect of the decreased shortwave radiation. While currently, the CO_2 fertilization effect primarily drives the tropical GPP increase that dominates the global GPP anthropogenic effect, in the future warmer world, the climate drivers are projected to constrain the tropical GPP increase, so that the climate-driven non-tropical GPP increase takes over the dominancy of the GPP anthropogenic effect.

Second, I analyzed the temporal changes in the anthropogenic and biosphere carbon fluxes with the explicit accountancy of the GPP and TER anthropogenic effects. I showed that despite the benefits of CO_2 fertilization, the positive GPP anthropogenic effect could not catch up with the increasing anthropogenic and biosphere carbon emissions. The role of the TER is likely to dominate over GPP in the land carbon uptake of future warmer world. I showed that both magnitude and interannual variation of TER increase with warming. The main driver of the TER anthropogenic effect is temperature. The probability of years with extremely high global TER increases in the climates +2K and +4K warmer than pre-industrial. The high global TER during extreme years corresponds to high TER in mid-latitudes in +2K and northern high latitudes and equatorial tropics in +4K climate. I attributed these changes to increased autotropic and heterotrophic respirations driven by increased GPP and air temperature. While in 1952–2010, temperature played only a minor role in the TER anthropogenic effect, its role in TER and, thus land carbon uptake is projected to increase in the future warmer climates because the contribution of temperature in driving TER increases with warming exponentially according to Q10 function. Overall, the weakening role of the GPP and strengthening role of TER, marked with a disproportional increase in TER with warming towards high latitudes that are a massive reservoir of soil carbon highlight the need in the urgent action for stronger mitigation of anthropogenic emissions.

Because of the poor current understanding of cloud–radiation feedbacks to climate change and their effects on the carbon cycle, I encourage future studies to focus on cloud–radiation feedbacks. The present study used a single biosphere model and large-ensemble climate simulations using a single climate model. Thus, the results include some uncertainty. In addition, because the utilized d4PDF data set involved some limitations for studying the anthropogenic effect on the climate change, i.e. absence of the natural atmospheric aerosol variability in the nonwarming simulation, the results include the associated level of uncertainty. Finally, estimation of unaccounted land carbon fluxes, e.g. permafrost thawing and subsequent decomposition of organic matter, fires, etc. would further contrite to deepening the understanding of the impact of anthropogenic activities on the terrestrial carbon fluxes.

List of Tables

Table 2.1. BEAMS input data. 8

Table 2.2. Duration, ensemble size, and prescribed boundary conditions of the four simulations of d4PDF. Modified from Mizuta et al. (2017). 11

Table 2.3. Climate and leaf area index (LAI) data sets. 12

Table 2.4. Global 1982–2009 mean and interannual variation (by standard deviation) of climate variables from different data sets (sea surface, desert and ice areas are excluded). 13

Table 2.5. Global 2001–2010 mean and interannual variation (by standard deviation) of leaf area index (LAI) from different data sets. 14

Table 2.6. FLUXNET2015 sites utilized for validation of gross primary production by BEAMS. 20

Table 2.7. Model outputs of Multi-scale Synthesis and Terrestrial Model Intercomparison Project (MsTMIP) models utilized for evaluation of BEAMS performance. 21

Table 2.8. The statistical relationships between soil respiration and climate variables derived by Hursh et al. (2017). 22

Table 3.1. Global mean, interannual variation (IAV) and 1982–2010 linear trend of terrestrial gross primary production (GPP). 29

Table 5.1. Interannual means and linear trends of the global carbon fluxes in 1960–2010. 60

List of Figures

Figure 1.1. Atmospheric CO2 concentrations in parts per million (ppm) for the past 800 000 years, based on EPICA (ice core) data. The peaks and valleys in CO2 levels track the coming and going of ice ages (low CO2) and warmer interglacials (higher levels). Throughout these cycles, atmospheric carbon dioxide was never higher than 300 ppm; in 2018, it reached 407.4 ppm (black dot). NOAA Climate.gov, based on EPICA Dome C data (Lüthi et al., 2008) provided by NOAA NCEI Paleoclimatology Program. Modified reprints from Rebecca Lindsey, https://www.climate.gov/. 2

Figure 2.1. Outline of the BEAMS model structure. 7

Figure 2.2. The study design used to estimate terrestrial gross primary production (GPP) and ecosystem respiration (TER) anthropogenic effect with the input data-induced uncertainty. 16

Figure 2.3. The trajectory of annual BEAMS estimates following spin-up of multi-ensemble (a) gross primary production (GPP) and (b) net ecosystem production (NEP). Gray lines indicate 100 ensemble members and green lines indicate the ensemble-mean with error bars showing standard deviation of 100 ensemble members. Year 1951 is the initial year of spin-up. 17

Figure 3.1. (a) Interannual anomalies and (b) latitudinal variations of climate variables from different data sets (excluding sea surface, desert and ice areas) based on 1982–2009 mean. HPB indicates ensemble-mean of the historical simulation d4PDF data. Error bars indicate standard deviation of the 100 ensemble members. Solid lines correspond to reanalyses, square dot lines correspond to observation-based data sets, and dash dot lines correspond to reanalyses-observation hybrids. (c) Interannual variation (left) of global leaf area index (LAI) and latitudinal variation (right) based on 2000–2010 average LAI from different satellite data sets. HPB indicates ensemble-mean LAI derived from GIMMS3g LAI and d4PDF (HPB) air temperature. 24

Figure 3.2. Comparison between interannual mean gross primary productions (GPP) by BEAMS forced with d4PDF data and in situ GPP observations at 21 eddy-covariance sites globally. The sites are divided into plant functional types by colors: tropical evergreen broadleaf forest (green), crops (orange), deciduous broadleaf forest (blue) and evergreen needle forest (dark blue), wetlands (light blue), grasslands (magenta), savannas (dark red) and shrub-lands (purple). The error bars indicate interannual variation. 27

Figure 3.3. (a) Comparison between interannual mean gross primary production (GPP) by BEAMS forced with GIMMS3g- and d4PDF-based leaf area index (LAI) and fraction of absorbed photosynthetically active radiation (FAPAR) data. The sites are divided into plant functional types by colors: tropical evergreen broadleaf forest (green), crops (orange), deciduous broadleaf forest (blue) and evergreen needle forest (dark blue), wetlands (light blue), grasslands (magenta), savannas (dark red) and shrub-lands (purple). The error bars indicate interannual variation by standard deviation. (b) Comparison of GPP by BEAMS forced with GIMMS3g and d4PDF against GPP flux tower observations at 21 sites globally. 28

Figure 3.4. (a) Interannual variation of 100-member ensemble means of climate variables from historical (HPB) and nonwarming (HPB NAT) climate simulations. The error bars indicate standard deviation between ensemble members. (b) Spatial distribution of the ensemble means of the anthropogenic effect (HPB – HPB NAT) on the climate variables (excluding sea surface, desert and ice areas). 31

Figure 3.5. The gross primary production (GPP) anthropogenic effect. (a) Long-term interannual variation of 100-member ensemble means of the historical and nonwarming climates. The error bars indicate standard deviation between ensemble members. The names of the erupted volcanoes with climatologically corrected Volcanic Explosivity Index (VEI) > 5 are provided. The Multivariate ENSO Index (MEI) data were downloaded from

https://www.esrl.noaa.gov/psd/enso/mei.ext/table.ext.html
and volcano aerosols data were from
http://www.juergen-grieser.de/downloads/VolcanicAerosolForcing/vaod.dat 32

(b) The difference between 1952–2010 GPP of the historical (HPB) and nonwarming (HPB NAT) climate simulations. Latitudinal pattern (1° bands) of mean GPP anthropogenic effect. The shading indicates the longitudinal variation by standard deviation. The sea surface, desert and ice areas are excluded.

Figure 3.6. Interannual variation of gross primary production (GPP) absolute values for seven driving factors of the sensitivity experiment. The default runs of historical (HPB) and nonwarming (HPB NAT) GPP are plotted for comparison. The error bars indicate the spread of 100 ensemble members by standard deviation. 33

Figure 3.7. The interannual gross primary production (GPP) from the CO2 sensitivity experiment using HPB climate simulation data and CO2 concentration data of four Representative Concentration Pathway (RCP) scenarios as a function of (a) year and (b) atmospheric CO2 concentration. 34

Figure 3.8. (a) The 1952–2010 linear trend (95% significance) of gross primary production (GPP) of default HPB run. (b) Spatial distribution of dominant driving factors of GPP trend defined as the driving factor from the sensitivity experiment that contributes the most to the increase (or decrease) in GPP in each vegetated grid cell. The driving factors include CO2, temperature (Temp) and shortwave radiation (Rad). A prefix “+” of the driving factors indicates a positive effect on GPP trends, whereas “-” indicates a negative effect. 35

Figure 3.9. The 1952–2010 linear trends (95% significance) of gross primary production (GPP) for seven driving factors of the sensitivity experiment. The ensemble spreads are defined through standard deviation and relative standard deviation, i.e. standard deviation divided by the ensemble mean. 36

Figure 3.10. The interannual variation of gross primary production (GPP) from the CO2 sensitivity experiment using HPB, 2K, +4K climate simulation data and CO2 concentration data of four Representative Concentration Pathway (RCP) 8.5. The error bars indicate ensemble-spread by standard deviation. 37

Figure 3.11. The difference between (a) +2K default GPP simulation and CO2 sensitivity experiment based on CO2 concentration data of Representative Concentration Pathway (RCP) 8.5 of year 2040 and (b) +4K default GPP simulation and CO2 sensitivity experiment based on RCP8.5 of year 2090. The sea surface, desert and ice areas are excluded. The negative values suggest stronger positive effect of CO2 concentration increase on GPP, and negative values suggest stronger positive effect of climate. 38

Figure 4.1. The interannual variation of the terrestrial ecosystem respiration (TER) anthropogenic effect estimated by BEAMS and TER, TER Q10 effect estimated using d4PDF soil moisture, soil respiration (RS) anomalies by various approaches from the 1980–2010 mean. The anomaly of atmospheric carbon growth is plotted for comparison. 40

Figure 4.2. Spatial distribution of the ensemble means of the anthropogenic effect (difference between +2K or+4K and HPB NAT) on the climate variables (sea surface and desert areas are excluded). 42

Figure 4.3. Probability density functions of global terrestrial ecosystem respiration (TER) in HPB NAT, +2K and +4K climates based on (a) absolute TER values, (b) TER anomalies of the default experiment and (c–f) TER anomalies of future sensitivity experiments for shortwave radiation, vapor pressure, temperature and precipitation (5900 years of HPB NAT, 6 ×540 years of +2K and 6 × 900 years of +4K simulations). 43

Figure 4.4. Latitudinal variation of the average global terrestrial ecosystem respiration (TER) in three climate simulations (a), the +2K and +4K TER anthropogenic effect (b) and relative TER anthropogenic effect relative to the ensemble-mean TER estimated by BEAMS (c). Calculations are based on 5900 years of HPB NAT, 3240 years of +2K and 5400 years of +4K simulations. The shading indicates the longitudinal variation by standard deviation. 45

Figure 4.5. Spatial distribution of the terrestrial ecosystem respiration (TER) corresponding to the difference between the 95th and 5th percentiles of global TER in +2K and +4K in default and sensitivity experiments based on 3240 years of +2K and 5400 years of 4K simulations. 46

Figure 4.6. Spatial distribution of the differences between 95th percentiles and medians of global TER averaged over all years of +2K and +4K climates in (a) default and (b) four sensitivity runs. (c) The spatial distribution of the climate variables that correspond to the differences between 95th percentiles and medians of global TER in four multi-ensemble sensitivity runs. Figures are based on 3240 years for +2K and 5400 years for +4K. 47

Figure 4.7. Probability density functions of global soil respiration (RS) in HPB NAT, +2K and +4K climates based on RS estimated using the statistical relationships with four climate drivers determined by Hursh et al. (2017). 5900 years of HPB NAT, 6 × 540 years of +2K and 6 × 900 years of +4K simulations are used. 49

Figure 4.8. The interannual variation of terrestrial ecosystem respiration (TER) from the BEAMS and Q10 effect on TER based on d4PDF soil temperature data simulated for Representative Concentration Pathway (RCP) 8.5 scenario. The error bars indicate ensemble-spread by standard deviation. 50

Figure 5.1. (a) Interannual variation of 100-member ensemble means of the anthropogenic effect (difference between HPB and HPB NAT simulations) on global surface shortwave radiation and total cloud cover from d4PDF data set. Error bars indicate standard deviation of 100 ensemble members. Sea surface, desert and ice areas are excluded.(b) same for the Northern High Latitudes that correspond to region over 25N, tropics—to region 25S–25N and Southern High Latitudes—to the region over 25S. Sea surface, desert and ice areas are excluded. 53

Figure 5.2. Interannual anomalies of total cloud cover from CRU TS 4.03 and d4PDF (sea surface, desert and ice areas are excluded) based on 1951–2010 mean. HPB indicates ensemble-mean of the historical simulation d4PDF data with error bars indicating standard deviation of 100 ensemble members. (a) Global mean, (b) mean of the tropics corresponding to region 25S–25N, (c) Northern High Latitudes—region over 25N, and (d) Southern High Latitudes—region over 25S. 54

Figure 5.3. Interannual variation of the land carbon uptake, gross primary production (GPP) anthropogenic effect and anthropogenic carbon emissions. Interannual variation is not included into the GPP anthropogenic effect. Error bars indicate the standard deviation of 100-member ensemble runs of BEAMS to estimate GPP. 58

List of Abbreviations

AGCM	Atmospheric General Circulation Model
BEAMS	Biosphere model integrating Eco-physiological And Mechanistic approaches using Satellite data
CMIP5	Coupled Model Intercomparison Project Phase 5
COBE	Centennial Observation-Based Estimates
d4PDF	Database for Policy Decision-Making for Future Climate Change
ENSO	El Niño Southern Oscillation
FAO/UNESCO	Food and Agriculture Organization of the United Nations/United Nations Educational, Scientific, and Cultural Organization
FAPAR	Fraction of Absorbed Photosynthetically Active Radiation
GCB	Global Carbon Project
GCM	General Circulation Models
GHG	greenhouse gas
GPP	Gross Primary Production
IAV	Interannual Variation
LAI	Leaf Area Index
LST	Land Surface Temperature
LUE	Light Use Efficiency
LULUC	Land Use and Land Use Changes
MEI	Multivariate ENSO Index
MRI-AGCM	Meteorological Research Institute Atmospheric General Circulation Model
MsTMIP	Multi-scale Synthesis and Terrestrial Model Intercomparison Project
MTE	Multi-Tree-Ensemble
NEP	Net Ecosystem Production
NH	Northern Hemisphere
NOAA	National Oceanic and Atmospheric Administration
NPP	Net Primary Production
PDF	Probability Density Function
ppm	parts per million
RA	Autotrophic Respiration
RCP	Representative Concentration Pathway
RECCAP	Regional Carbon Cycle Assessment and Processes

SD	Soil Decomposition
SH	Southern Hemisphere
SRDB	Soil Respiration Database
R_S	Soil Respiration
SRTM	Shuttle Radar Topography Mission
SST	Sea Surface Temperature
TER	Terrestrial Ecosystem Respiration
VEI	Volcanic Explosivity Index

Acknowledgements

First, I would like to express my sincere gratitude to my advisor Prof. Sasai for all support, guidance, encouragement, and patience. I am sincerely grateful for all the discussions and advice for this research.

I am deeply thankful to Prof. Yamazaki and Prof. Iwasaki for the brilliant suggestions for the research, continued support and encouragement. I am thankful to all members of the Tohoku University atmospheric science laboratory including those who had left before this thesis was completed. Special thanks to Prof. Muraoka of Gifu University and Prof. T. Rogova of Kazan University who encouraged me to do PhD research.

Since I started to work on this topic, I had precious opportunities to discuss with many scientists. Special thanks to H. Sato from Institute of Arctic Climate and Environment Research, Japan Agency for Marine-Earth Science and Technology, H. Shibata of Hokkaido University, V. Brovkin of Max Planck Institute for Meteorology, O. Boucher of Pierre Simon Laplace Institute and K. Tanaka of National Institute for Environmental Studies for the valuable discussions and technical advice on this research.

I would like to express my thankful appreciation to the Japanese government for granting me the chance to study in Japan together with financial support of the MEXT Scholarship.

This work would not have done without the endless encouragement and support of my family. Deepest thanks for their unconditional love throughout my years of study.

References

Adler, R. F., Huffman, G. J., Chang, A., Ferraro, R., Xie, P.-P., Janowiak, J., et al. (2003). The version-2 global precipitation climatology project (GPCP) monthly precipitation analysis (1979–present). *Journal of Hydrometeorology, 4*(6), 1147-1167.

Ahlström, A., Raupach, M. R., Schurgers, G., Smith, B., Arneth, A., Jung, M., et al. (2015). The dominant role of semi-arid ecosystems in the trend and variability of the land CO2 sink. *Science, 348*(6237), 895-899.

Alton, P. B. (2018). Decadal trends in photosynthetic capacity and leaf area index inferred from satellite remote sensing for global vegetation types. *Agricultural and Forest Meteorology, 250-251*, 361-375.

Anav, A., Friedlingstein, P., Beer, C., Ciais, P., Harper, A., Jones, C., et al. (2015). Spatiotemporal patterns of terrestrial gross primary production: A review. *Reviews of Geophysics, 53*(3), 785-818.

Baldocchi, D., Ryu, Y., & Keenan, T. (2016). Terrestrial Carbon Cycle Variability. *F1000Research, 5*, F1000 Faculty Rev-2371.

Ballantyne, A., Smith, W., Anderegg, W., Kauppi, P., Sarmiento, J., Tans, P., et al. (2017). Accelerating net terrestrial carbon uptake during the warming hiatus due to reduced respiration. *Nature Climate Change, 7*, 148.

Ballantyne, A. P., Alden, C. B., Miller, J. B., Tans, P. P., & White, J. W. C. (2012). Increase in observed net carbon dioxide uptake by land and oceans during the past 50 years. *Nature, 488*, 70.

Beer, C., Reichstein, M., Tomelleri, E., Ciais, P., Jung, M., Carvalhais, N., et al. (2010). Terrestrial Gross Carbon Dioxide Uptake: Global Distribution and Covariation with Climate. *Science*, 1184984.

Bloom, A. A., Exbrayat, J.-F., van der Velde, I. R., Feng, L., & Williams, M. (2016). The decadal state of the terrestrial carbon cycle: Global retrievals of terrestrial carbon allocation, pools, and residence times. *Proceedings of the National Academy of Sciences, 113*(5), 1285-1290.

Boden, T., Andres, R., & Marland, G. (2017). Global, regional, and national fossil-fuel CO2 emissions (1751-2014) (v. 2017). In: Carbon Dioxide Information Analysis Center (CDIAC), Oak Ridge National Laboratory (ORNL), Oak Ridge, TN (United States).

Bonan, G. (2015). *Ecological Climatology: Concepts and Applications* (3 ed.). Cambridge: Cambridge University Press.

Bond-Lamberty, B., Bailey, V. L., Chen, M., Gough, C. M., & Vargas, R. (2018). Globally rising soil heterotrophic respiration over recent decades. *Nature, 560*(7716), 80-83.

Bond-Lamberty, B., & Thomson, A. (2010). A global database of soil respiration data. *Biogeosciences, 7*(6), 1915-1926.

Bond-Lamberty, B. P., & Thomson, A. M. (2018). A Global Database of Soil Respiration Data, Version 4.0. In: ORNL Distributed Active Archive Center.

Boucher, O., Randall, D., Artaxo, P., Bretherton, C., Feingold, G., Forster, P., et al. (2013). Clouds and Aerosols. In T. F. Stocker, D. Qin, G.-K. Plattner, M. Tignor, S. K. Allen, J. Boschung, A. Nauels, Y. Xia, V. Bex, & P. M. Midgley (Eds.), *Climate Change 2013: The Physical Science Basis. Contribution of Working Group I to the Fifth Assessment Report of the Intergovernmental Panel on Climate Change* (pp. 571–658). Cambridge, United Kingdom and New York, NY, USA: Cambridge University Press.

Bousquet, P., Peylin, P., Ciais, P., Le Quéré, C., Friedlingstein, P., & Tans, P. P. (2000). Regional Changes in Carbon Dioxide Fluxes of Land and Oceans Since 1980. *Science, 290*(5495), 1342-1346.

Canadell, J. G., Le Quéré, C., Raupach, M. R., Field, C. B., Buitenhuis, E. T., Ciais, P., et al. (2007a). Contributions to accelerating atmospheric CO2 growth from economic activity, carbon intensity, and efficiency of natural sinks. *Proceedings of the National Academy of Sciences, 104*(47), 18866-18870.

Canadell, J. G., Pataki, D. E., Gifford, R., Houghton, R. A., Luo, Y., Raupach, M. R., et al. (2007b). Saturation of the terrestrial carbon sink. In *Terrestrial ecosystems in a changing world* (pp. 59-78): Springer.

Carvalhais, N., Forkel, M., Khomik, M., Bellarby, J., Jung, M., Migliavacca, M., et al. (2014). Global covariation of carbon turnover times with climate in terrestrial ecosystems. *Nature, 514*, 213.

Ceppi, P., Brient, F., Zelinka, M. D., & Hartmann, D. L. (2017). Cloud feedback mechanisms and their representation in global climate models. *Wiley Interdisciplinary Reviews: Climate Change, 8*(4), e465.

Ciais, P., Sabine, C., Bala, G., Bopp, L., Brovkin, V., Canadell, J., et al. (2013). Carbon and Other Biogeochemical Cycles. In T. F. Stocker, D. Qin, G.-K. Plattner, M. Tignor, S. K. Allen, J. Boschung, A. Nauels, Y. Xia, V. Bex, & P. M. Midgley (Eds.), *Climate Change 2013: The Physical Science Basis. Contribution of Working Group I to the Fifth Assessment Report of the Intergovernmental Panel on Climate Change* (pp. 465–570). Cambridge, United Kingdom and New York, NY, USA: Cambridge University Press.

Compo, G. P., Whitaker, J. S., Sardeshmukh, P. D., Matsui, N., Allan, R. J., Yin, X., et al. (2011). The twentieth century reanalysis project. *Quarterly Journal of the Royal Meteorological Society, 137*(654), 1-28.

De Kauwe, M. G., Lin, Y. S., Wright, I. J., Medlyn, B. E., Crous, K. Y., Ellsworth, D. S., et al. (2016). A test of the ‘one‐point method’for estimating maximum carboxylation capacity from field‐measured, light‐saturated photosynthesis. *New Phytologist, 210*(3), 1130-1144.

Decker, M., Brunke, M. A., Wang, Z., Sakaguchi, K., Zeng, X., & Bosilovich, M. G. (2012). Evaluation of the Reanalysis Products from GSFC, NCEP, and ECMWF Using Flux Tower Observations. *Journal of Climate, 25*(6), 1916-1944.

Dee, D. P., Uppala, S., Simmons, A., Berrisford, P., Poli, P., Kobayashi, S., et al. (2011). The ERA‐Interim reanalysis: Configuration and performance of the data assimilation system. *Quarterly Journal of the royal meteorological society, 137*(656), 553-597.

Dessler, A. E. (2010). A Determination of the Cloud Feedback from Climate Variations over the Past Decade. *Science, 330*(6010), 1523-1527.

Doney, S. C., Lindsay, K., Fung, I., & John, J. (2006). Natural Variability in a Stable, 1000-Yr Global Coupled Climate–Carbon Cycle Simulation. *Journal of Climate, 19*(13), 3033-3054.

Drake, B. L., Hanson, D. T., Lowrey, T. K., & Sharp, Z. D. (2017). The carbon fertilization effect over a century of anthropogenic CO2 emissions: higher intracellular CO2 and more drought resistance among invasive and native grass species contrasts with increased water use efficiency for woody plants in the US Southwest. *Global Change Biology, 23*(2), 782-792.

Fang, Y., Michalak, A., M., Schwalm, C., R., Huntzinger, D., N., Berry, J., A., Ciais, P., et al. (2017). Global land carbon sink response to temperature and precipitation varies with ENSO phase. *Environmental Research Letters, 12*(6), 064007.

Farr, T. G., Rosen, P. A., Caro, E., Crippen, R., Duren, R., Hensley, S., et al. (2007). The Shuttle Radar Topography Mission. *Reviews of Geophysics, 45*(2).

Forkel, M., Carvalhais, N., Rödenbeck, C., Keeling, R., Heimann, M., Thonicke, K., et al. (2016). Enhanced seasonal CO2 exchange caused by amplified plant productivity in northern ecosystems. *Science, 351*(6274), 696-699.

Frank, D., Reichstein, M., Bahn, M., Thonicke, K., Frank, D., Mahecha, M. D., et al. (2015). Effects of climate extremes on the terrestrial carbon cycle: concepts, processes and potential future impacts. *Global Change Biology, 21*(8), 2861-2880.

Friedl, M. A., Sulla-Menashe, D., Tan, B., Schneider, A., Ramankutty, N., Sibley, A., & Huang, X. (2010). MODIS Collection 5 global land cover: Algorithm refinements and characterization of new datasets. *Remote Sensing of Environment, 114*(1), 168-182.

Friedlingstein, P., Fung, I., Holland, E., John, J., Brasseur, G., Erickson, D., & Schimel, D. (1995). On the contribution of CO2 fertilization to the missing biospheric sink. *Global Biogeochemical Cycles, 9*(4), 541-556.

Friedlingstein, P., Meinshausen, M., Arora, V. K., Jones, C. D., Anav, A., Liddicoat, S. K., & Knutti, R. (2014). Uncertainties in CMIP5 climate projections due to carbon cycle feedbacks. *Journal of Climate, 27*(2), 511-526.

Garonna, I., de Jong, R., Stöckli, R., Schmid, B., Schenkel, D., Schimel, D., & Schaepman, M. E. (2018). Shifting relative importance of climatic constraints on land surface phenology. *Environmental Research Letters, 13*(2), 024025.

Gettelman, A., & Sherwood, S. C. (2016). Processes Responsible for Cloud Feedback. *Current Climate Change Reports, 2*(4), 179-189.

Graven, H. D., Keeling, R. F., Piper, S. C., Patra, P. K., Stephens, B. B., Wofsy, S. C., et al. (2013). Enhanced Seasonal Exchange of CO₂ by Northern Ecosystems Since 1960. *Science*.

Gu, L., Baldocchi, D. D., Wofsy, S. C., Munger, J. W., Michalsky, J. J., Urbanski, S. P., & Boden, T. A. (2003). Response of a Deciduous Forest to the Mount Pinatubo Eruption: Enhanced Photosynthesis. *Science, 299*(5615), 2035-2038.

Harris, I., Jones, P., Osborn, T., & Lister, D. (2014). Updated high ‐ resolution grids of monthly climatic observations–the CRU TS3. 10 Dataset. *International Journal of Climatology, 34*(3), 623-642.

Hashimoto, S., Carvalhais, N., Ito, A., Migliavacca, M., Nishina, K., & Reichstein, M. (2015). Global spatiotemporal distribution of soil respiration modeled using a global database. *Biogeosciences, 12*(13), 4121-4132.

Hayasaka, T. (2016). The Long-term Variation in Surface Shortwave Irradiance in China and Japan: A Review. *Journal of the Meteorological Society of Japan. Ser. II, 94*(5), 393-414.

Hirahara, S., Ishii, M., & Fukuda, Y. (2014). Centennial-Scale Sea Surface Temperature Analysis and Its Uncertainty. *Journal of Climate, 27*(1), 57-75.

Houghton, R. A., House, J. I., Pongratz, J., van der Werf, G. R., DeFries, R. S., Hansen, M. C., et al. (2012). Carbon emissions from land use and land-cover change. *Biogeosciences, 9*(12), 5125-5142.

Huntzinger, D. N., Michalak, A. M., Schwalm, C., Ciais, P., King, A. W., Fang, Y., et al. (2017). Uncertainty in the response of terrestrial carbon sink to environmental drivers undermines carbon-climate feedback predictions. *Scientific Reports, 7*(1), 4765.

Huntzinger, D. N., Schwalm, C., Michalak, A. M., Schaefer, K., King, A. W., Wei, Y., et al. (2013). The North American Carbon Program Multi-Scale Synthesis and Terrestrial Model Intercomparison Project – Part 1: Overview and experimental design. *Geoscientific Model Development, 6*(6), 2121-2133.

Huntzinger, D. N., Schwalm, C. R., Wei, Y., Cook, R. B., Michalak, A. M., Schaefer, K., et al. (2018). NACP MsTMIP: Global 0.5-degree Model Outputs in Standard Format, Version 1.0. In: ORNL Distributed Active Archive Center.

Hursh, A., Ballantyne, A., Cooper, L., Maneta, M., Kimball, J., & Watts, J. (2017). The sensitivity of soil respiration to soil temperature, moisture, and carbon supply at the global scale. *Global Change Biology, 23*(5), 2090-2103.

Ichii, K., Hashimoto, H., Nemani, R., & White, M. (2005). Modeling the interannual variability and trends in gross and net primary productivity of tropical forests from 1982 to 1999. *Global and Planetary Change, 48*(4), 274-286.

Iizumi, T., Shiogama, H., Imada, Y., Hanasaki, N., Takikawa, H., & Nishimori, M. (2018). Crop production losses associated with anthropogenic climate change for 1981–2010 compared with preindustrial levels. *International Journal of Climatology, 38*(14), 5405-5417.

IPCC. (2013a). *Climate Change 2013: The Physical Science Basis. Contribution of Working Group I to the Fifth Assessment Report of the Intergovernmental Panel on Climate Change* (T. F. Stocker, D. Qin, G.-K. Plattner, M. Tignor, S. K. Allen, J. Boschung, A. Nauels, Y. Xia, V. Bex, & P. M. Midgley Eds.). Cambridge, United Kingdom and New York, NY, USA: Cambridge University Press.

IPCC. (2013b). Summary for Policymakers. In T. F. Stocker, D. Qin, G.-K. Plattner, M. Tignor, S. K. Allen, J. Boschung, A. Nauels, Y. Xia, V. Bex, & P. M. Midgley (Eds.), *Climate Change 2013: The Physical Science Basis. Contribution of Working Group I to the Fifth Assessment Report of the Intergovernmental Panel on Climate Change* (pp. 1–30). Cambridge, United Kingdom and New York, NY, USA: Cambridge University Press.

Ito, A., Nishina, K., Reyer, C. P., François, L., Henrot, A.-J., Munhoven, G., et al. (2017). Photosynthetic productivity and its efficiencies in ISIMIP2a biome models: benchmarking for impact assessment studies. *Environmental Research Letters, 12*(8), 085001.

Jiang, C., Ryu, Y., Fang, H., Myneni, R., Claverie, M., & Zhu, Z. (2017). Inconsistencies of interannual variability and trends in long-term satellite leaf area index products. *Global Change Biology, 23*(10), 4133-4146.

Joiner, J., Yoshida, Y., Zhang, Y., Duveiller, G., Jung, M., Lyapustin, A., et al. (2018). Estimation of Terrestrial Global Gross Primary Production (GPP) with Satellite Data-Driven Models and Eddy Covariance Flux Data. *Remote Sensing, 10*(9), 1346.

Joos, F., Gerber, S., Prentice, I. C., Otto-Bliesner, B. L., & Valdes, P. J. (2004). Transient simulations of Holocene atmospheric carbon dioxide and terrestrial carbon since the Last Glacial Maximum. *Global Biogeochemical Cycles, 18*(2).

Jung, M., Reichstein, M., Margolis, H. A., Cescatti, A., Richardson, A. D., Arain, M. A., et al. (2011). Global patterns of land-atmosphere fluxes of carbon dioxide, latent heat, and sensible heat derived from eddy covariance, satellite, and meteorological observations. *Journal of Geophysical Research: Biogeosciences, 116*(G3).

Jung, M., Reichstein, M., Schwalm, C. R., Huntingford, C., Sitch, S., Ahlström, A., et al. (2017). Compensatory water effects link yearly global land CO2 sink changes to temperature. *Nature, 541*, 516.

Kalnay, E., Kanamitsu, M., Kistler, R., Collins, W., Deaven, D., Gandin, L., et al. (1996). The NCEP/NCAR 40-year reanalysis project. *Bulletin of the American meteorological Society, 77*(3), 437-471.

Kanniah, K. D., Beringer, J., North, P., & Hutley, L. (2012). Control of atmospheric particles on diffuse radiation and terrestrial plant productivity: A review. *Progress in Physical Geography, 36*(2), 209-237.

Keenan, T. F., Prentice, I. C., Canadell, J. G., Williams, C. A., Wang, H., Raupach, M., & Collatz, G. J. (2016). Recent pause in the growth rate of atmospheric CO2 due to enhanced terrestrial carbon uptake. *Nature Communications, 7*, 13428.

Knyazikhin, Y., Glassy, J., Privette, J., Tian, Y., Lotsch, A., Zhang, Y., et al. (1999). MODIS leaf area index (LAI) and fraction of photosynthetically active radiation absorbed by vegetation (FPAR) product (MOD15) algorithm theoretical basis document. *Theoretical Basis Document, NASA Goddard Space Flight Center, Greenbelt, MD, 20771*.

Kobayashi, S., Ota, Y., Harada, Y., Ebita, A., Moriya, M., Onoda, H., et al. (2015). The JRA-55 reanalysis: General specifications and basic characteristics. *Journal of the Meteorological Society of Japan. Ser. II, 93*(1), 5-48.

Kolus, H. R., Huntzinger, D. N., Schwalm, C. R., Fisher, J. B., McKay, N., Fang, Y., et al. (2019). Land carbon models underestimate the severity and duration of drought's impact on plant productivity. *Scientific Reports, 9*(1), 2758.

Krueger, O., Schenk, F., Feser, F., & Weisse, R. (2013). Inconsistencies between Long-Term Trends in Storminess Derived from the 20CR Reanalysis and Observations. *Journal of Climate, 26*(3), 868-874.

Kunkel, K. E., Easterling, D. R., Hubbard, K., & Redmond, K. (2004). Temporal variations in frost-free season in the United States: 1895–2000. *Geophysical Research Letters, 31*(3).

Lasslop, G., Reichstein, M., Papale, D., Richardson, A. D., Arneth, A., Barr, A., et al. (2010). Separation of net ecosystem exchange into assimilation and respiration using a light response curve approach: critical issues and global evaluation. *Global Change Biology, 16*(1), 187-208.

Lawrimore, J. H., Menne, M. J., Gleason, B. E., Williams, C. N., Wuertz, D. B., Vose, R. S., & Rennie, J. (2011). An overview of the Global Historical Climatology Network monthly mean temperature data set, version 3. *Journal of Geophysical Research: Atmospheres, 116*(D19).

Le Quéré, C., Andrew, R. M., Canadell, J. G., Sitch, S., Korsbakken, J. I., Peters, G. P., et al. (2016). Global Carbon Budget 2016. *Earth Syst. Sci. Data, 8*(2), 605-649.

Le Quéré, C., Andrew, R. M., Friedlingstein, P., Sitch, S., Hauck, J., Pongratz, J., et al. (2018). Global Carbon Budget 2018. *Earth Syst. Sci. Data, 10*(4), 2141-2194.

Li, J.-L. F., Waliser, D. E., Stephens, G., Lee, S., L'Ecuyer, T., Kato, S., et al. (2013). Characterizing and understanding radiation budget biases in CMIP3/CMIP5 GCMs, contemporary GCM, and reanalysis. *Journal of Geophysical Research: Atmospheres, 118*(15), 8166-8184.

Li, W., Ciais, P., Wang, Y., Yin, Y., Peng, S., Zhu, Z., et al. (2018). Recent Changes in Global Photosynthesis and Terrestrial Ecosystem Respiration Constrained From Multiple Observations. *Geophysical Research Letters, 45*(2), 1058-1068.

Liu, F., Chai, J., Huang, G., Liu, J., & Chen, Z. (2015). Modulation of decadal ENSO-like variation by effective solar radiation. *Dynamics of Atmospheres and Oceans, 72*, 52-61.

Liu, Y., Liu, R., & Chen, J. M. (2012). Retrospective retrieval of long‐term consistent global leaf area index (1981–2011) from combined AVHRR and MODIS data. *Journal of Geophysical Research: Biogeosciences, 117*(G4).

Liu, Y., Xiao, J., Ju, W., Zhu, G., Wu, X., Fan, W., et al. (2018a). Satellite-derived LAI products exhibit large discrepancies and can lead to substantial uncertainty in simulated carbon and water fluxes. *Remote Sensing of Environment, 206*, 174-188.

Liu, Z., Ballantyne, A. P., Poulter, B., Anderegg, W. R. L., Li, W., Bastos, A., & Ciais, P. (2018b). Precipitation thresholds regulate net carbon exchange at the continental scale. *Nature Communications, 9*(1), 3596.

Lucht, W., Prentice, I. C., Myneni, R. B., Sitch, S., Friedlingstein, P., Cramer, W., et al. (2002). Climatic Control of the High-Latitude Vegetation Greening Trend and Pinatubo Effect. *Science, 296*(5573), 1687-1689.

Lüthi, D., Le Floch, M., Bereiter, B., Blunier, T., Barnola, J.-M., Siegenthaler, U., et al. (2008). High-resolution carbon dioxide concentration record 650,000–800,000 years before present. *Nature, 453*(7193), 379-382.

Ma, J., Yan, X., Dong, W., & Chou, J. (2015). Gross primary production of global forest ecosystems has been overestimated. *Scientific Reports, 5*, 10820.

Mao, J., Fu, W., Shi, X., Ricciuto, D. M., Fisher, J. B., Dickinson, R. E., et al. (2015). Disentangling climatic and anthropogenic controls on global terrestrial evapotranspiration trends. *Environmental Research Letters, 10*(9), 094008.

Meinshausen, M., Smith, S. J., Calvin, K., Daniel, J. S., Kainuma, M. L. T., Lamarque, J.-F., et al. (2011). The RCP greenhouse gas concentrations and their extensions from 1765 to 2300. *Climatic Change, 109*(1), 213.

Meiyappan, P., & Jain, A. K. (2012). Three distinct global estimates of historical land-cover change and land-use conversions for over 200 years. *Frontiers of Earth Science, 6*(2), 122-139.

Melnikova, I., Awaya, Y., Saitoh, T., Muraoka, H., & Sasai, T. (2018). Estimation of Leaf Area Index in a Mountain Forest of Central Japan with a 30-m Spatial Resolution Based on Landsat Operational Land Imager Imagery: An Application of a Simple Model for Seasonal Monitoring. *Remote Sensing, 10*(2), 179.

Mercado, L. M., Bellouin, N., Sitch, S., Boucher, O., Huntingford, C., Wild, M., & Cox, P. M. (2009). Impact of changes in diffuse radiation on the global land carbon sink. *Nature, 458,* 1014.

Mizuta, R., Murata, A., Ishii, M., Shiogama, H., Hibino, K., Mori, N., et al. (2017). Over 5,000 Years of Ensemble Future Climate Simulations by 60-km Global and 20-km Regional Atmospheric Models. *Bulletin of the American Meteorological Society, 98*(7), 1383-1398.

Mizuta, R., Yoshimura, H., Murakami, H., Matsueda, M., Endo, H., Ose, T., et al. (2012). Climate Simulations Using MRI-AGCM3.2 with 20-km Grid. *Journal of the Meteorological Society of Japan. Ser. II, 90A,* 233-258.

Murray-Tortarolo, G., Anav, A., Friedlingstein, P., Sitch, S., Piao, S., Zhu, Z., et al. (2013). Evaluation of Land Surface Models in Reproducing Satellite-Derived LAI over the High-Latitude Northern Hemisphere. Part I: Uncoupled DGVMs. *Remote Sensing, 5*(10), 4819.

Myneni, R. B., Keeling, C. D., Tucker, C. J., Asrar, G., & Nemani, R. R. (1997). Increased plant growth in the northern high latitudes from 1981 to 1991. *Nature, 386*(6626), 698-702.

Nemani, R. R., Keeling, C. D., Hashimoto, H., Jolly, W. M., Piper, S. C., Tucker, C. J., et al. (2003). Climate-driven increases in global terrestrial net primary production from 1982 to 1999. *Science, 300*(5625), 1560-1563.

Norris, J. R., Allen, R. J., Evan, A. T., Zelinka, M. D., O'Dell, C. W., & Klein, S. A. (2016). Evidence for climate change in the satellite cloud record. *Nature, 536,* 72.

Norton, A. J., Rayner, P. J., Koffi, E. N., Scholze, M., Silver, J. D., & Wang, Y.-P. (2018). Estimating global gross primary productivity using chlorophyll fluorescence and a data assimilation system with the BETHY-SCOPE model. *Biogeosciences Discussions, 2018,* 1-40.

Oleson, K. W., Lawrence, D. M., Gordon, B., Flanner, M. G., Kluzek, E., Peter, J., et al. (2010). Technical description of version 4.0 of the Community Land Model (CLM).

Pan, N., Feng, X., Fu, B., Wang, S., Ji, F., & Pan, S. (2018). Increasing global vegetation browning hidden in overall vegetation greening: Insights from time-varying trends. *Remote Sensing of Environment, 214,* 59-72.

Parton, W., Scurlock, J., Ojima, D., Gilmanov, T., Scholes, R., Schimel, D., et al. (1993). Observations and modeling of biomass and soil organic matter dynamics for the grassland biome worldwide. *Global Biogeochemical Cycles, 7*(4), 785-809.

Piao, S., Sitch, S., Ciais, P., Friedlingstein, P., Peylin, P., Wang, X., et al. (2013). Evaluation of terrestrial carbon cycle models for their response to climate variability and to CO2 trends. *Global Change Biology, 19*(7), 2117-2132.

Reichstein, M., Bahn, M., Ciais, P., Frank, D., Mahecha, M. D., Seneviratne, S. I., et al. (2013). Climate extremes and the carbon cycle. *Nature, 500,* 287.

Reichstein, M., Falge, E., Baldocchi, D., Papale, D., Aubinet, M., Berbigier, P., et al. (2005). On the separation of net ecosystem exchange into assimilation and ecosystem respiration: review and improved algorithm. *Global Change Biology, 11*(9), 1424-1439.

Richardson, T. B., Forster, P. M., Andrews, T., Boucher, O., Faluvegi, G., Fläschner, D., et al. (2018). Drivers of Precipitation Change: An Energetic Understanding. *Journal of Climate, 31*(23), 9641-9657.

Saha, S., Moorthi, S., Pan, H.-L., Wu, X., Wang, J., Nadiga, S., et al. (2010). NCEP Climate Forecast System Reanalysis (CFSR) Selected Hourly Time-Series Products, January 1979 to December 2010. In. Boulder, Colo: Research Data Archive at the National Center for Atmospheric Research, Computational and Information Systems Laboratory.

Sasai, T., Ichii, K., Yamaguchi, Y., & Nemani, R. (2005). Simulating terrestrial carbon fluxes using the new biosphere model "biosphere model integrating eco‐physiological and mechanistic approaches using satellite data" (BEAMS). *Journal of Geophysical Research: Biogeosciences, 110*(G2).

Sasai, T., Obikawa, H., Murakami, K., Kato, S., Matsunaga, T., & Nemani, R. R. (2016). Estimation of net ecosystem production in Asia using the diagnostic‐type ecosystem model with a 10‐km grid‐scale resolution. *Journal of Geophysical Research: Biogeosciences*.

Sasai, T., Okamoto, K., Hiyama, T., & Yamaguchi, Y. (2007). Comparing terrestrial carbon fluxes from the scale of a flux tower to the global scale. *Ecological Modelling, 208*(2), 135-144.

Sato, H., Kumagai, T., Takahashi, A., & Katul, G. G. (2015). Effects of different representations of stomatal conductance response to humidity across the African continent under warmer CO2-enriched climate conditions. *Journal of Geophysical Research: Biogeosciences, 120*(5), 979-988.

Schimel, D., Pavlick, R., Fisher, J. B., Asner, G. P., Saatchi, S., Townsend, P., et al. (2015a). Observing terrestrial ecosystems and the carbon cycle from space. *Global Change Biology, 21*(5), 1762-1776.

Schimel, D., Stephens, B. B., & Fisher, J. B. (2015b). Effect of increasing CO2 on the terrestrial carbon cycle. *Proceedings of the National Academy of Sciences, 112*(2), 436-441.

Schneider, U., Becker, A., Finger, P., Meyer-Christoffer, A., Rudolf, B., & Ziese, M. (2011). GPCC Full Data Reanalysis Version 6.0 at 1.0°: Monthly Land-Surface Precipitation from Rain-Gauges built on GTS-based and Historic Data. In.

Schuur, E. A. G., McGuire, A. D., Schädel, C., Grosse, G., Harden, J. W., Hayes, D. J., et al. (2015). Climate change and the permafrost carbon feedback. *Nature, 520,* 171.

Schwalm, C. R., Huntzinger, D. N., Fisher, J. B., Michalak, A. M., Bowman, K., Ciais, P., et al. (2015). Toward “optimal” integration of terrestrial biosphere models. *Geophysical Research Letters, 42*(11), 4418-4428.

Setoyama, Y., & Sasai, T. (2013). Analyzing decadal net ecosystem production control factors and the effects of recent climate events in Japan. *Journal of Geophysical Research: Biogeosciences, 118*(1), 337-351.

Sheffield, J., Goteti, G., & Wood, E. F. (2006). Development of a 50-year high-resolution global dataset of meteorological forcings for land surface modeling. *Journal of Climate, 19*(13), 3088-3111.

Sitch, S., Friedlingstein, P., Gruber, N., Jones, S., Murray-Tortarolo, G., Ahlström, A., et al. (2015). Recent trends and drivers of regional sources and sinks of carbon dioxide. *Biogeosciences, 12*(3), 653-679.

Sitch, S., Huntingford, C., Gedney, N., Levy, P. E., Lomas, M., Piao, S. L., et al. (2008). Evaluation of the terrestrial carbon cycle, future plant geography and climate-carbon cycle feedbacks using five Dynamic Global Vegetation Models (DGVMs). *Global Change Biology, 14*(9), 2015-2039.

Sitch, S., Smith, B., Prentice, I. C., Arneth, A., Bondeau, A., Cramer, W., et al. (2003). Evaluation of ecosystem dynamics, plant geography and terrestrial carbon cycling in the LPJ dynamic global vegetation model. *Global Change Biology, 9*(2), 161-185.

Slingo, A. (1989). A GCM Parameterization for the Shortwave Radiative Properties of Water Clouds. *Journal of the Atmospheric Sciences, 46*(10), 1419-1427.

Smith, B., Prentice, I. C., & Sykes, M. T. (2001). Representation of vegetation dynamics in the modelling of terrestrial ecosystems: comparing two contrasting approaches within European climate space. *Global Ecology and Biogeography, 10*(6), 621-637.

Smith, W. K., Reed, S. C., Cleveland, C. C., Ballantyne, A. P., Anderegg, W. R. L., Wieder, W. R., et al. (2015). Large divergence of satellite and Earth system model estimates of global terrestrial CO2 fertilization. *Nature Climate Change, 6*, 306.

Stöckli, R., Rutishauser, T., Baker, I., Liniger, M. A., & Denning, A. S. (2011). A global reanalysis of vegetation phenology. *Journal of Geophysical Research: Biogeosciences, 116*(G3).

Tramontana, G., Jung, M., Schwalm, C. R., Ichii, K., Camps-Valls, G., Ráduly, B., et al. (2016). Predicting carbon dioxide and energy fluxes across global FLUXNET sites with regression algorithms. *Biogeosciences, 13*(14), 4291-4313.

Trenberth, K. E., & Fasullo, J. T. (2009). Global warming due to increasing absorbed solar radiation. *Geophysical Research Letters, 36*(7).

van der Molen, M. K., Dolman, A. J., Ciais, P., Eglin, T., Gobron, N., Law, B. E., et al. (2011). Drought and ecosystem carbon cycling. *Agricultural and Forest Meteorology, 151*(7), 765-773.

Verger, A., Filella, I., Baret, F., & Peñuelas, J. (2016). Vegetation baseline phenology from kilometric global LAI satellite products. *Remote Sensing of Environment, 178*, 1-14.

von Buttlar, J., Zscheischler, J., Rammig, A., Sippel, S., Reichstein, M., Knohl, A., et al. (2018). Impacts of droughts and extreme-temperature events on gross primary production and ecosystem respiration: a systematic assessment across ecosystems and climate zones. *Biogeosciences, 15*(1), 1293-1318.

Wang, A., & Zeng, X. (2013). Development of Global Hourly 0.5° Land Surface Air Temperature Datasets. *Journal of Climate, 26*(19), 7676-7691.

Wang, J., Dong, J., Yi, Y., Lu, G., Oyler, J., Smith, W., et al. (2017). Decreasing net primary production due to drought and slight decreases in solar radiation in China from 2000 to 2012. *Journal of Geophysical Research: Biogeosciences, 122*(1), 261-278.

Wang, W., Ciais, P., Nemani, R. R., Canadell, J. G., Piao, S., Sitch, S., et al. (2013). Variations in atmospheric CO2 growth rates coupled with tropical temperature. *Proceedings of the National Academy of Sciences, 110*(32), 13061-13066.

Webb, R. S., Rosenzweig, C. E., & Levine, E. R. (1993). Specifying land surface characteristics in general circulation models: Soil profile data set and derived water-holding capacities. *Global Biogeochemical Cycles, 7*(1), 97-108.

Wei, Y., Liu, S., Huntzinger, D. N., Michalak, A. M., Viovy, N., Post, W. M., et al. (2014). The North American carbon program multi-scale synthesis and terrestrial model intercomparison project–Part 2: environmental driver data. *Geoscientific Model Development Discussions, 7*, 2875-2893.

Welp, L. R., Keeling, R. F., Meijer, H. A. J., Bollenbacher, A. F., Piper, S. C., Yoshimura, K., et al. (2011). Interannual variability in the oxygen isotopes of atmospheric CO2 driven by El Niño. *Nature, 477*, 579.

Wild, M. (2012). Enlightening Global Dimming and Brightening. *Bulletin of the American Meteorological Society, 93*(1), 27-37.

Wild, M. (2016). Decadal changes in radiative fluxes at land and ocean surfaces and their relevance for global warming. *Wiley Interdisciplinary Reviews: Climate Change, 7*(1), 91-107.

Xiao, J., Liu, S., & Stoy, P. C. (2016). Preface: Impacts of extreme climate events and disturbances on carbon dynamics. *Biogeosciences*(13), 3665-3675.

Xiao, Z., Liang, S., Wang, J., Chen, P., Yin, X., Zhang, L., & Song, J. (2014). Use of general regression neural networks for generating the GLASS leaf area index product from time-series MODIS surface reflectance. *IEEE Transactions on Geoscience and Remote Sensing, 52*(1), 209-223.

Yeh, S.-W., Kug, J.-S., Dewitte, B., Kwon, M.-H., Kirtman, B. P., & Jin, F.-F. (2009). El Niño in a changing climate. *Nature, 461*, 511.

Yuan, H., Dai, Y., Xiao, Z., Ji, D., & Shangguan, W. (2011). Reprocessing the MODIS Leaf Area Index products for land surface and climate modelling. *Remote Sensing of Environment, 115*(5), 1171-1187.

Yukimoto, S., Adachi, Y., Hosaka, M., Sakami, T., Yoshimura, H., Hirabara, M., et al. (2012). A new global climate model of the Meteorological Research Institute: MRI-CGCM3—model description and basic performance—. *Journal of the Meteorological Society of Japan. Ser. II, 90*, 23-64.

Zeng, N., Mariotti, A., & Wetzel, P. (2005). Terrestrial mechanisms of interannual CO2 variability. *Global Biogeochemical Cycles, 19*(1).

Zhang, X., Liang, S., Wang, G., Yao, Y., Jiang, B., & Cheng, J. (2016). Evaluation of the reanalysis surface incident shortwave radiation products from NCEP, ECMWF, GSFC, and JMA using satellite and surface observations. *Remote Sensing, 8*(3), 225.

Zhang, Y., Dannenberg, M. P., Hwang, T., & Song, C. (2019a). El Niño–Southern Oscillation-induced variability of terrestrial gross primary production during the satellite era. *Journal of Geophysical Research: Biogeosciences, 124*.

Zhang, Y., Song, C., Band, L. E., & Sun, G. (2019b). No Proportional Increase of Terrestrial Gross Carbon Sequestration From the Greening Earth. *Journal of Geophysical Research: Biogeosciences, 124*(8), 2540-2553.

Zhao, M., & Running, S. W. (2010). Drought-Induced Reduction in Global Terrestrial Net Primary Production from 2000 Through 2009. *Science, 329*(5994), 940-943.

Zhu, Z., Bi, J., Pan, Y., Ganguly, S., Anav, A., Xu, L., et al. (2013). Global data sets of vegetation leaf area index (LAI) 3g and Fraction of Photosynthetically Active Radiation (FPAR) 3g derived from Global Inventory Modeling and Mapping Studies (GIMMS) Normalized Difference Vegetation Index (NDVI3g) for the period 1981 to 2011. *Remote Sensing, 5*(2), 927-948.

Zhu, Z., Piao, S., Myneni, R. B., Huang, M., Zeng, Z., Canadell, J. G., et al. (2016). Greening of the Earth and its drivers. *Nature Climate Change*.

Zou, L., Wang, L., Lin, A., Zhu, H., Peng, Y., & Zhao, Z. (2016). Estimation of global solar radiation using an artificial neural network based on an interpolation technique in southeast China. *Journal of Atmospheric and Solar-Terrestrial Physics, 146*, 110-122.

Zscheischler, J., Mahecha, M. D., Von Buttlar, J., Harmeling, S., Jung, M., Rammig, A., et al. (2014a). A few extreme events dominate global interannual variability in gross primary production. *Environmental Research Letters, 9*(3), 035001.

Zscheischler, J., Michalak, A. M., Schwalm, C., Mahecha, M. D., Huntzinger, D. N., Reichstein, M., et al. (2014b). Impact of large-scale climate extremes on biospheric carbon fluxes: An intercomparison based on MsTMIP data. *Global Biogeochemical Cycles, 28*(6), 585-600.